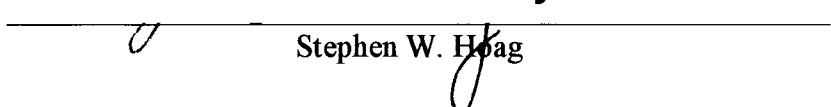


AN ABSTRACT OF THE THESIS OF

Syed A. Altaf for the degree of Doctor of Philosophy in Pharmacy presented on December 13, 1995. Title: Tablet Machine Instrumentation to Study Tablet Compaction and Compression of Polymer Coated Beads into Tablets

Abstract approved: *Redacted for Privacy*

 Stephen W. Hoag

This thesis dissertation is comprised of three distinct sections, which are described below:

Deformations that affect the vertical punch displacement of a Stokes B2 rotary tablet press were characterized with a cathetometer. The press deformation was found to be elastic for both the upper and lower compression roller assemblies. However, the upper and lower compression roller assemblies have different Hookian spring constants:  $8.58 \times 10^4$  and  $5.18 \times 10^4$  kN/m for the upper and lower assemblies, respectively. Using two-way ANOVA, the Hookian spring constants were shown to be independent of compaction phases and lower punch penetration setting. To study the influence of press deformation on tablet compaction, the Hookian spring constants were factored into the calculation of the incremental work of compaction for dibasic calcium phosphate dihydrate and microcrystalline cellulose.

A split-web die concept was proposed which encloses the sensing web in a cylinder for die wall stress measurements. This design avoids binding of the sensing web and isolates stress measurement to the narrow band around the tablet. A design-by-analysis approach and finite element analysis (FEA) software were used to determine optimal strain gage placement and web dimensions for the split-web die design. The commercial finite element program COSMOS/M was employed. Based on FEA results, a 1/8 in. sensing web with a strain gage located at  $\phi = 0^\circ$  was selected for experimental testing. A linear calibration curve ( $r^2=0.999$ ) with no hysteresis was

obtained, verifying the FEA predictions. Residual die wall stress (RDWS) and radial versus axial stress transmission curves were generated for commonly used excipients.

To better understand factors that affect coat integrity upon compression of polymer coated beads into tablets, multi-layered beads were manufactured and evaluated. The multi-layered beads consist of several alternating layers of acetaminophen and polymer coats (Aquacoat<sup>®</sup>) with an outer layer of mannitol as a cushioning excipient. The Avicel PH-101 coats were applied at 20, 40, 60 and 80% w/w of total bead weight as layer 7, 8, 9 and 10, respectively. The results showed a loss of sustained release properties upon compaction of the multilayered beads. The application of cushioning excipients by spray coating onto polymer coated beads was successfully done. The effect of compression on bead size showed that smaller size beads could be compacted at low pressure to make physically stable caplets. Four new concepts were then developed and evaluated i.e. Excipient / disintegrant coated compacts, Sealant-effect compacts, Triple-layered caplets, and Granulated bead compacts. The effect of polymer coat thickness, cushioning excipients, and compaction pressure on drug release from compressed bead formulations was also investigated.

**Tablet Machine Instrumentation to Study Tablet Compaction  
And  
Compression of Polymer-Coated Beads into Tablets**

by

**Syed A. Altaf**

**A THESIS**

submitted to

**Oregon State University**

in partial fulfillment of  
the requirements for the  
degree of

**Doctor of Philosophy**

**Presented December 13, 1995  
Commencement June 1996**

Doctor of Philosophy thesis of Syed A. Altaf presented on December 13, 1995

APPROVED:

*Redacted for Privacy*

Major Professor/Representing Pharmacy

*Redacted for Privacy*

Dean of College of Pharmacy

*Redacted for Privacy*

Dean of Graduate School

I understand that my thesis will become part of the permanent collection of Oregon State University libraries. My signature below authorizes release of my thesis to any reader upon request.

*Redacted for Privacy*

Syed A. Altaf, Author

## ACKNOWLEDGMENTS

I would like to thank the almighty ALLAH for His guidance, His mercy and His blessings in every step of my life.

I dedicate this thesis to my parents and my sisters for their constant support, love, patience and encouragement throughout my studies.

I would like to express my sincere gratitude to my major professor, Dr. Stephen W. Hoag for his invaluable help, guidance, constant encouragement, and advice throughout the course of my Ph.D. thesis.

I would also like to thank Dr. James W. Ayres for his constant support, encouragement, and his positive attitude towards every experimental result.

I thank my committee members Dr. Mark Christensen, Dr. David Thomas and Dr. Thomas Savage for their valuable time.

Special thanks to Dr. Joyce Chou, who has helped me in many stages of this thesis. Joyce is a true friend who's encouragement, help and friendship is unforgettable.

Thanks to all my fellow graduate students and everyone in pharmaceuticals lab for making all these years lots of fun in the lab.

Thanks extended to the staff at College of Pharmacy office and stock room and also the staff at Graduate School for being always helpful and nice to me.

## CONTRIBUTION OF AUTHORS

Dr. Chuntien Yeh assisted in computer aided engineering stress analysis of the Split-web die design. Dr. James Ayres co-advised the bead compaction study.

## TABLE OF CONTENTS

CHAPTER I	INTRODUCTION.....	1
CHAPTER II	DEFORMATION OF THE STOKES B2 ROTARY TABLET PRESS: QUANTITATION AND INFLUENCE ON TABLET COMPACTION.....	4
	Abstract.....	5
	Introduction.....	6
	Experimental.....	8
	Results and discussion.....	12
	Conclusions.....	37
	References.....	39
CHAPTER III	FORCE TRANSDUCER DESIGN FOR DIE WALL STRESS MEASUREMENT DURING TABLET COMPACTION: OPTIMIZATION AND VALIDATION OF SPLIT-WEB DIE USING FINITE ELEMENT ANALYSIS.....	41
	Abstract.....	42
	Introduction.....	43
	Theory.....	46
	Experimental.....	48
	Results and discussion.....	51
	Conclusions.....	68
	References.....	70

TABLE OF CONTENTS (continued)

CHAPTER IV BEAD COMPACTS: I. COMPRESSION OF POLYMER COATED MULTI-LAYERED BEAD FORMULATIONS.....	72
Abstract.....	73
Introduction.....	74
Experimental.....	76
Results and discussion.....	84
Conclusions.....	95
References.....	97
CHAPTER V BEAD COMPACTS: II. EVALUATION OF RAPIDLY DISINTEGRATING FORMULATIONS FROM COMPRESSED POLYMER-COATED BEADS.....	99
Abstract.....	100
Introduction.....	101
Experimental.....	103
Results and discussion.....	108
Conclusions.....	125
References.....	126
CHAPTER VI CONCLUSION.....	128
BIBLIOGRAPHY.....	132
APPENDICES.....	138



TABLE OF CONTENTS (continued)

APPENDIX A	SUMMARIZED TABLES FOR DATA ON DEFORMATION OF STOKES B2 ROTARY TABLET PRESS AT DIFFERENT COMPACTION PHASES AND PUNCH PENETRATION SETTINGS.....	139
APPENDIX B	FORCE TRANSDUCER DESIGN FOR DIE WALL STRESS MEASUREMENT DURING TABLET COMPACTION: I. GENERAL THEORY OF DESIGN OPTIMIZATION USING TRADITIONAL STRESS ANALYSIS AND FINITE ELEMENT ANALYSIS.....	149
	Abstract.....	150
	Introduction.....	151
	Optimal design methodology.....	154
	Design examples.....	162
	Conclusions.....	191
	References.....	193

Figure	LIST OF FIGURES	Page
II.1	Schematic of punch head, the arrows denote the position of the compression roller when readings were taken for the loading, dwell, and unloading phases.	11
II.2	Punch separation for the upper and lower punches versus punch stress (error bars within symbols).	13
II.3	Height of lead compact versus applied punch stress.	19
II.4	Punch displacement corrected for press deformation versus time for the lower punch; the maximum punch stresses were 0 MPa, 65 MPa, 135 MPa, and 225 Mpa.	22
II.5	Force-displacement profile showing the nonelastic and elastic curves for (a) Emcompress and (b) Avicel PH-101.	23
II.6	For Emcompress, lower punch incremental work versus time for the three phases of tablet compaction, i.e. loading, dwell, and unloading, and for three different maximum pressures.	29
II.7	Lower punch incremental work versus time for Avicel and Emcompress compressed to a peak punch pressure of 135 Mpa.	35
II.8	A schematic representation of the coupling between press elasticity and tablet viscoelasticity.	36
III.1	Assembly of the three layer split web die design.	45
III.2	Finite Element Model for the 1/8 in. sensing web.	47
III.3	Dimensions of sensing web for the split web die.	50
III.4	Von Mises stress contour for the 1/16 in. prototype sensing web at maximum inner die wall pressure of 120 Mpa.	54

Figure	LIST OF FIGURES(continued)	Page
III.5	A deformed 1/8 in. sensing web showing maximum nodes displacement at the arch of the sensing web.	56
III.6	Effect of web thickness on tangential strain for the 1/8 and 1/16 in. sensing webs.	57
III.7	Effect of strain gage position $\phi = 0^\circ, 30^\circ$ and $60^\circ$ on tangential strain at inner die wall pressures ranging from 0 to 120 Mpa.	60
III.8	Experimental calibration curve for the split web die using Neoprene rubber plugs.	61
III.9	Radial versus axial stress transmission curves for sodium chloride using 1/8 in. sensing web.	64
III.10	Radial versus axial stress transmission curves for Starch 1500 using 1/8 in. sensing web.	65
III.11	Residual die wall stress versus maximum axial stress using 1/8 in. sensing web for the excipients studied.	67
IV.1	Cross sectional view of a 10 layer multi-layered bead.	80
IV.2	Scanning electron micrographs (SEM) of a L 10 Multi-Layered Bead; magnification, A = 60 & B =340.	85
IV.3	Percent drug release versus time profiles for the non-compacted Multi-Layered Beads.	86
IV.4	SEM's of the deformed Multi-Layered Bead upon compaction at 500 lb.; magnification, A = 50 & B = 480.	87
IV.5	Dissolution profiles of the compacted (500 lb) versus non-compacted Multi-Layered Beads.	88
IV.6	Multi-Layered Beads compressed at 500 lb.: Effect of drug release from intact (IC) and crushed caplets (CC).	91

Figure	LIST OF FIGURES (continued)	Page
IV.7	SEM's of the cross section of non-compacted Avicel PH-101 coated Multi-Layered Bead; magnification, A = 55 & B = 280.	92
IV.8	SEM's of the cross section of deformed Avicel PH-101 coated Multi-Layered Bead upon compaction at 100 lb..	93
IV.9	Effect of Avicel PH-101 coating as cushioning excipient on drug release from compressed Multi-Layered Beads.	94
V.1	Effect of polymer coat thickness on drug release from different size beads.	110
V.2	Effect of bead size on drug release from compressed beads at different compaction pressures.	111
V.3	Effect of pressure on drug release from formulation E and F compressed beads.	113
V.4	Scanning electron micrographs of formulation G, non-compacted beads and compacted beads (125 lb.).	114
V.5	Effect of Excipient/disintegrant coating on drug release from compressed formulation beads at different compaction pressures.	116
V.6	Effect of spray coated PEO on drug release from compressed beads.	118
V.7	Triple layered caplets: Effect of pressure with PEO layers (33%) on drug release from compressed beads.	120
V.8	Triple layered caplets: Effect of Avicel and PEO layers on formulation C compressed beads.	122
V.9	Triple layered caplets: Effect of Avicel and PEO layers on formulation E compressed beads.	123
V.10	Granulated bead compacts: Effect of compression of Avicel-granulated polymer-coated beads on drug release.	124

Table	LIST OF TABLES	Page
II.1	Upper Punch Compliance Constants for the Stokes B2 Rotary Tablet Press.	15
II.2	Absolute Value of Lower Punch Compliance Constants for the Stokes B2 Rotary Tablet Machine.	16
II.3	Absolute Value of Pooled Compliance and Hookian Constants for the Upper and Lower Punches of the Stokes B2 Rotary Tablet Press.	18
II.4	Dimensions and Definitions of Parameters for the Stokes B2 Rotar Tablet Press Fitted with IPT Standard Punch Heads.	27
II.5	The Nonelastic and Elastic Work of Compaction for the Loading, Dwell, and Unloading Phases, for Emcompress Compressed at Three Different Peak Pressures.	30
III.1	Summary of Maximum Von Mises Stresses for 1/16 and 1/8 inch Webs.	55
III.2	Initial and Terminal Slopes and Poisson's Ratio Calculated from Pressure-Cycle Curves.	63
IV.1	Formulation Compositions for the Multi-Layered Beads	81
IV.2	Formulation Compositions for the Multi-Layered Beads wit Avicel PH-101 as the outer layers.	82
IV.3	Spray coating conditions for the Multi-layered beads using a fluid-bed spray coater.	83
V.1	Percentage composition for the various compressed bead formulations.	106
V.2	Coating conditions for the various bead formulations on a Fluid-Bed spray coater.	107

Figure	LIST OF APPENDIX B FIGURES	Page
B.1	Traditional die design procedure (a) and the proposed optimal die design procedure ODP (b).	152
B.2	The Wheatstone bridge circuit.	159
B.3	Cylindrical die with a single active gage mounted horizontally on the die surface $r = r_e$ .	163
B.4	Distributions of the normalized radial stress $s_r/P_{max}$ , tangential stress $s_q/P_{max}$ and Von Mises stress $s_{vm}/P_{max}$ along a radial line for cylindrical die ( $r_i = 3 \text{ mm}, r_e = 9 \text{ mm}$ ).	169
B.5	Optimal die wall thickness (feasible wall thickness) for a cylindrical-shape die based on given design constraints and closed-form analytic analysis.	173
B.6	Finite element model of one-eighth of the symmetrical segmented die generated by COSMOS/M using 144 3D, 8-node, solid elements.	174
B.7	The symmetric segmented die; f: cut-away angle, t: effective wall thickness, and h: die height.	175
B.8	Maximum Von Mises stresses at a 120 MPa die-wall pressure for four cut-away angles ( $f = 30^\circ, 60^\circ, 90^\circ, 120^\circ$ ) and effective die-wall thicknesses ( $t = 1 \text{ mm} - 5 \text{ mm}$ ).	179
B.9	Die Wall Signals at a 120 MPa die-wall pressure for four cut-away angles ( $f = 30^\circ, 60^\circ, 90^\circ, 120^\circ$ ) and effective die-wall thicknesses ( $t = 1 \text{ mm} - 5 \text{ mm}$ ).	181
B.10	Dimensions of the segmented die ( $f = 30^\circ, t = 5 \text{ mm}, r_i = 11.2 \text{ mm}$ ) selected for finite element analysis with Hölzer and Sjögren's [19] strain gage configuration.	184

Figure	LIST OF APPENDIX B FIGURES (continued)	Page
B.11	Finite element model for tablet-compaction simulation using symmetric segmented die [19] with $f = 30^\circ$ , $t = 5$ mm and bore radius equal to 11.2 mm.	185
B.12	The Von Mises stress contour for symmetric segmented die at 120 MPa upper punch pressure.	188
B.13	Deformed shape of the symmetric segmented die generated by COSMOS/M at 120 MPa upper punch pressure.	189
B.14	Die wall signals at 120 MPa upper punch pressure for various lower punch positions and at constant compact height (4 mm).	190

Table	LIST OF APPENDIX A TABLES	Page
A.1	Punch displacement measurements at the <u>loading phase</u> with lower punch penetration setting of <u>6.99 mm</u> for the lower and upper punch of a Stokes B2 rotary tablet machine.	140
A.2	Punch displacement measurements at the <u>dwell phase</u> with lower punch penetration setting of <u>6.99 mm</u> for the lower and upper punch of a Stokes B2 rotary tablet machine.	141
A.3	Punch displacement measurements at the <u>unloading phase</u> with lower punch penetration setting of <u>6.99 mm</u> for the lower and upper punch of a Stokes B2 rotary tablet machine.	142
A.4	Punch displacement measurements at the <u>loading phase</u> with lower punch penetration setting of <u>11.05 mm</u> for the lower and upper punch of a Stokes B2 rotary tablet machine.	143
A.5	Punch displacement measurements at the <u>dwell phase</u> with lower punch penetration setting of <u>11.05 mm</u> for the lower and upper punch of a Stokes B2 rotary tablet machine.	144
A.6	Punch displacement measurements at the <u>unloading phase</u> with lower punch penetration setting of <u>11.05 mm</u> for the lower and upper punch of a Stokes B2 rotary tablet machine.	145
A.7	Punch displacement measurements at the <u>loading phase</u> with lower punch penetration setting of <u>14.06 mm</u> for the lower and upper punch of a Stokes B2 rotary tablet machine.	146
A.8	Punch displacement measurements at the <u>dwell phase</u> with lower punch penetration setting of <u>14.06 mm</u> for the lower and upper punch of a Stokes B2 rotary tablet machine.	147
A.9	Punch displacement measurements at the <u>unloading phase</u> with lower punch penetration setting of <u>14.06 mm</u> for the lower and upper punch of a Stokes B2 rotary tablet machine.	148



<b>Table</b>	<b>LIST OF APPENDIX B TABLES</b>	<b>Page</b>
<b>B.1</b>	<b>Definition and parameters used for the cylindrical die calculations.</b>	<b>165</b>
<b>B.2</b>	<b>D3 tool steel material properties used for stress/strain calculations.</b>	<b>168</b>
<b>B.3</b>	<b>Definition and parameters used for the segmented die calculations.</b>	<b>177</b>
<b>B.4</b>	<b>Definition and parameters used for Hölzer and Sjögren's segmented die calculations.</b>	<b>186</b>

# TABLET MACHINE INSTRUMENTATION TO STUDY TABLET COMPACTION AND COMPRESSION OF POLYMER COATED BEADS INTO TABLETS

## CHAPTER I

### INTRODUCTION

Punch displacement during tablet compaction is limited to only a few millimeters. Since compaction studies focus on very distances, any tablet machine deformation can lead to large errors in the determination of punch displacement. In chapter two, deformations that affect the vertical punch displacement of a Stokes B2 rotary tablet press were characterized (quantitated) with a cathetometer. With this information, correction factors for the punch displacement equations were developed, thus improving the accuracy of punch displacement calculations for tablet presses that undergo deformation. In addition, this study uses the work of compaction to examine the effect of press deformation on tablet compaction by factoring the Hookian spring constants into the calculation of the incremental work of compaction for dibasic calcium phosphate dihydrate and microcrystalline cellulose.

When designing a transducer for die wall stress measurements, two major concerns are the effects of tablet height and tablet position within the die on output signal. These factors make calibration and data interpretation more difficult because they interact, causing the transducer to have a non-linear output signal. To address

these concerns, in chapter three a split-web die concept is proposed for accurate measurements of radial die-wall stress (DWS) during tablet compaction. This design encloses the sensing web in a cylinder, thereby avoiding the sensing web binding caused by the standard die lockscrew. The optimal design process (ODP) described in Appendix B was used to determine the sensing web dimensions and strain gage arrangement that optimizes signal output. Finite element analysis (FEA) was used as a numerical tool for systematic optimization of the split-web die design. Radial versus axial transmission curves and residual die-wall stress measurements for some commonly used excipients were generated and compared with literature data to confirm the effectiveness and signal linearity of the transducer designed by the ODP.

Compression of polymer coated beads into tablets raises concerns regarding the loss of integrity of the polymer coat following compression, since coat integrity is necessary to serve as a diffusion barrier to delay drug release from these compressed tablets. Chapter four evaluates the effect of compression on beads with alternating multiple layers of polymer and drug coat, and the effect of cushioning excipients and compaction pressure on drug release from compressed bead formulations. This study also examines the utility of spray coating Avicel PH-101 as cushioning excipient onto polymer coated beads to eliminate the segregation problem associated with mixing of polymer-coated beads and cushioning excipients. In addition, the effect of cushioning excipient type and amount and compaction pressure on drug release from compressed multi-layered beads was investigated.

In chapter five, the effect of bead size on compression and subsequent drug release was investigated using 45/60 mesh Nu-pariel beads instead of 25/30 mesh as used in experiments in chapter three. Four new concepts were developed and evaluated in the development of rapidly disintegrating polymer coated bead compacts i.e. Excipient / disintegrant coated compacts, Sealant-effect compacts, Triple-layered caplets, and Granulated bead compacts. The effect of polymer coat thickness, cushioning excipients, and compaction pressure on drug release from compressed bead formulations was also investigated.

## CHAPTER II

### DEFORMATION OF THE STOKES B2 ROTARY TABLET PRESS: QUANTITATION AND INFLUENCE ON TABLET COMPACTION

Syed A. Altaf and Stephen W. Hoag

Journal of Pharmaceutical Sciences, March 1995

## ABSTRACT

Deformations that affect the vertical punch displacement of a Stokes B2 rotary tablet press were characterized with a cathetometer. The press deformation was found to be elastic for both the upper and lower compression roller assemblies. However, the upper and lower compression roller assemblies have different Hookian spring constants:  $8.58 \times 10^4$  and  $5.18 \times 10^4$  kN/m for the upper and lower assemblies, respectively. Using two-way analysis of variance, the Hookian spring constants were shown to be independent of compaction phases and lower punch penetration setting. To study the influence of press deformation on tablet compaction, the Hookian spring constants were factored into the calculation of the incremental work of compaction for dibasic calcium phosphate dihydrate and microcrystalline cellulose. As the peak compression pressure increases, the force-displacement work done on the tablet during the loading phase decreases relative to calculations that neglect press deformation. This decrease in force-displacement work was attributed to elastic press deformation, which absorbs energy during the loading phase and then releases this energy later in the compaction cycle, altering the punch-displacement profile. The rate at which the press stores and releases elastic energy depends in part upon the viscoelastic properties of the tablet. Based upon these results, the coupling between press elasticity and a tablet's viscoelastic properties should be accounted for when analyzing tablet compaction or trying to simulate the punch-displacement profile of a tablet press that deforms during compaction.

## INTRODUCTION

The analysis and modeling of tablet compaction requires an accurate knowledge of the punch displacement during compaction. Punch displacement can be measured on a rotary tablet press using commercially available displacement transducers (1). However, these measurements are difficult to perform, because a relatively high frequency signal must be obtained from a rotating turret. These difficulties were avoided by Rippie and Danielson (2), who derived an equation that calculates punch displacement. This equation has been widely used; however, for the equation to be valid, the compression rollers must be in horizontal alignment and the components of the tablet press which affect punch displacement must not deform. Since compaction studies focus on very small distances, tablet press deformation can lead to errors in punch displacement calculation.

At present, very little quantitative data have been collected on tablet press deformation. Early studies of press deformation focused on single-punch presses. One of the first quantitative studies was done by Lammens et al. (3,4) who developed an equation that corrects the measured displacement from an inductive displacement transducer for the elastic deformation of a single-punch press; a similar approach was also used by Juslin and Paronen (5). Kennerley et al. (6) used a cathetometer and linear variable differential transformer (LVDT) to determine the Hookian constants for

instrumented Manesty E2 and F3 tablet presses. Later studies examined the deformation of rotary tablet presses (7,8) and compaction simulators (9). One of the most complete studies was done by Oates and Mitchell (10). They were able to measure significant press deformation for the Manesty Betapress. They found that the upper compression roller assembly deflects linearly with vertical punch force and accounts for approximately 35% of the total press deformation. The remaining 65% of the machine deflection occurs in the lower compression roller assembly and also varies linearly with applied punch force.

While studying the work of compaction on a Stokes B2 rotary tablet press, Hoblitzell and Rhodes (11) raised concerns regarding errors in punch displacement calculations due to press deformation; however, they had no quantitative data to support their assumption. Because press deformation is important for the study of tablet compaction and no quantitative data exists on the deformation of the Stokes B2 tablet press, the purpose of the present study is to quantitate the deformation of the Stokes B2 rotary tablet press. With this information, correction factors for the punch displacement equations will be developed, thus improving the accuracy of punch displacement calculations for tablet presses that undergo deformation. In addition, this study will use the work of compaction to examine the effect of press deformation on tablet compaction.



## EXPERIMENTAL

### Tablet Machine Instrumentation

Measurements were done on a Stokes-B2 16 station rotary tablet press (F.J. Stokes Machine Co., Philadelphia, PA) equipped with "standard IPT head"  $3/8$  in. flat faced punches. The ejection cam was removed to facilitate measurements. Lower punch stress was measured with an instrumented compression roller pin (Specialty Measurements Inc., Pittstown, NJ). To measure upper punch stress, the opposite sides of the upper punch were ground flat, and two bonded electrical resistant strain gages were mounted on each side of the upper punch, approximately 5 cm from the tip. The two strain gages were connected to an opposite arm Wheatstone bridge to cancel out bending motions introduced by the compression rollers. The upper punch and roller pin were connected by a cable to a signal conditioning amplifier (model 2310, Measurements Group Inc., Raleigh, NC). The punches were calibrated with a compression load cell (model 3174, Eaton Corp., Troy, MI) and a Carver hydraulic press. The punch calibration was linear from 0 to 300 MPa with an  $R^2 = 0.99999$ , and the intercept was statistically insignificant from zero. The turret angular velocity ( $\omega$ ) and the time at which top dead center occurred were measured by a magnetically triggered digital proximity switch and aligned magnets mounted on the turret. The signals from the punch, instrumented roller pin, and proximity switch were sent to a personal computer interfaced with a 12 bit 100 kHz analog to digital (A/D) converter

(model AT-MIO-16, National Instruments Corp., Austin, TX). To maintain compression roller alignment, the eccentric cam of the upper compression roller pin was fixed at the 3.175 mm penetration setting.

#### Tablet Machine Deformation Measurement

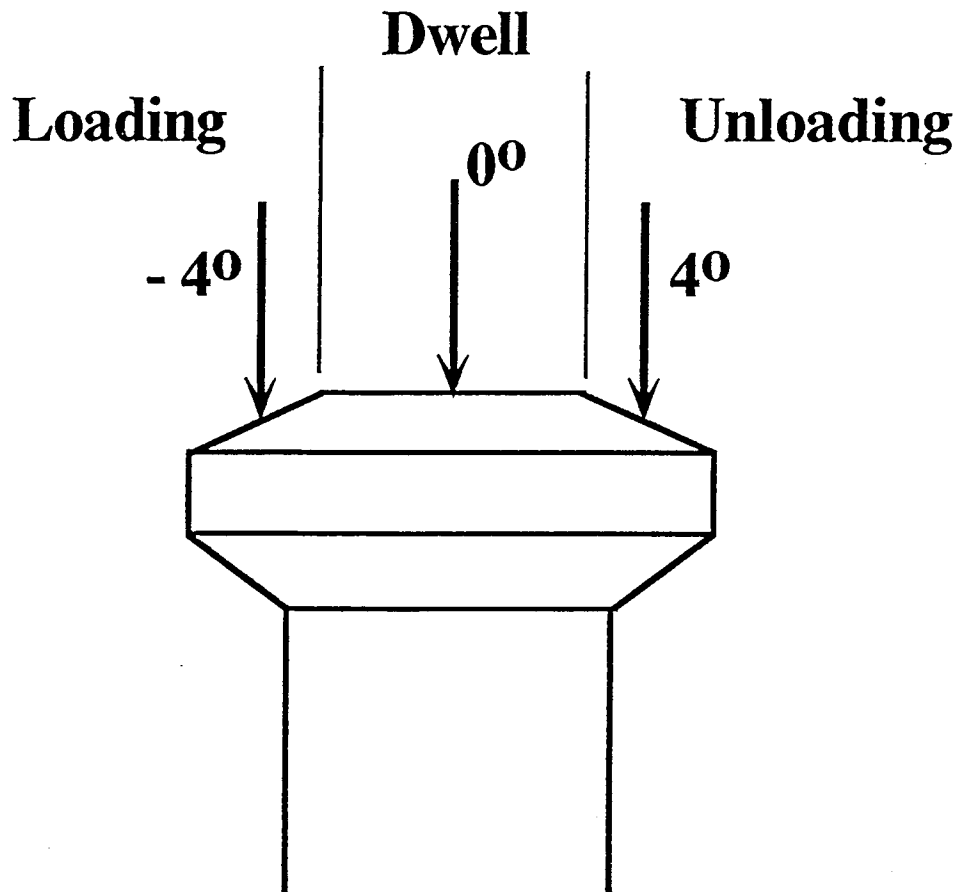
A cathetometer (model M912, Gaertner Scientific Corp., Chicago, IL) was used to measure the distance between reference marks inscribed on the barrel of the upper punch (ca. 2 cm from the tip) and on the neck of the lower punch. The cathetometer consists of a telescope mounted on a vertical meter rod inscribed with a scale and vernier that can take a vertical position reading with an accuracy of 0.01 mm. To assure accurate measurements, the precise leveling of the meter rod frame, elimination of the telescope parallax error, and focusing were carried out according to the manufacturer's specifications. Before readings can be taken, the upper and lower punch barrels must be lubricated. The upper punch position is determined by sighting the cathetometer on the upper punch reference mark, and reading the corresponding position from the vernier scale. Then the telescope is moved down the meter rod, the cathetometer is sighted on the lower punch reference mark, and the corresponding vertical position is recorded. Three readings were taken in this same sequence at pressures of 50, 100, 150, 200, and 250 MPa (pressures that do not trigger the overload spring). These pressures were generated by placing a combination of different

sized rubber plugs into the die and then manually rotating the turret until the punch and die are between the compression rollers; readings were not taken for 5 min. after applying pressure to allow for plug stress relaxation. By measuring the time it took for the rubber plugs to reach stress equilibrium, it was found that 5 min. was more than sufficient to allow for stress relaxation. Therefore, the stress was virtually constant during the measurement period. Readings were taken with the compression roller positioned on the punch head at top dead center  $0^{\circ}$  (dwell), and at  $-4^{\circ}$  (loading) and  $4^{\circ}$  (unloading) of turret rotation from top dead center (see Figure II.1). The loading, roll-on, dwell, roll-off, and unloading are shown in Figure II.1.

To confirm the cathetometer data, press deformation was also characterized by measuring the height of lead compacts compressed to different pressures. The lead compacts were made by placing an exact amount of lead into the die and manually rotating the turret to top dead center, as described above. After this position was held for 60 s, the corresponding pressure was recorded. The lead compact was then removed from the die, and its height was measured with a micrometer. Each piece of lead was only compressed once.

### Tablet Compaction

Tablets were made from dibasic calcium phosphate dihydrate (Emcompress, Edward Mendell Co., Patterson, NY) and microcrystalline cellulose (Avicel PH-101, FMC Corp., Philadelphia, PA). Before compaction, the die wall was lubricated by



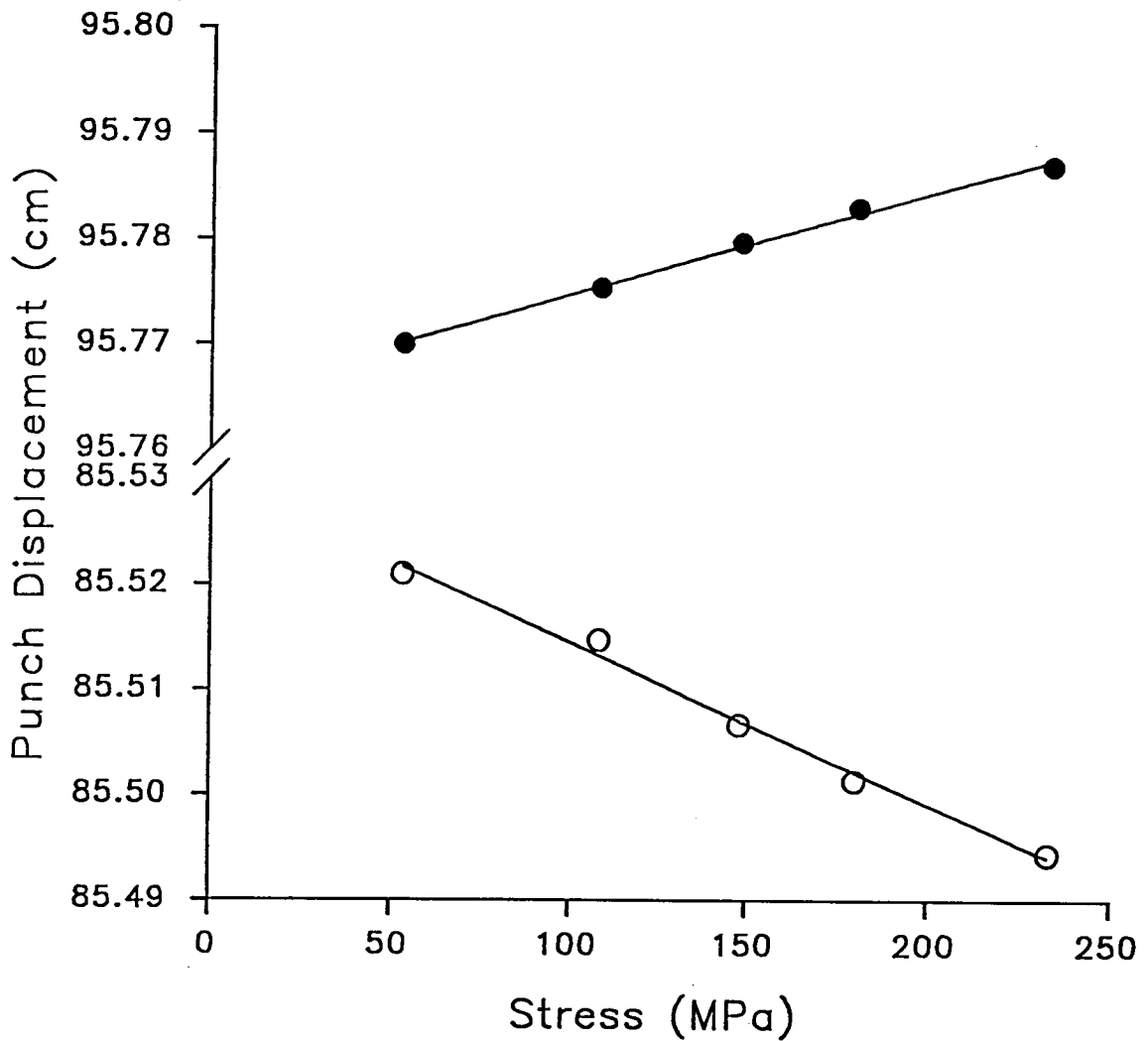
II.1 Schematic of punch head, the arrows denote the position of the compression roller when readings were taken for the loading, dwell, and unloading phases. The angles give the degrees of turret from top dead center, and roll-on and roll-off are indicated by the vertical lines.

swabbing a 20% (w/v) magnesium stearate-2-propanol slurry onto the die wall; the alcohol was evaporated prior to compaction.

## RESULTS AND DISCUSSION

### Tablet Machine Elasticity

Figure II.2 shows the results of the tablet press deformation study done with the cathetometer. When the axial stress on the punch was increased from 50 to 250 MPa, the separation between the upper and lower punches increased by 0.44 mm, clearly indicating that the Stokes B2 tablet press deforms. To determine if the press deformation is linear, a t-test with a null hypothesis of independence (i.e., no linear correlation) in a bivariate normal population was used (12). The rejection of the null hypothesis (even at a significance level of 0.001) and the coefficient of determination ( $r^2 = 0.998$ ) for both the upper and lower punches gives strong evidence of linear press deformation. Equivalent results were found for all press deformation data in this study. The linear deformation clearly indicates that the Stokes B2 tablet press behaves like a Hookian spring, where the slope of the line in Figure II.2 is the compliance ( $k$ ) or reciprocal of the elastic Hookian spring constant ( $Y$ ). Because the deforming elements of the tablet press are a composite of different parts with different cross sectional areas and lengths, Young's elastic modulus cannot easily be calculated; therefore, the Hookian notation will be used.



II.2 Punch separation for the upper (●) and lower (○) punches versus punch stress (error bars within symbols). The data was collected at top dead center, and the punch penetration was set at 3.175 and 14.06 mm for the upper and lower punches, respectively.

The 0.44 mm tablet press deformation resulted from a 0.17 and 0.27 mm punch movement for the upper and lower punches, respectively. The greater displacement of the lower punch suggests that the upper and lower compression roller assemblies have different Hookian spring constants. This was confirmed by a paired Student's t-test done on the difference between the absolute values of the slopes for the upper and lower punch data. A significant difference ( $p = 0.0001$ ) strongly suggests that the upper and lower punch assemblies are not symmetric.

To determine if the upper and lower Hookian spring constants change during the compaction cycle and with different lower punch penetration (eye-bolt) settings, they were measured for the loading, dwell, and unloading phases of compaction and for three different lower punch penetration settings. The upper punch penetration was fixed because changing its setting could result in horizontal misalignment of the upper and lower punches by as much as 3.175 mm. The elastic constants obtained by linear regression of punch displacement versus punch stress are shown in Tables II.1 and II.2. The reported error is the standard error of the slope. The data in Tables II.1 and II.2 were analyzed by two-way analysis of variance (ANOVA), using the SAS statistical software package. A P-value of less than 0.05 was considered significant. The two-way ANOVA results showed no difference in slopes among the three phases of tablet compaction for both the upper and lower punches ( $P > 0.1$ ). The lower punch penetration settings had no effect on the elastic constants ( $P > 0.05$  for the upper and  $P > 0.1$  for lower punch). The interaction between the phase of compaction and punch penetration setting was not significant for both the upper and

Table II.1 Upper Punch Compliance Constants for the Stokes B2 Rotary Tablet

Press ( $\pm$  indicates standard error).

Lower Punch  Penetration  (mm)	Phase $\times 10^{-5}$ (m/kN)		
	Loading	Dwell	Unloading
6.99	1.01 $\pm$ 0.09	1.18 $\pm$ 0.11	1.24 $\pm$ 0.05
	1.33 $\pm$ 0.03	1.00 $\pm$ 0.05	1.41 $\pm$ 0.23
	1.08 $\pm$ 0.04	1.01 $\pm$ 0.04	1.31 $\pm$ 0.09
11.05	1.09 $\pm$ 0.05	1.26 $\pm$ 0.10	1.34 $\pm$ 0.16
	1.14 $\pm$ 0.06	0.94 $\pm$ 0.10	1.00 $\pm$ 0.06
	1.43 $\pm$ 0.03	1.05 $\pm$ 0.10	1.32 $\pm$ 0.15
14.06	1.13 $\pm$ 0.08	1.17 $\pm$ 0.16	1.27 $\pm$ 0.09
	1.17 $\pm$ 0.15	1.15 $\pm$ 0.23	1.18 $\pm$ 0.20
	1.50 $\pm$ 0.03	1.07 $\pm$ 0.08	1.18 $\pm$ 0.09



Table II.2 Absolute Value of Lower Punch Compliance Constants for the Stokes B2 Rotary Tablet Machine ( $\pm$  indicates standard error).

Lower Punch Penetration (mm)	Phase x 10 <sup>-5</sup> (m/kN)		
	Loading	Dwell	Unloading
6.99	2.15 $\pm$ 0.11	1.60 $\pm$ 0.21	1.96 $\pm$ 0.09
	1.96 $\pm$ 0.09	1.52 $\pm$ 0.08	1.98 $\pm$ 0.14
	1.82 $\pm$ 0.13	2.11 $\pm$ 0.22	2.11 $\pm$ 0.08
11.05	1.68 $\pm$ 0.10	2.11 $\pm$ 0.11	2.02 $\pm$ 0.27
	1.68 $\pm$ 0.08	1.96 $\pm$ 0.11	1.96 $\pm$ 0.15
	2.17 $\pm$ 0.19	2.11 $\pm$ 0.06	2.19 $\pm$ 0.15
14.06	1.96 $\pm$ 0.06	1.66 $\pm$ 0.12	1.89 $\pm$ 0.10
	2.18 $\pm$ 0.15	2.11 $\pm$ 0.10	2.20 $\pm$ 0.11
	2.01 $\pm$ 0.20	1.68 $\pm$ 0.06	1.94 $\pm$ 0.13

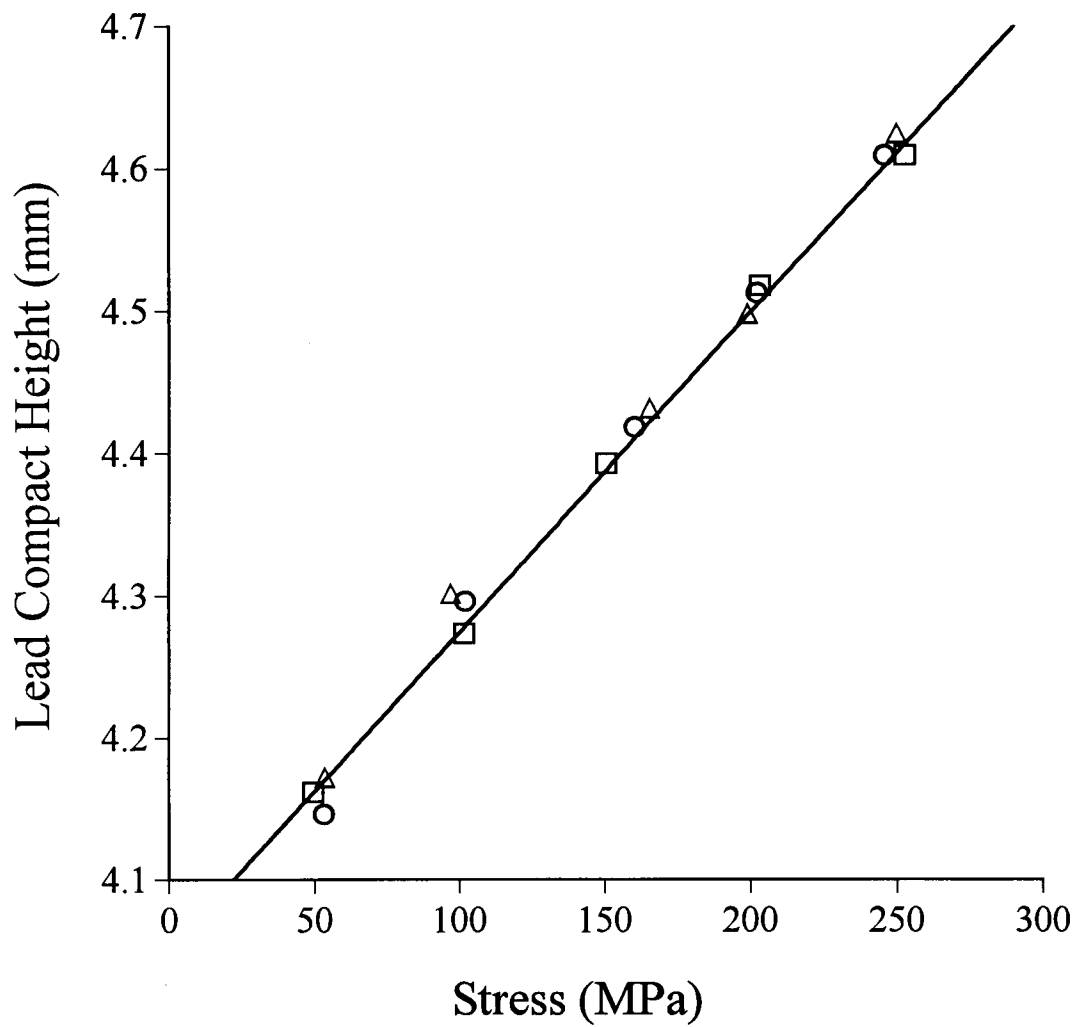
lower punches ( $P > 0.1$ ). For the results of a two-way ANOVA to be valid, the data in Tables II.1 and II.2 must be normally distributed and the variances must be homogeneous. Both of these assumptions were checked and found to be valid. Thus, it can be concluded that for the Stokes B2, press deformation can be characterized by two different elastic constants, one for the upper and one for the lower compression roller assemblies. Both of these elastic constants are independent of compaction phase and lower punch penetration setting. Because the elastic constants do not change, the data in Tables II.1 and II.2 were pooled and summarized in Table II.3. The individual runs for all the compaction phases at different lower punch penetration settings and their statistics are summarized in Appendix A.

Figure II.3 plots the lead compact height versus the punch stress. As the consolidation pressure increases from 50 to 250 MPa, the average height of the compact increased by 0.456 mm and the average coefficient of determination between punch stress and compact height was  $R^2 = 0.995$ . The 0.456 mm average increase in lead compact height is only 3.6% different from the 0.44 mm increase in punch separation measured with the cathetometer. This small 3.6% difference independently confirms the data collected with a cathetometer, and the  $R^2 = 0.995$  confirms the finding of elastic press deformation.

The data clearly show that for pressures between 50 and 250 MPa, the Stokes B2 tablet press undergoes elastic deformation that can be described by two elastic constants that are unchanged by compaction phase or lower punch penetration setting. As pointed out by several authors, there are difficulties in extrapolating the elastic

Table II.3 Absolute Value of Pooled Compliance and Hookian Constants for the Upper and Lower Punches of the Stokes B2 Rotary Tablet Press ( $\pm$  indicates standard error).

Constant	Punch	
	Upper	Lower
Compliance ( $k$ ) (m/kN) ( $\times 10^{-5}$ )	1.18 $\pm$ 0.15	1.95 $\pm$ 0.20
Hookian ( $Y$ ) (kN/m) ( $\times 10^4$ )	8.58 $\pm$ 1.05	5.18 $\pm$ 0.57



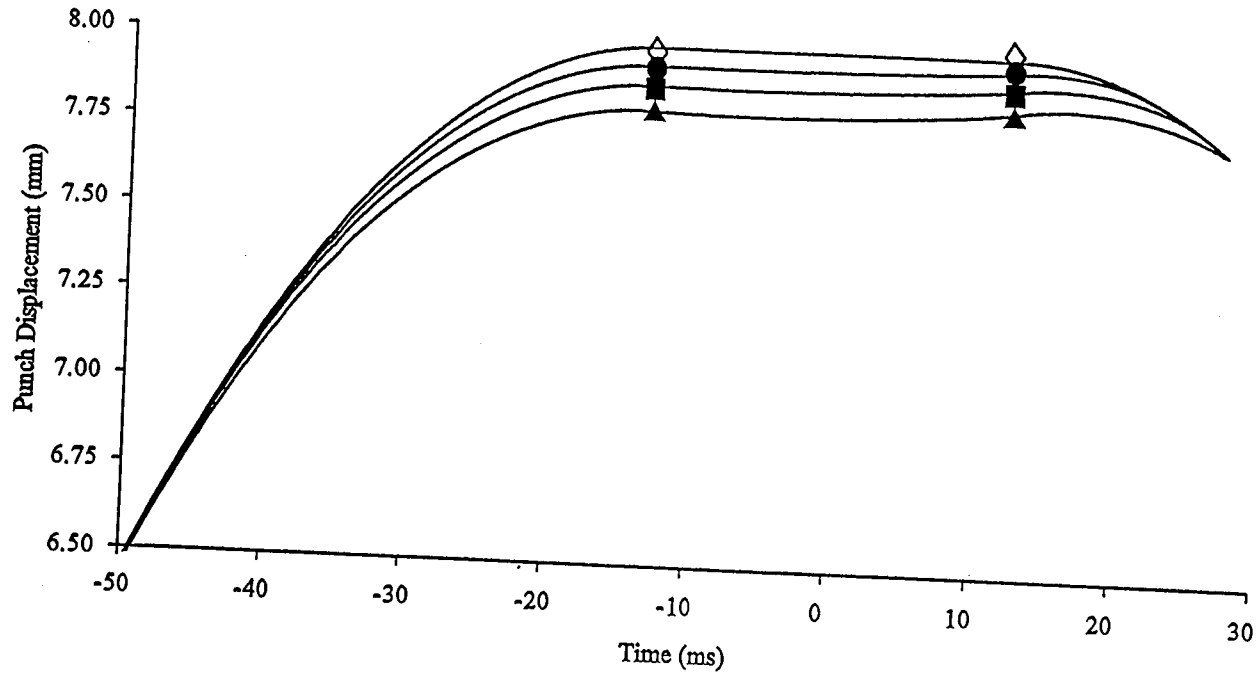
II.3 Height of lead compact versus applied punch stress. Each symbol set represents an individual run or replicate.

constants outside this range. Oats and Mitchell (10) found a change in the slope of the press deflection versus punch force at approximately 2.3 kN (32 MPa with  $3/8$  in. tooling). Juslin and Paronen (5) also found a similar two phase profile in a single station press with the change in slope occurring at pressures less than 5 MPa, they attributed the change in slope to machine "looseness." Although the elastic constants for deformations less than 50 MPa are probably different from those for deformations greater than 50 MPa; in the present study, the difference was neglected when calculating the work of compaction. In addition, the reported elastic constants in Table II.3 are not valid for pressures greater than 275 MPa because the press's deformation character (slope in Figure II.2) starts to change.

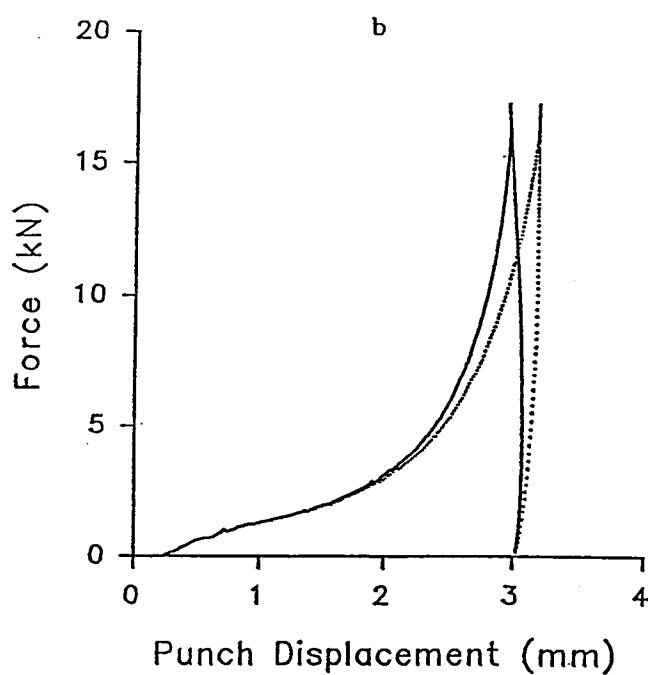
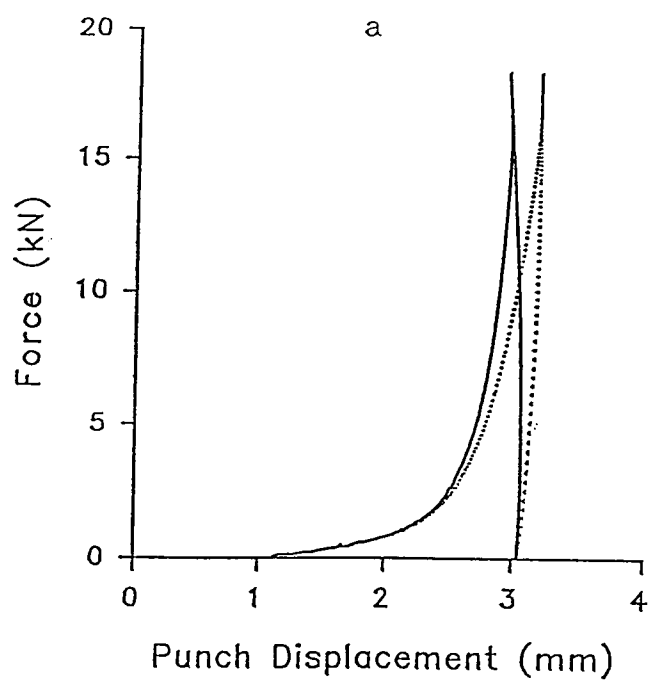
The elastic constants obtained in this paper are specific to the Stokes B2 rotary tablet press. The elastic constants reflect press construction; thus, the constants reported in Table II.3 cannot be generalized to different types of tablet presses. For example, when Hoag and Rippie (13) tried to measure the deformation of the Colton 216 rotary tablet press with a cathetometer, they could not measure any deformation in the range from 0 to ca. 15 kN. It should be noted that all of their studies were done with loads less than 15 kN. However, when Walter and Augsburg (7) measured punch displacement into the die for the Colton 216 with a LVDT, they found that there was press deformation in the 0–25.1 kN load range. Some of the differences between the two studies can be attributed to the higher loads used by Walter and Augsburg. In addition, when Oates and Mitchell (10) measured deformation of the Manesty Betapress with an LVDT, they found a Hookian compliance constant for the lower

compression roller assembly ca. 25% smaller ( $1.5 \times 10^{-5}$  m/kN) than the compliance of the Stokes B2. The upper compression roller assembly also has a Hookian compliance constant ca. 25% smaller ( $8.5 \times 10^{-6}$  m/kN) than the compliance of the Stokes B2. Thus, the Manesty Betapress is a stiffer tablet press than the Stokes B2.

One concern about static press deformation measurements made with a cathetometer is whether these measurements can be used to predict dynamic press deformation during tablet compaction. The authors feel this assumption is appropriate because elastic deformation is a very rapid, time independent process. In addition, the results in this study are consistent with three other similar studies in which dynamic measurements of press deformation were actually made for different types of tablet presses. First, Oates and Mitchell (10) used an LVDT to make dynamic measurements of punch displacement with increasing punch pressure. They found that the Manesty Beta press behaved elastically, the elastic constants did not change with the phase of compaction, and the upper and lower compression roller assemblies have different elastic constants. Second, Walter and Augsburg (7) measured punch displacement for a Colton 216 with an LVDT, and found vertical punch movement on the flat very similar to the calculated displacements shown in Figure II.4. Third, the force-displacement curves in Figure II.5 show a similar behavior to those obtained by Muller and Schierstedt (8): The consistency of our results with these studies helps to validate the use of elastic constants measured with a cathetometer to dynamic situations. In



II.4 Punch displacement corrected for press deformation versus time for the lower punch; the maximum punch stresses were 0 MPa (◇), 65 MPa (●), 135 MPa (■), and 225 MPa (▲). Top dead center occurs at the time axis origin; the symbols plotted on each line mark the beginning and end of the dwell phase.



II.5 Force-displacement profile showing the nonelastic (...) and elastic (—) curves for (a) Emcompress and (b) Avicel PH-101



addition, a unique advantage of this study is that the cathetometer measures press deformation from an external reference frame that is completely independent of any press deformation; this eliminates measurement errors caused by transducers fixed to deforming reference frames. This can be a problem as pointed out by Ho (14); Juslin and Paronen (5); and Lammens (3,4); who developed equations for the correction of LVDT displacement readings for press deformation.

#### Punch Displacement Equations Corrected for Elastic Deformation

On the basis of punch head geometry, tablet compaction can be separated into the loading, dwell, and unloading phases, see Figure II.1. The transition between these phases occurs when the compression roller rolls off or onto the flat portion of the punch head, which either begins or ends the dwell phase. The vertical punch displacement ( $z$ ) for loading (ld) and unloading (ul) can be calculated *via* the equations developed by Rippie and Danielson (2):

$$z_{ld} = z_{\max} - \left[ (r_1 + r_2)^2 - (r_3 \sin \omega t + x_2)^2 \right]^{1/2} \quad (1)$$

$$z_{ul} = z_{\max} - \left[ (r_1 + r_2)^2 - (r_3 \sin \omega t - x_2)^2 \right]^{1/2} \quad (2)$$

During the dwell phase (dw), when the compression roller is on the flat portion of the punch head, the vertical punch displacement is constant:

$$z_{dw} = z_{\max} + r_1 + r_2 \quad (3)$$

The notation used in Equations 1-3 is the same as reference 2; the definition of parameters and dimensions for a Stokes B2 tablet press fitted with IPT standard punch heads are listed in Table II.4. The term  $z_{\max}$  in Equations 1-3 normalizes the punch displacement so that zero penetration occurs when the punch tip is even with the die face. The maximum punch extension ( $z_{\max}$ ) is given by the combined length of the compression roller radius, punch head curvature radius, and punch penetration setting:

$$\text{upper punch} \quad z_{\max} = z_{ec} - r_1 - r_2 \quad (4a)$$

$$\text{lower punch} \quad z_{\max} = z_{eb} - r_1 - r_2 \quad (4b)$$

where  $R_{ec}$  and  $R_{eb}$  are the punch penetration settings for the eccentric cam (ec) of the upper compression roller pin and the eye bolt (eb) position setting for the lower punch, respectively.

To account for tablet press deformation, the elastic stretch is subtracted from Equations 1-3. As pointed previously, there are different elastic constants for the upper and lower compression roller assemblies. Therefore, six equations are required to calculate the upper (up) and lower (lr) punch displacement for the three phases of compaction

	Loading phase	Dwell	Unloading phase	
Upper punch	$z = z_{ld} - k_{up} F_{zz}$	$z = z_{dw} - k_{up} F_z$	$z = z_{ul} - k_{up} F_{zz}$	(5a)

Lower punch	$z = z_{ld} - k_{lr} F_z$	$z = z_{dw} - k_{lr} F_{zz}$	$z = z_{ul} - k_{lr} F_{zz}$	(5b)
-------------	---------------------------	------------------------------	------------------------------	------

where  $k$  is the compliance from Table II.3 and  $F_{zz}$  is the axial punch force. The calculated lower punch displacements (Equation 5b) versus time are plotted in Figure II.4 for Emcompress compacted to maximum pressures of 65, 135, and 225 MPa. As shown in Figure II.4, the two main effects of press deformation are to (1) decrease punch penetration into the die and (2) change the punch displacement during the dwell phase, rather than it remaining constant.

#### Work of Compaction and Press Deformation

In this section the work of compaction will be used to examine the influence of press deformation on tablet compaction. The work of compaction ( $W$ ) can be calculated from the area under the force-displacement curve by using the trapezoidal rule:

$$W = -\frac{1}{2} \sum_{i=1}^N (F_{i+1} + F_i)(z_{i+1} - z_i) \quad (6)$$

This was done for Emcompress and Avicel, Figure II.5, parts a and b, respectively. To examine the work of compaction in more detail, the incremental work of compaction was plotted versus time for Emcompress compacted to maximum pressures of 65, 135, and 225 MPa (see Figure II.6). The incremental work is the amount of work done by the tablet during the  $i$ th interval (100 ms) of Equation 6. The loading, dwell, and unloading phases are shown as regions A-B, B-C, and C-D, respectively, in Figure II.6. In Equation 6 the displacement into the die ( $z$ ) and the punch force ( $F$ ) are defined as always positive.

**Table II.4 Dimensions and Definitions of Parameters for the Stokes B2 Rotary Tablet Press Fitted with IPT Standard Punch Heads.**

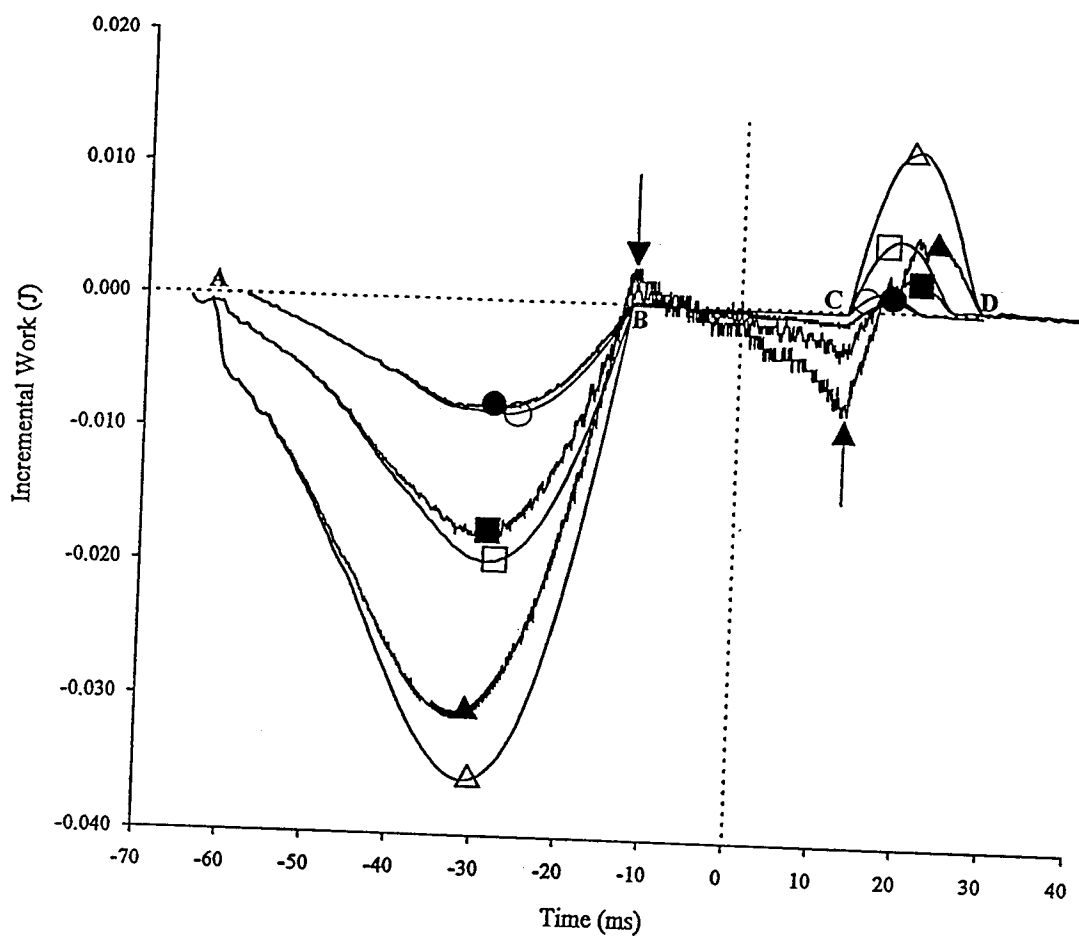
<b>Parameter</b>	<b>Dimension</b>
Die table radius ( $r_3$ )	114.30 mm
Compression roller radius ( $r_1$ )	101.60 mm
Punch head curvature radius ( $r_2$ )	7.9375 mm
Punch head flat radius ( $x_2$ )	6.35 mm
Angular turret velocity ( $w$ )	rad/s
Time ( $t$ )	ms

The work calculated by Equation 6 is the work done by the tablet. Thus, when the incremental work displayed in Figure II.6 is negative, the press is doing force-displacement work on the tablet; when the incremental work is positive, the tablet is doing force-displacement work on the press.

In the following three parts of the discussion, the incremental work of compaction for Emcompress will be examined with and without the influence of press deformation.

#### Loading Phase

If there was no press deformation during the loading phase (region A-B), all of the available energy would flow into the tablet *via* force-displacement work done by the punches. However, when there is press deformation as shown in Figure II.6, there is less energy input into the tablet because the press's components stretch, which decreases the punch penetration into the die. At a peak pressure of 225 MPa, including press deformation in the displacement calculation reduces the calculated force-displacement work by 13.4% (see Table II.5). At lower pressures, the force-displacement work was decreased by 9.6% and 5.2% for peak pressures of 135 and 65 MPa, respectively (see Table II.5). The energy required to deform the tablet press is converted to stored elastic energy within the deforming elements of upper and lower compression roller assemblies. Because stored elastic energy is conserved, this energy will be returned to the tablet later in the compaction cycle.



- II.6 For Emcompress, lower punch incremental work versus time for the three phases of tablet compaction, i.e. loading (A-B), dwell (B-C), and unloading (C-D), and for three different maximum pressures. Maximum compression stresses were (nonelastic curves open symbols/elastic curves, closed symbols) 65 MPa (O/●), 135 MPa (□/■), and 225 MPa (△/▲). Top dead center occurs at the time axis origin, and the arrows point to the beginning and end of the dwell phase.

Table II.5 The Nonelastic and Elastic Work of Compaction for the Loading, Dwell, and Unloading Phases, for Emcompress Compressed at Three Different Peak Pressures ( $P_{\max}$ )<sup>a</sup>

$P_{\max}$ (MPa)	Type	Work energy (J)			
		Loading	Dwell	Unloading	Total
65	Nonelastic	-2.2741	0.0000	0.0963	-2.1783
	Elastic	-2.1545	-0.0724	0.0486	-2.1783
135	Nonelastic	-5.3577	0.0000	0.4829	-4.8767
	Elastic	-4.8425	-0.2439	0.2097	-4.8767
225	Nonelastic	-10.5620	0.0000	1.3039	-9.2581
	Elastic	-9.1395	-0.5974	0.4788	-9.2581

<sup>a</sup> The elastic dwell phase was integrated from roll-on to the time at which elastic curves crosses the x-axis. The nonelastic dwell phase was integrated from roll-on to roll-off.

### Dwell phase

If there were no press deformation during the dwell phase (region B-C), there would be no force-displacement work done on or by the tablet since punch displacement is held constant by virtue of the compression rollers being on the punch flat. During the dwell phase, the pressure on the tablet causes viscoelastic flow and creep to occur within the tablet. However, when there is press deformation, the viscoelastic flow and creep leads to the further consolidation of the tablet, allowing the press to release some of its stored elastic energy. As shown in Figure II.6, the incremental work curves that exclude press deformation equal zero during the dwell phase, indicating that no work is being done on the tablet; the curves that include press deformation become increasingly negative as the dwell phase progresses, indicating that work is still being done on the tablet by the press. The amount of work done on the tablet by the press during the dwell phase is proportional to the amount of energy stored by the press, which is in turn proportional to peak punch pressure (see Table II.5).

For the Stokes B2 press, the maximum punch pressure ( $P_{\max}$ ) typically occurs during the dwell phase shortly after roll-on. This indicates that the punch stress is increasing while the vertical punch velocity is decreasing or becoming approximately constant; as a result, the incremental work calculated by Equation 6, becomes positive near the beginning of the dwell phase (see Figure II.6). As shown by Morehead and Rippie (15) for viscoelastic materials, the maximum pressure should occur when the strain rate is at or near a maximum. Thus, the authors believe that the reason that  $P_{\max}$



occurs during the dwell phase is not a result of the tablet's viscoelastic properties, but is a result of a mechanical process occurring within the tablet press during compaction.

For example, torsional stresses or bending moments on the tablet press frame that developed during the loading phase may be released during the initial dwell phase when nonaxial stresses are reduced, causing  $P_{\max}$  to occur during the initial dwell phase.

Because the positive area at the beginning of the dwell phase is very small, the authors believe that this effect has little influence on tablet compaction or the analysis of compaction.

#### Unloading Phase

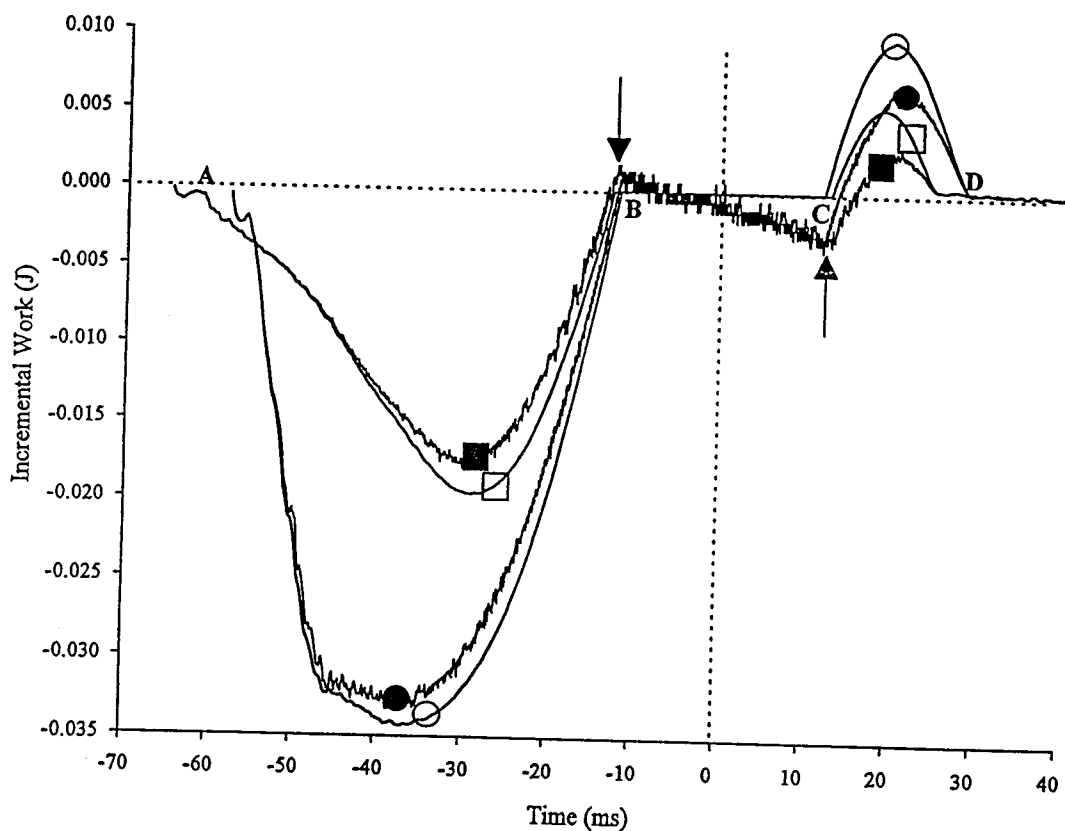
If there was no press deformation during the unloading phase (region C-D), the kinematics of the tablet press dictate that the punches would immediately begin to separate at roll-off, in a manner described by Equation 2. Increasing the punch separation allows the tablet to expand, releasing a portion of its stored elastic energy by doing force-displacement work on the press. However, when there is elastic press deformation, the press elasticity extends the time before the tablet starts to release its stored elastic energy (see Figure II.6). This extension of the dwell phase occurs because the kinematic punch separation that occurs at roll-off (described by Equation 2) is offset by press elasticity, which brings the punches together faster than the press kinematics can separate them, the net effect being the further consolidation of the tablet. Thus, force-displacement work is still flowing into the tablet from the tablet press. As shown in Figure II.6, the nonelastic curves immediately become

positive at roll-off, while the elastic curves remain negative and slowly tend towards positive values, a process which takes about 4 ms for a peak pressure of 225 MPa. The elastic curves cross the  $x$ -axis when enough of the press's stored energy has been released, so the forces exerted by the press are less than the forces exerted by the tablet; at this point no further consolidation of the tablet occurs and the kinematic motions of the press cause the punches to separate, which allows the tablet to expand and do force-displacement work on the press. In addition to extending the dwell phase, the amount of force-displacement work done by the tablet during unloading is less in the presence of press elasticity (Table II.5).

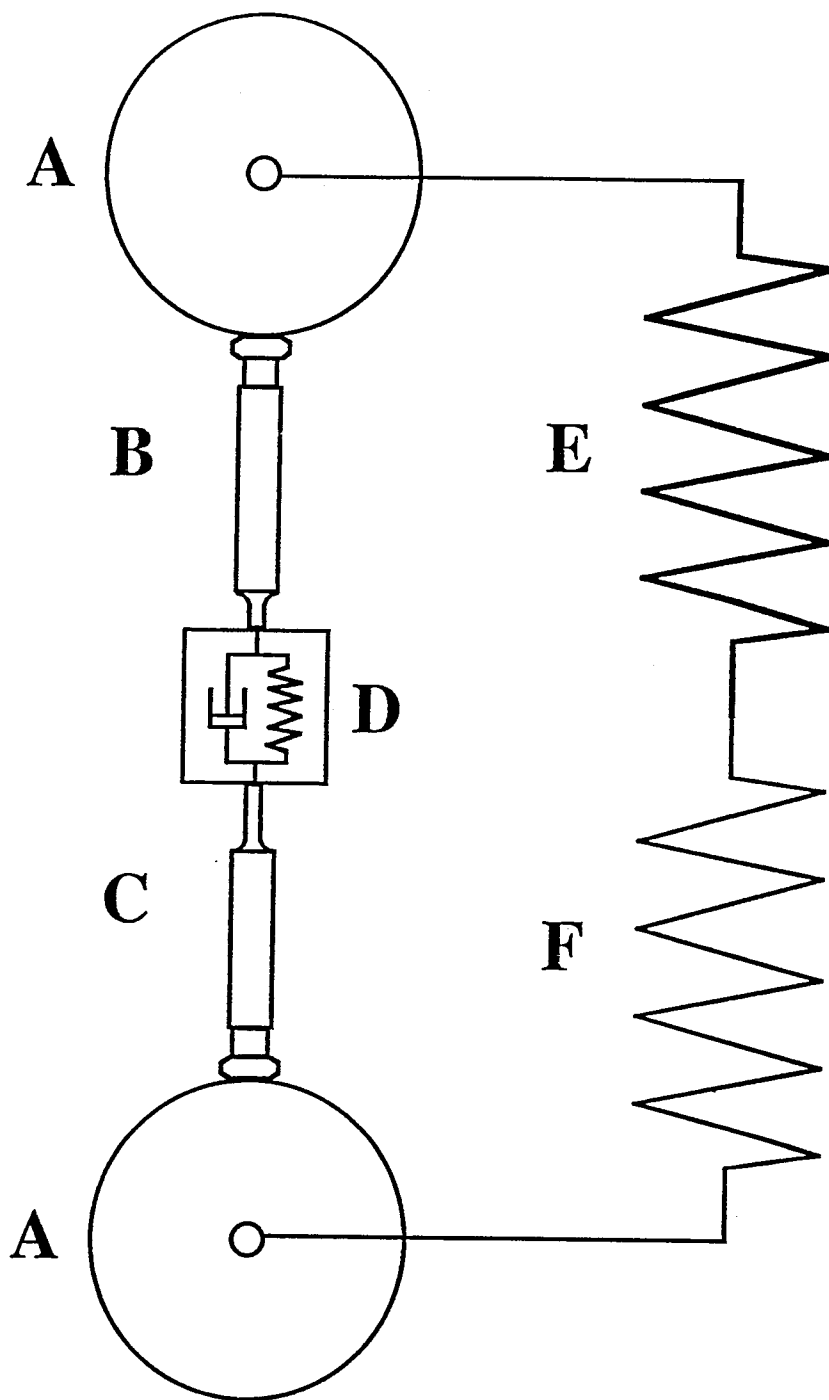
#### Summary

When there is elastic press deformation, the press stores some of the available energy, reducing the amount of work that can be done on the tablet during the loading phase. As discussed previously, this stored energy is returned as force-displacement work done on the tablet during the dwell phase and the initial portion of the unloading phase (Figure II.6). As predicted by elasticity theory, the total force-displacement work resulting from press deformation during the complete compaction cycle is zero because elastic deformations are reversible. Thus the work of compaction (Equation 6) for the complete cycle does not depend upon press deformation. However, the rate at which force-displacement work is done on or by the tablet during the different phases of compaction is affected by the interactions between the press deformation and the viscoelastic properties of the tablet. For example, during the dwell phase when punch

displacement is held constant, the rate at which the press can do work by continuing to compact the tablet depends on how fast internal viscoelastic flow can occur within the tablet. During the unloading phase, when the punches begin to move apart, the elastic recovery properties of the tablet again dictate how fast the tablet can do force-displacement work on the press. This fact is illustrated in Figure II.7, which shows that Avicel releases more energy and at a faster rate than Emcompress during the unloading phase. Therefore, the coupling of the tablet's viscoelastic properties with elastic press deformation dictates how fast energy is stored and released by the tablet press during the compaction cycle, as schematically represented in Figure II.8.



II.7 Lower punch incremental work versus time for Avicel (O/●) and Emcompress (□/■) (nonelastic curves, open symbols/elastic curves, closed symbols) compressed to a peak punch pressure of 135 MPa. The three phases of tablet compaction are marked as: loading (A-B), dwell (B-C), and unloading (C-D). Top dead center occurs at the time axis origin, and the arrows point to the beginning and end of the dwell phase.



II.8 A schematic representation of the coupling between press elasticity and tablet viscoelasticity: compression rollers (A), upper and lower punches (B and C), viscoelastic tablet element (D), and upper and lower compression roller assemblies (E and F).

## CONCLUSIONS

The deformation studies done with the cathetometer conclusively show that the Stokes B2 tablet press undergoes an elastic deformation, which can be characterized by two different elastic moduli (one for the upper and one for the lower compression roller assemblies); both elastic moduli are independent of compaction phase and lower punch penetration setting. The elastic moduli are summarized in Table II.3. The cathetometer data were independently verified by the lead compact studies (Figure II.3). Therefore, on the basis of these results, we recommend that, when calculating punch displacement for the Stokes B2, press deformation be accounted for by using the corrected displacement Equations 5a and 5b and the elastic constants in Table II.3.

The incremental work of compaction studies showed that press deformation absorbs energy during the loading phase and then releases this energy later in the compaction cycle. The rate at which the press stores and releases elastic energy depends in part upon the viscoelastic properties of the tablet. The coupling between the material properties of the tablet and press work together to change the punch-displacement profile, so that different tablet formulations, compression pressures, and operating conditions will lead to different compaction/punch-displacement profiles (cf. Figures II.6 and II.7). On the basis of these results, if a tablet press undergoes significant deformation during compaction, the coupling between the press and tablet should be accounted for when analyzing tablet compaction or trying to simulate the punch-displacement profile of that tablet press.

## ACKNOWLEDGMENTS

The authors wish to thank Russell Nesbitt and the Warner Lambert Co. for the generous donation of the Stokes B2 tablet machine, and the American Association of Colleges of Pharmacy and Eli Lilly and Co. for their generous financial support. The authors would also like to thank Thomas Kincaid for assistance with statistical analysis and David Weir of Stokes-Merril for information regarding the Stokes B2 tablet press.

## REFERENCES

- (1) Garratt, J. D., Survey of displacement transducers below 50 mm. *J. Phys. E: Sci. Instrum.*, 12, 563-573 (1979).
- (2) Rippie, E. G.; Danielson, D. W., Viscoelastic stress/strain behaviour of pharmaceutical tablets: analysis during unloading and postcompression periods. *J. Pharm. Sci.*, 70, 476-482 (1981).
- (3) Lammens, R. F.; Polderman, J.; deBlaey, C. J.; Armstrong, N. A., Evaluation of force-displacement measurements during powder compaction: Precision and accuracy of powder height and punch displacement measurements. *Int. J. Pharm. Technol. Prod. Manuf.*, 1, 26-35 (1980).
- (4) Lammens, R. F.; Polderman, J.; deBlaey, C. J., Evaluation of force-displacement measurements during powder compaction: Precision and accuracy of force measurements. *Int. J. Pharm. Technol. Prod. Manuf.*, 1, 26-35 (1979).
- (5) Juslin, M. J.; Paronen, T. P. On the accuracy of displacement measurements by instrumented single-punch machines. *J. Pharm. Pharmacol.*, 32, 796-798 (1980).
- (6) Kennerley, J. W.; Newton, J. M.; Stanley, P., Tablet thickness variation and machine stiffness. *Acta Pharm. Suecica*, 18, 106-107 (1981).
- (7) Walter, J. T.; Augsburger, L., A computerized force/displacement instrumented system for a rotary press. *Pharm. Technol.*, 10, (2), 26-34 (1986).
- (8) Muller, V. F.; Schierstedt, D. *Pharm. Ind.*, 44, 834-837 (1982).
- (9) Holman, L. E.; Marshall, K., Calibration of a Compaction Simulator for the Measurement of Tablet Thickness During Compression. *Pharm. Res.*, 10, 816-822 (1993).
- (10) Oates, R. J.; Mitchell, A. G., Calculation of punch displacement and work of powder compaction on a rotary tablet press. *J. Pharm. Pharmacol.*, 41, 517-523 (1989).
- (11) Hoblitzell, J. R.; Rhodes, C. T., Determination of a relationship between force-displacement and force-time compression curves. *Drug Dev. Ind. Pharm.*, 16, 201-229 (1990).



- (12) Devore, J.; Peck, R. *Statistics, the Exploration and Analysis of Data*; West Publishing: St. Paul, 474-477 (1986).
- (13) Hoag, S. W.; Rippie, E. G., Thermodynamic Analysis of Energy Dissipation by Pharmaceutical Tablets During Stress Unloading. *J. Pharm. Sci.*, 83, 903-908 (1994).
- (14) Ho, A.; Barker, J. F.; Spence, J.; Jones, T. M., A comparison of three methods of mounting a linear variable displacement transducer on an instrumented tablet machine. *J. Pharm. Pharmacol.*, 31, 471-472 (1979).
- (15) Morehead, W. T.; Rippie, E. G., Timing Relationships among Maxima of Punch and Die-wall Stress and Punch Displacement during Compaction of Viscoelastic Solids. *J. Pharm. Sci.*, 79, 1020-1022 (1990).

### CHAPTER III

#### FORCE TRANSDUCER DESIGN FOR DIE WALL STRESS MEASUREMENT DURING TABLET COMPACTION: OPTIMIZATION AND VALIDATION OF SPLIT-WEB DIE USING FINITE ELEMENT ANALYSIS

## ABSTRACT

Radial stress measurements during tablet compaction are important for the understanding of die wall friction, capping, lamination and the three-dimensional viscoelastic characterization of tablets. One transducer for the measurement of die wall stress is the three-layered die developed by Rippie and Danielson; however, to accommodate mounting, the die table must be modified. To overcome this problem the authors developed a split-web die concept which encloses the sensing web in a cylinder. A design-by-analysis approach and finite element analysis (FEA) software were used to determine optimal strain gage placement and web dimensions. To calculate the stress/strain distribution in the die wall needed for the design-by-analysis approach, the commercial finite element program COSMOS/M was employed. Calculations were performed with a 2-dimensional 4-node linear plane finite element model. Based on FEA results, a 1/8 in. sensing web with a strain gage located at  $\phi = 0^\circ$  was selected for experimental testing. A linear calibration curve ( $r^2=0.999$ ) with no hysteresis was obtained, verifying the FEA predictions. Residual die wall stress (RDWS) and radial versus axial stress transmission curves were generated for commonly used excipients. The results were in excellent agreement with the published data, also demonstrating the effectiveness of the split-web die designed using the design-by-analysis approach.

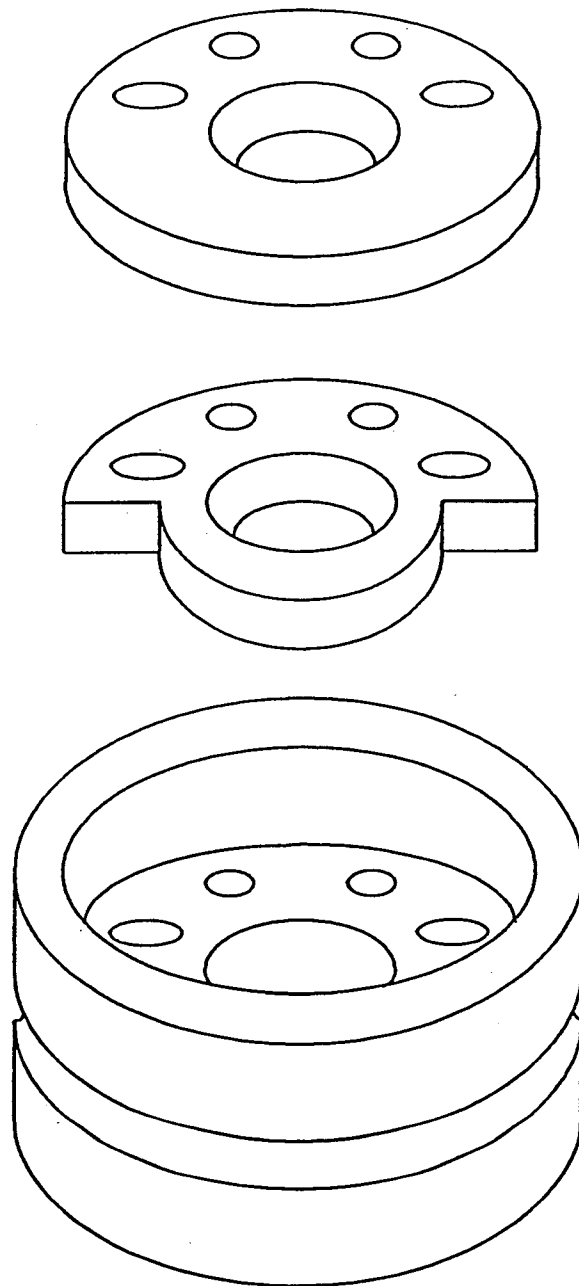
## INTRODUCTION

The three-dimensional analysis and modeling of tablet compaction requires accurate measurements of radial die-wall stress (DWS) during compaction. At present there are many transducer systems available that can measure die wall stress (1-7). The earliest transducer design for the measurement of DWS is Nelson's three-punch die (1), which was followed by, to name a few, Windheuser's segmented die (2), and Ridgway's photoelastic die (3). Of all the early designs, the segmented die has become the most popular. When designing a transducer, two major concerns are the effects of tablet height and tablet position within the die on output signal (8). These factors make calibration and data interpretation more difficult because they interact, causing the transducer to have a non-linear output signal (8). To address these concerns, the segmented die design has been modified over time to achieve better signal output. For example, Hölzer and Sjögren (9) found that the die wall signal increases linearly with tablet height; to compensate, they used the area of contact between tablet and die wall to normalize the output signal. Huckle and Summers (10) improved DWS measurement by averaging the output signal from multiple gages placed on the cut-away portion of the die. This strain gage arrangement reduces the dependence of DWS measurements on tablet height and position. Cocolas and Lordi (11) developed another approach which used the height of the tablet to normalize the summed response from four piezoelectric force transducers placed in a spiral arrangement around the die bore. All of these methods greatly improved the original segmented die design; however, measurements from these systems are based upon averaging DWS over the height of the tablet, which neglects changes in DWS that can occur along the height of the

tablet during compaction. In addition, transducer calibration can be affected by the fact that the complicated stress/strain distribution within the transducer die wall depends upon tablet height and position within the die.

Another approach for improving DWS measurement is the three-layered die developed by Rippie and Danielson (6). By integrating a sensing web into a thin middle layer, this design isolates stress measurement to the narrow band around the tablet. In addition, the stress/strain distribution in the sensing web is completely uncoupled from all other die wall stresses and strains. The advantage of Rippie's system over other systems is that the stress is measured over a very small area, which gives a much closer approximation to the true stress. Also, by isolating stress measurement to a narrow band around the tablet DWS measurement is independent of tablet height and position within the die (as long as the sensing web has full contact with the tablet). Thus changes in DWS with tablet height can be accounted for. Another advantage of Rippie's three layered die is signal linearity. Because the strain gage is mounted on a thin sensing web which is uncoupled from other die wall stresses and strains, and where the stress underneath the web is approximately constant, as predicted by Lamé's solution (12) for the stress/strain distribution in a hollow cylinder, the tangential strain on the outer die surface is a linear function of a uniformly applied internal pressure. Even though the sensing web in the three layered die is not completely symmetric this linear relationship still holds (recall Saint-Venant's principle (12)).

However, a disadvantage of Rippie's design is that the die table must be modified to accommodate mounting of the transducer. The die hole must be enlarged to accommodate the vertical die lockscrews that hold the transducer in place because the standard horizontal die lockscrew causes the layers to tilt, which binds the sensing web.

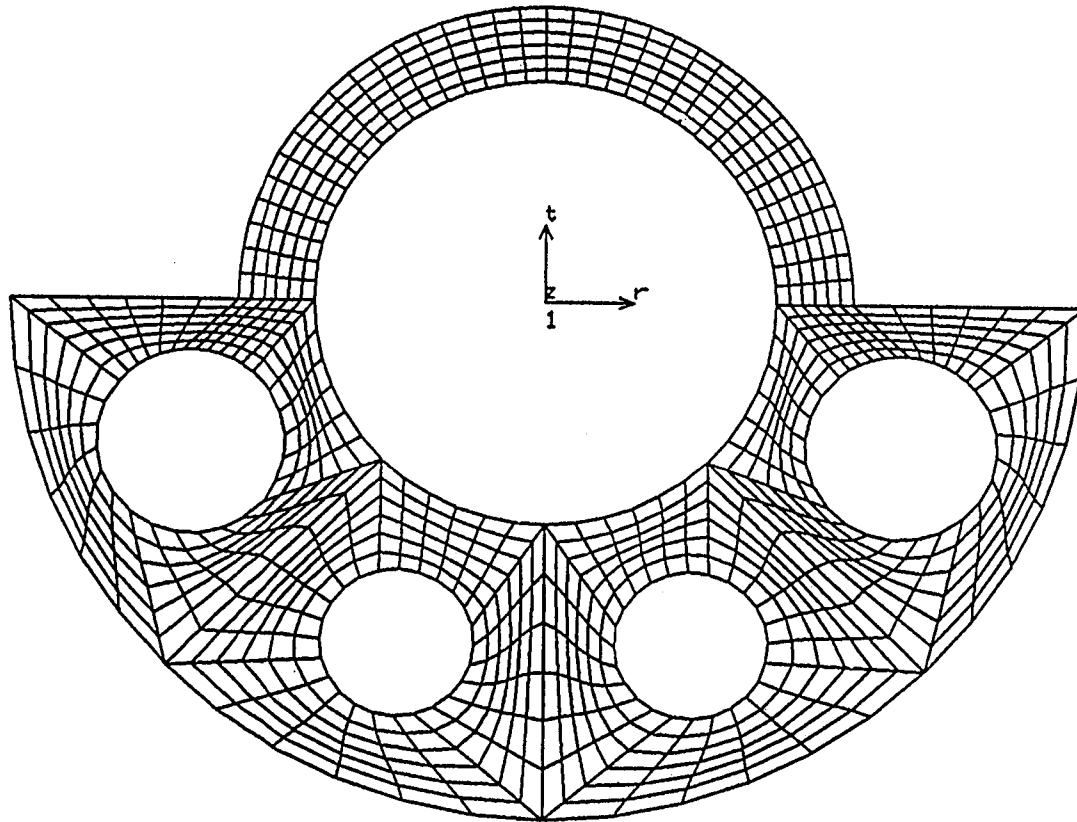


III.1 Assembly of the three layer split web die design.

To avoid modifying the die table, the authors propose a split-web die concept which encloses the sensing web in a cylinder, thereby avoiding the sensing web binding caused by the standard die lockscrew (see Figure III.1). To obtain the best design, the sensing web configuration must be optimized. The primary design variables to be optimized are the sensing web thickness and the strain gage position on the sensing web. Therefore, the goal of this paper is to use the optimal design process (ODP) developed earlier by the authors (8) to determine the sensing web dimensions and strain gage arrangement that optimizes signal output. Finite element analysis (FEA) is used as a numerical tool for systematic optimization of the split-web die design. To confirm the effectiveness and signal linearity of the transducer designed by the ODP, pressure cycle curves (i.e. radial versus axial transmission curves) and residual die-wall stress measurements for some commonly used excipients will be generated and compared with literature data.

## THEORY

The finite element analysis is a numerical method for approximating the governing equations (stress/strain fields) of any continuous body. The first step in FEA is to generate a finite element model, which is a geometric representation of the actual mechanical component being analyzed. This model is created by dividing the actual component into a large number of subdivisions called, "finite elements." These elements are interconnected at specified points called, "nodes," or "nodal points." The nodes lie on the element boundaries and are the points where adjacent elements are connected. To create a finite element mesh of a mechanical component, the user needs to enter the geometric dimensions of the component into the FEA software (e.g.



III.2 Finite Element Model for the 1/8 in. sensing web.



thickness, shape, etc.). Once the geometric model has been created, the material properties, boundary conditions and loading conditions are then used to calculate the stress/strain fields (13).

Figure III.2 shows the finite element model created for stress/strain analysis of the sensing web. The computations were performed with the finite element software, COSMOS/M, running on a personal computer. The model uses a total of 630 PLAND2D 4-node, iso-parametric elements (14), interconnected at 732 nodal points. Since the web thickness is small in comparison to the other dimensions and no axial loads are applied, the assumption of plane stress was employed. All the nodal points along the alignment pin holes were restricted in translation but free in rotation. These boundary conditions were used to simulate the behavior of the actual web. For the same reasons given by the authors' previously (8) the die-wall friction that would induce axial forces was neglected for the FEA calculations.

## EXPERIMENTAL

Based upon dimensions obtained from the ODP, the die was built in three sections (Figure III.1). To test the FEA predictions, two different prototypes of the sensing web were built with sensing web thickness of 1/8 inch (3.175 mm) and 1/16 inch (1.5875 mm). Both prototypes had a web height of 1/8 inch (Figure III.3). To allow free movement between the web and adjacent layers, the sensing web was made 1/10,000 in. thinner than the rest of the middle section. This slight clearance improves accuracy of die wall stress measurements because the interfering friction forces are reduced, allowing the web to move freely between layers. Also, the clearance is small enough to prevent tableting material from extruding between adjacent layers. The die was calibrated in triplicate with Neoprene rubber plugs and an instrumented punch.

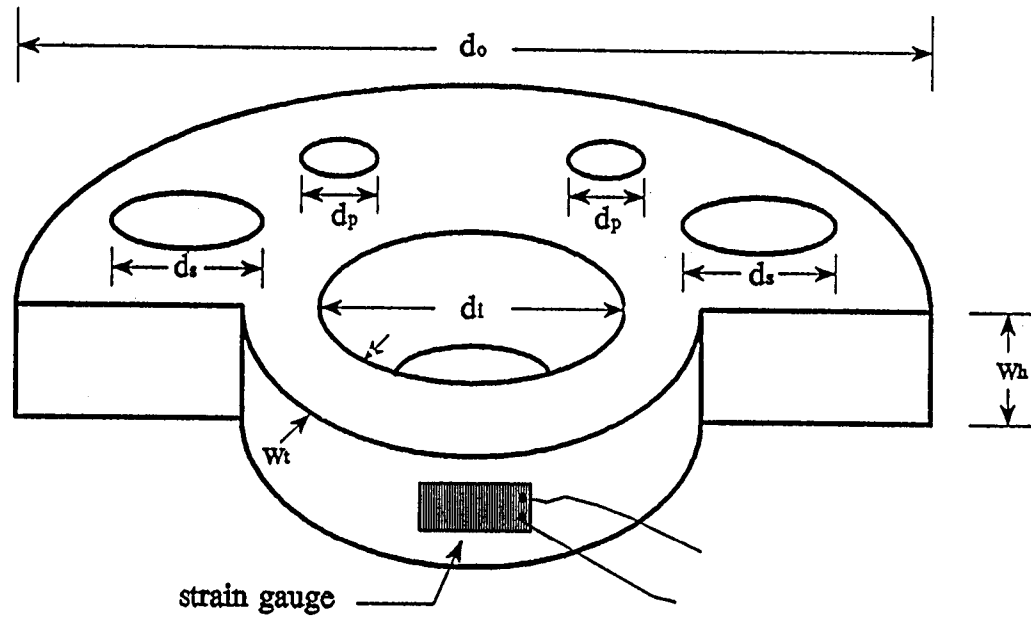
The pressure was applied by filling the die with the rubber plugs and manually rotating the turret through the loading, dwell and unloading phases.

### Press Instrumentation

A Stokes B2 rotary tablet press (F.J. Stokes Machine Company, Philadelphia, PA) equipped with "standard IPT head" 3/8 in. flat faced punches was used for tablet compaction. The ejection cam was removed to allow for residual die wall stress measurement. Lower punch stress was measured with an instrumented compression roller pin (Specialty Measurements Int., Pittstown, NJ). A bonded electrical resistant strain gage (EA-06-031DE-120, Micro-Measurements, Raleigh, NC) was placed on the sensing web at  $\phi = 0^\circ$  and configured into a single arm Wheatstone bridge. The turret angular velocity ( $\omega$ ) and the time at which top dead center occurred were determined by a magnetically triggered digital proximity switch and aligned magnets placed on the turret. The signals from the instrumented die, roller pin and proximity sensor were sent to a personal computer interfaced with a 12-bit 100 kHz analog to digital (A/D) converter (model AT-MIO-16, National Instruments Corp., Austin, TX).

### Tablet Compaction

Compressible sugar (Dipac, Mallinckrodt AR, Paris, KY), microcrystalline cellulose (Avicel PH-101, FMC Corp., Philadelphia, PA), starch (Sta-Rx 1500, Colorcon, Westpoint, PA), sodium chloride (Mallinckrodt AR, Paris, KY) and acetaminophen (Sigma Chemical, St. Louis, MO), were used for the compaction studies. For lubrication, a 20% slurry of magnesium stearate in isopropyl alcohol was swabbed onto the die wall and dried before compaction. The die was hand-filled and the tablets were compressed with an average turret angular velocity of  $\omega = 4.62$  rads/sec. Three tablets of each material were compacted to a peak



- |       |                               |                   |
|-------|-------------------------------|-------------------|
| $d_i$ | : inner diameter              | = $3/8''$         |
| $d_o$ | : outer diameter              | = $7/8''$         |
| $d_s$ | : screw hole diameter         | = $5/32''$        |
| $d_p$ | : alignment pin hole diameter | = $1/8''$         |
| $w_h$ | : web height                  | = $1/8''$         |
| $w_t$ | : web thickness               | = $1/16'', 1/8''$ |

### III.3 Dimensions of sensing web for the split web die.

die-wall pressures of 30, 60, and 90 MPa. To maintain compression roller alignment, the upper compression roller eccentric cam and the eye-bolt position were fixed; thus, the desired compaction pressure was achieved by varying the fill weight.

## RESULTS AND DISCUSSION

### Design Optimization

Having developed the split-web design concept, the next step is to optimize web thickness and strain gage position according to ODP algorithm (see Figure B.1, Reference 8). It should be noted, that as long as the cutting angle is large enough so as not to affect the tangential strain on the outer die wall surface the cutting angle isn't important; thus, for the split-web design the cutting angle does not require optimization.

### Web Thickness

As discussed in the authors' previous paper (8), the sensing web thickness is an important factor in determining optimum signal output. As sensing web thickness decreases, the signal output increases, but at the same time, the decreasing web thickness also weakens the web. Because web thickness can only be reduced to a certain point before material failure occurs, the web thickness must be chosen in a manner which optimizes output-signal level while not failing when the in-service loads are applied.

To determine the minimal web thickness that will not fail at peak compression, the Von Mises failure criteria was used (8). The Von Mises failure criteria predicts that material failure will occur when the Von Mises stress ( $\sigma_{vm}$ ) exceeds the uniaxial yield

strength ( $\sigma_{yd}$ ) of a material; thus, the criteria for material failure can be written as:

$$\sigma_{yd} \leq \sigma_{vm} \quad (1)$$

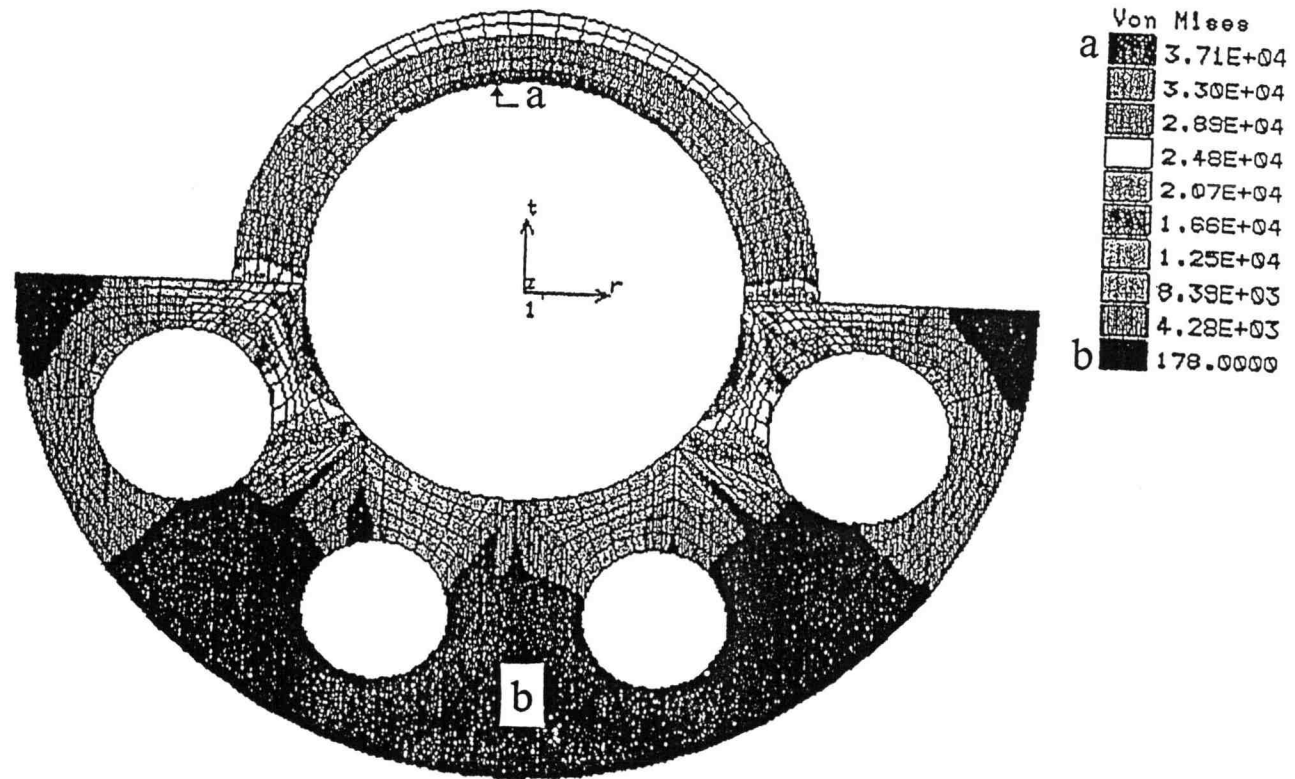
Using a uniform inner die wall pressure of 120 MPa to simulate peak loading conditions, the Von Mises stress distribution was calculated for the finite element model shown in Figure III.2. The greatest Von Mises stress occurs at the sensing web arch (point a, Figure III.4), while the lowest Von Mises stress occurs in the area around the alignment-pin holes (point b, Figure III.4). It should be noted that even though there are two corners at the base of the sensing-web arch where the concentration of stress could affect structural integrity, the Von Mises stress in these regions is still well below the maximum global Von Mises stress on the sensing web arch. Thus, Von Mises stress around the two corners are not important in the analysis of material failure for this system. In addition, when a prototype is actually made these corners are usually rounded which further lowers the Von Mises stress making the possibility of material failure in these regions improbable. The maximum Von Mises stress (i.e. point a, Figure III.4) for the 1/16 and 1/8 in. sensing web prototypes and the literature values for the material yield strength of a typical D3 tool steel are summarized in Table III.1. As expected, the Von Mises stress decreases as the die wall thickness increases. Because the Von Mises stress in the 1/16 in. sensing web exceeds the material yield strength, the Von Mises failure criteria (Equation. 1) predicts that failure will occur in the 1/16 in. web but not in the 1/8 in. web. To test these predictions, tablets were compacted using the 1/16 and 1/8 in. webs. When the 1/16 in. sensing web was tested at an inner die wall pressure of 120 MPa, the sensing web failed, while the 1/8 in. sensing web was used many times at this pressure without failing. Thus, confirming the accuracy of FEA predictions.

To determine if the strain at the gage site is sufficient to produce a measurable signal, the tangential strain ( $\epsilon_t$ ) on the outer surface of the sensing web must be calculated and compared to the minimum detection limit of the strain gage and data acquisition system. Using the finite element model (Figure III.2), the tangential strain for the 1/16 and 1/8 in. sensing web prototypes were calculated from the node displacement. An exaggerated view of the deformed sensing web with an inner die wall pressure of 120 MPa is shown in Figure III.5. As expected the greatest node displacement occurs at the sensing web arch. Note the actual displacement of the sensing web arch is less than 1/10,000th of an inch, alleviating concerns that die wall deformation could produce out of shape tablets.

Using the node displacement (Figure III.6), the tangential strains ( $\epsilon_t$ ) can be plotted versus angle ( $\phi$ ) along the mounting surfaces of sensing web ( $0^\circ$  to  $90^\circ$ , see Figure III.6). The  $\epsilon_t$  for the 1/16 and 1/8 in. webs varies from 810 to 1091  $\mu\epsilon$  and from 389 to 508  $\mu\epsilon$ , respectively. FEA results indicate that the tangential strain, on the average, doubles when the sensing web thickness decreases from 1/8 to 1/16 in.. Ideally, the full scale strain should be 1000  $\mu\epsilon$  or greater, but a peak strain of 389  $\mu\epsilon$  still produces a detectable signal. Therefore, based on an analysis of material failure and signal output, the authors recommend a web thickness of 1/8 in.. In addition, the 1/8 in. web has a built in safety factor ( $SF$ ) of approximately 15% (8).

### Strain Gage Location

Strain gage position on the sensing web is also a critical design factor, because a strain gage that is placed in an area of high stress concentration (high strain gradient) may produce inaccurate results. Because strain gages average the strain over the area covered by the grid, improper averaging of strain may occur in areas with steep strain

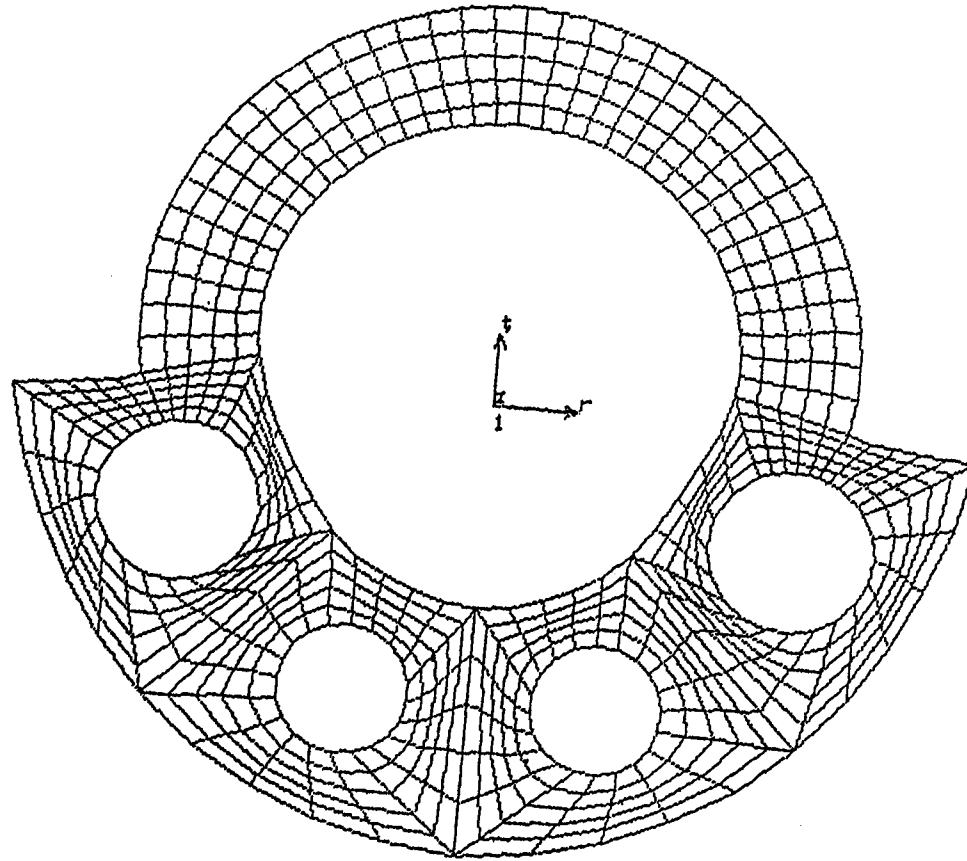


III.4 Von Mises stress contour for the 1/16 in. prototype sensing web at maximum inner die wall pressure of 120 MPa.

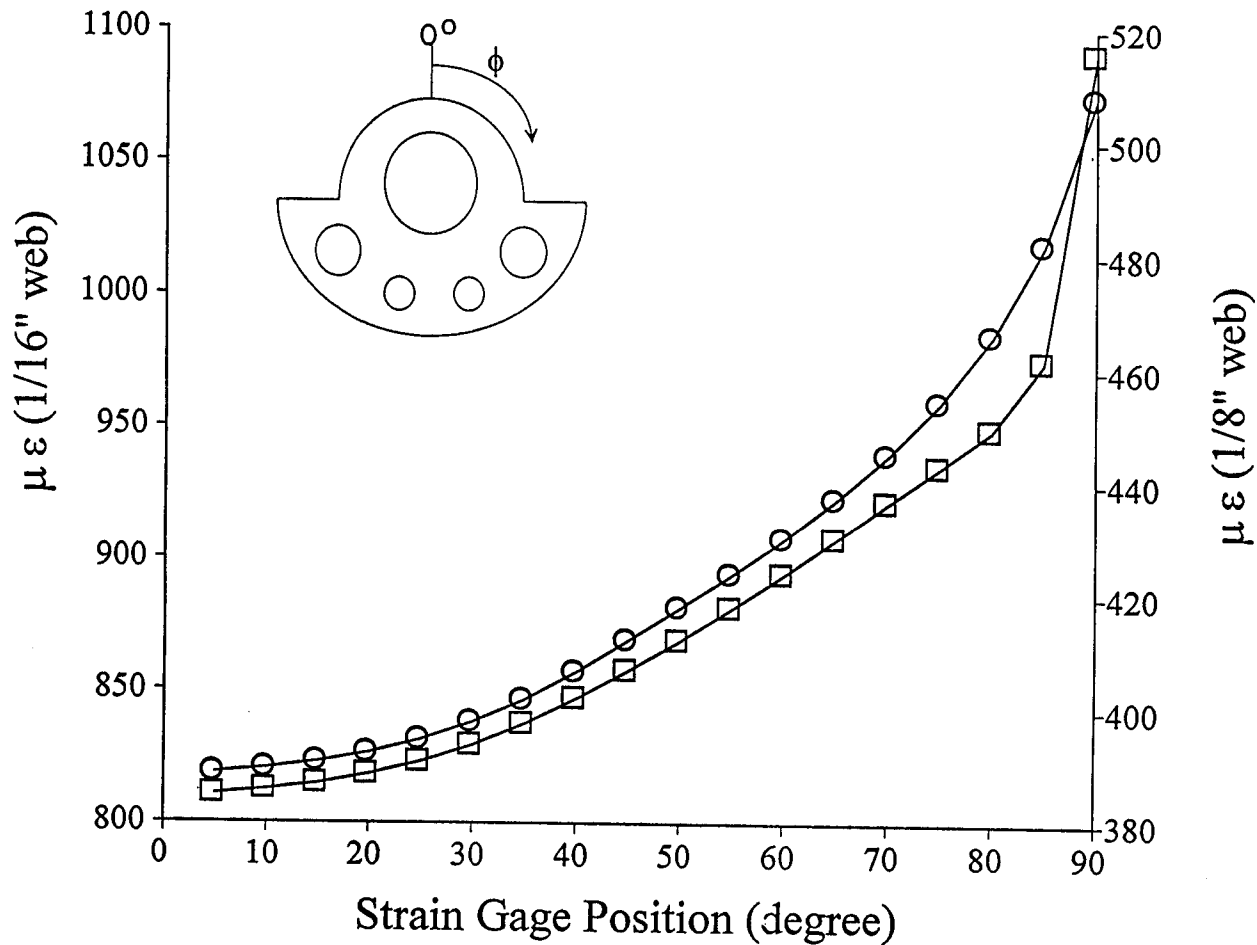
Table III.1 Summary of Maximum Von Mises Stresses for 1/16 and 1/8 inch Webs.

Web Designs	Material Yield Stress (psi) - D3 Tool Steel	Maximum Von Mises Stress (psi)
1/16 inch Web	$6.4 \times 10^4$	$7.42 \times 10^4$
1/8 inch Web	$6.4 \times 10^4$	$4.96 \times 10^4$





III.5 A deformed 1/8 in. sensing web showing maximum nodes displacement at the arch of the sensing web.



III.6 Effect of web thickness on tangential strain for the 1/8 (○) and 1/16 (□) in. sensing webs. The sensing web drawn within the figure shows the position of the zero degree angle mark.

gradients. Figure III.6 shows a relationship between die wall strain and strain gage position on the sensing web. The strain gradient (slope of strain vs.  $\phi$ ) is smallest at  $\phi = 0^\circ$ , and highest at  $\phi = 90^\circ$  (i.e. around the edges of sensing web). Even though stress concentration in the web could be used to produce a higher output signal (i.e. by placing the strain gage in an area of high concentration such as  $\phi = 90^\circ$ ), this is not a recommended method of improving signal output. Therefore, the authors recommend placing a single strain gage at  $\phi = 0^\circ$  or placing two strain gages at  $\phi = \pm 30^\circ$ .

#### Signal Linearity

To theoretically verify output signal linearity, a strain calibration curve was calculated for strain gages on the 1/8 in. sensing web positioned at  $\phi = 0^\circ, 30^\circ$  and  $60^\circ$ , with the inner die wall pressures ( $P_1$ ) used for calculation, ranging from 0 to 120 MPa. A linear relationship is observed for all the three strain gage positions (Figure III.7). The difference in  $\epsilon_t$  for strain gages positioned at  $0^\circ, 30^\circ$  and  $60^\circ$  is less than 12%.

#### Die Calibration

The experimental calibration curve for the 1/8 in. split-web die is shown in Figure III.8. Even though the height of the tablet changed during calibration, a 99.9% correlation was still obtained. At a pressure of 90 MPa the bridge output with a strain level of 0.28 mV/V is produced. This linear calibration curve confirms the FEA prediction of linearity. Note that with this method of calibration, the application of pressure causes the height of the tablet to change. For the punch penetration setting used in the study, the height of the rubber plugs varied from an almost full die to 3/8 in.. The linear signal illustrates an advantage of layered dies over other methods of DWS measurement. In addition to linearity, the hysteresis phenomenon can be used to

judge transducer performance. Hysteresis is defined as a deviation from linearity in which the unloading curve falls below the loading curve (15), and when seen, indicates material or strain gage yielding. When signal output from the instrumented die was measured for both loading and unloading, no hysteresis was observed (Figure III.8, inset), thereby substantiating both Von Mises strength and the signal output calculations. Lack of hysteresis also indicates that the neoprene used for calibration doesn't affect the calibration results (10).

### Evaluation of Optimized Design

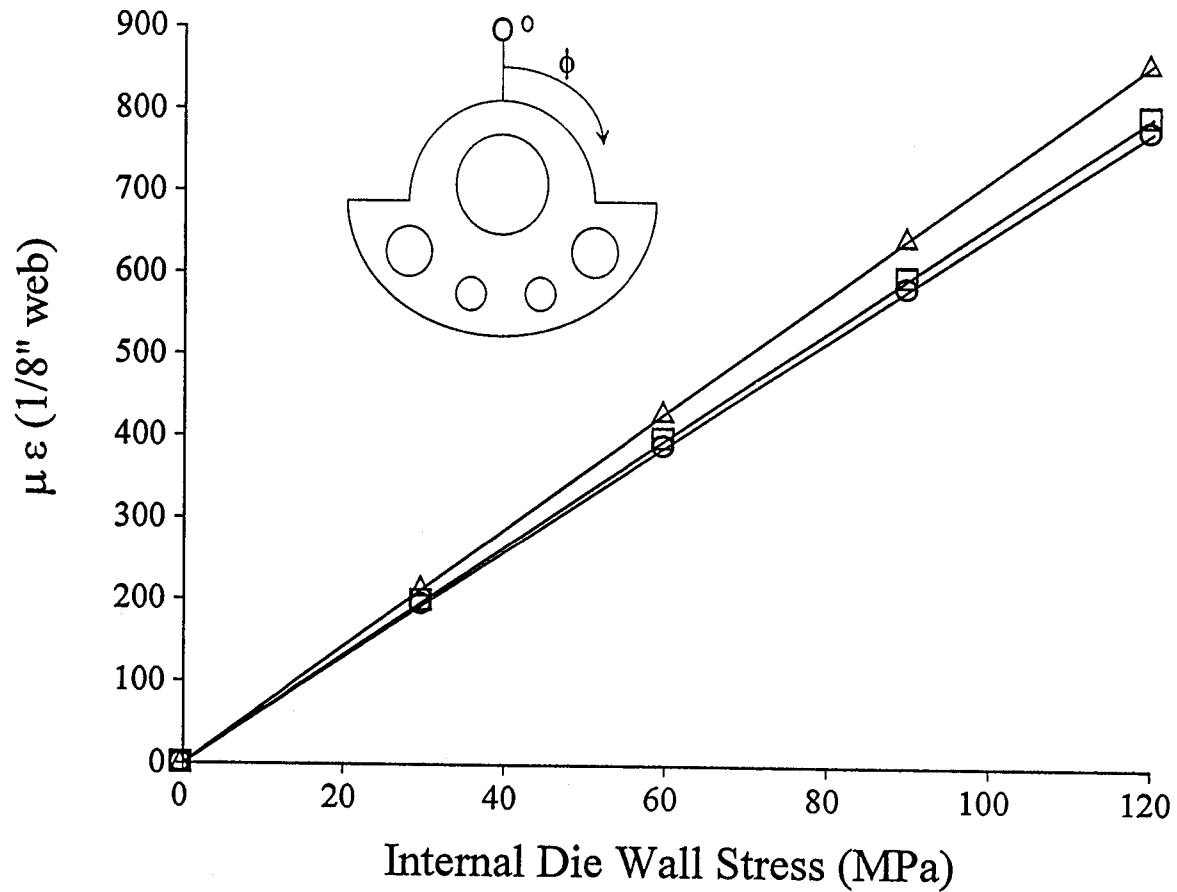
To test the performance of the transducer designed by using ODP, the compaction characteristics of some well characterized excipients were studied using radial versus axial stress transmission curves (pressure-cycle curves) and residual die wall stress (RDWS) measurements.

### Pressure cycle curves

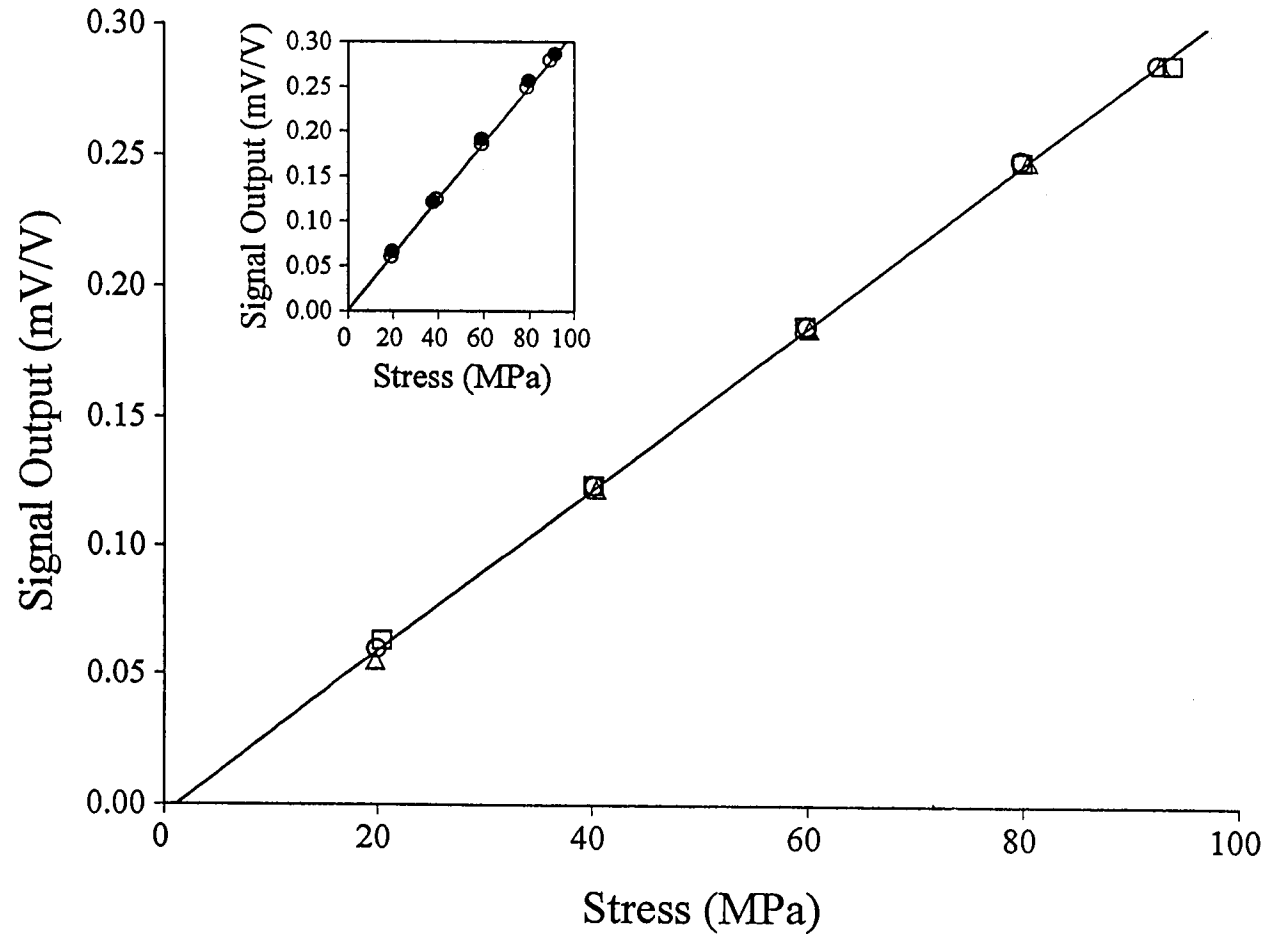
Radial to axial stress transmission curves (pressure-cycle curves) were first used by Long (16) to evaluate the compaction characteristics of materials used in powder metallurgy. Since then, pressure-cycle curves have been used to characterize pharmaceutical materials. By determining the initial and post-yield slope and Poisson's ratio from the pressure-cycle curves, the type of deformation a material undergoes during compaction can be characterized. For this study, Poisson's ratio was calculated using (17):

$$\sigma_r = \sigma_a \cdot \nu / (1 - \nu) \quad (2)$$

where  $\sigma_r$  = radial stress,  $\sigma_a$  = axial stress (Mpa),  $\nu$  = Poisson's ratio of the material; the model parameters were determined using standard linear regression techniques. Even



III.7 Effect of strain gage position  $\phi = 0^\circ(\circ)$ ,  $30^\circ(\square)$  and  $60^\circ(\Delta)$  on tangential strain at inner die wall pressures ranging from 0 to 120 MPa. The sensing web drawn within the figure shows the position of the zero degree angle mark.



III.8 Experimental calibration curve for the split web die using Neoprene rubber plugs. Each symbol set represents an individual run or replicate. The inset shows loading (○) and unloading (●) curves falling closely onto the regression line.

though Equation 2 is not a universally accepted method for calculating the Poisson's ratio of a compact during compaction, it can still be used to compare data collected by our transducer with other transducers designed for DWS measurement (i.e. it is not our goal to validate Equation 2 or its use in data interpretation but to validate the transducer design).

These results are in general agreement with the literature (18-20), which validates the transducer design. Based on the initial slope (before yield) and the post-yield slope value which is less than one in all cases, the materials were shown to exhibit behavior more closely to that of a Mohr body (Table III.2). Figures III.9 and III.10 show representative pressure-cycle curves for sodium chloride (NaCl) and starch 1500, respectively. However, the results for starch and NaCl are in disagreement with Cocolas and Lordi (11). This discrepancy may be attributed to the material form, i.e., granular or crystalline (18), particle shape and crystal habit (19) and moisture content (20). Despite some differences, there is general agreement with the literature (17-19), which validates the transducer design. Also, it is interesting to note that the slope of the pressure-cycle curve for starch shifts downward when the die wall was not lubricated prior to tablet compaction, indicating that differences in formulation characteristics can also be observed with the split-web die.

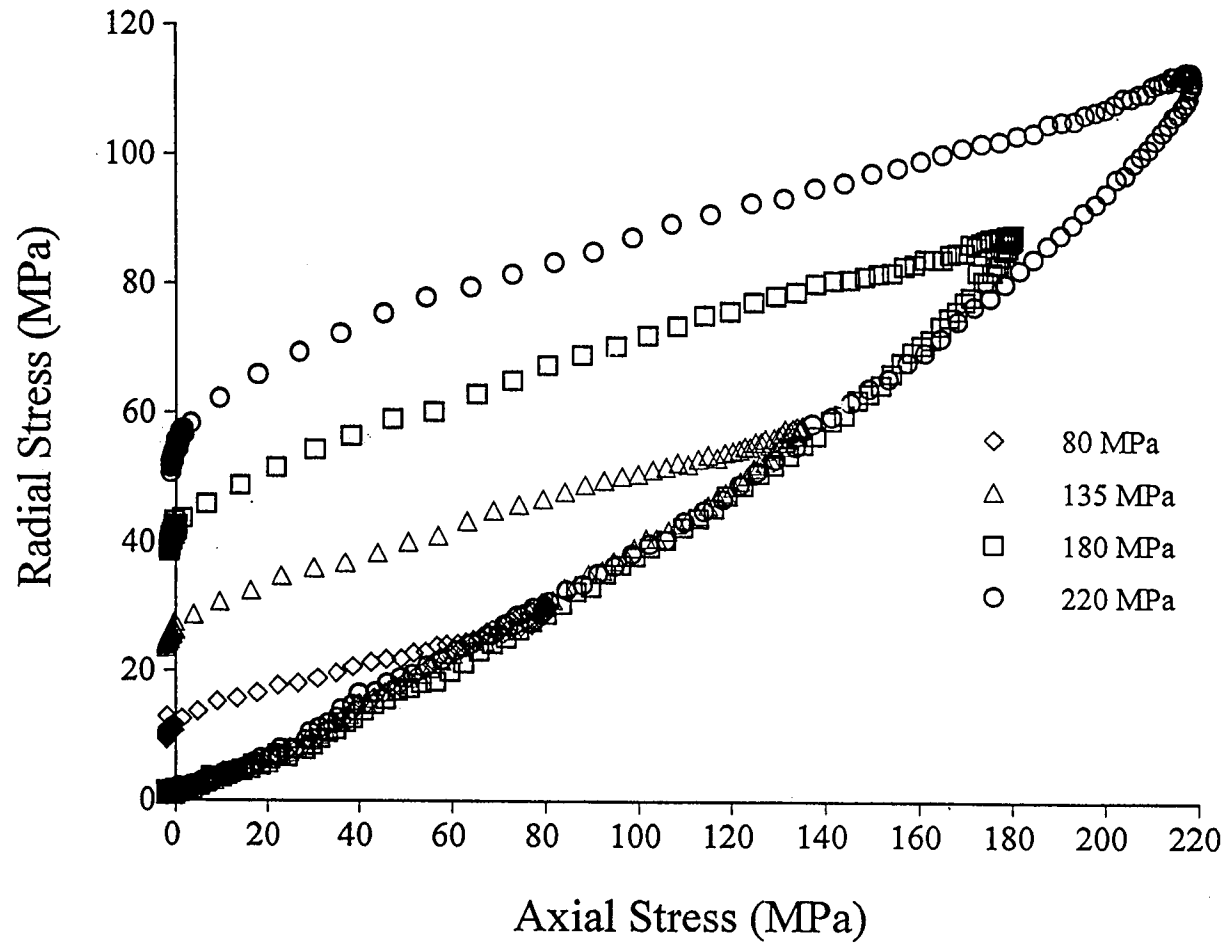
#### Residual die wall stress (RDWS)

Since the exact determination of the yield point can be very difficult due to ill defined breaks (see Figures III.9 and III.10) in the pressure-cycle curves, use of pressure-cycle curves may lead to ambiguous conclusions about the properties of a material. This is evident from the literature where a material (e.g. NaCl) has been characterized in two different classes. Thus, a better indication of material characteristics is obtained

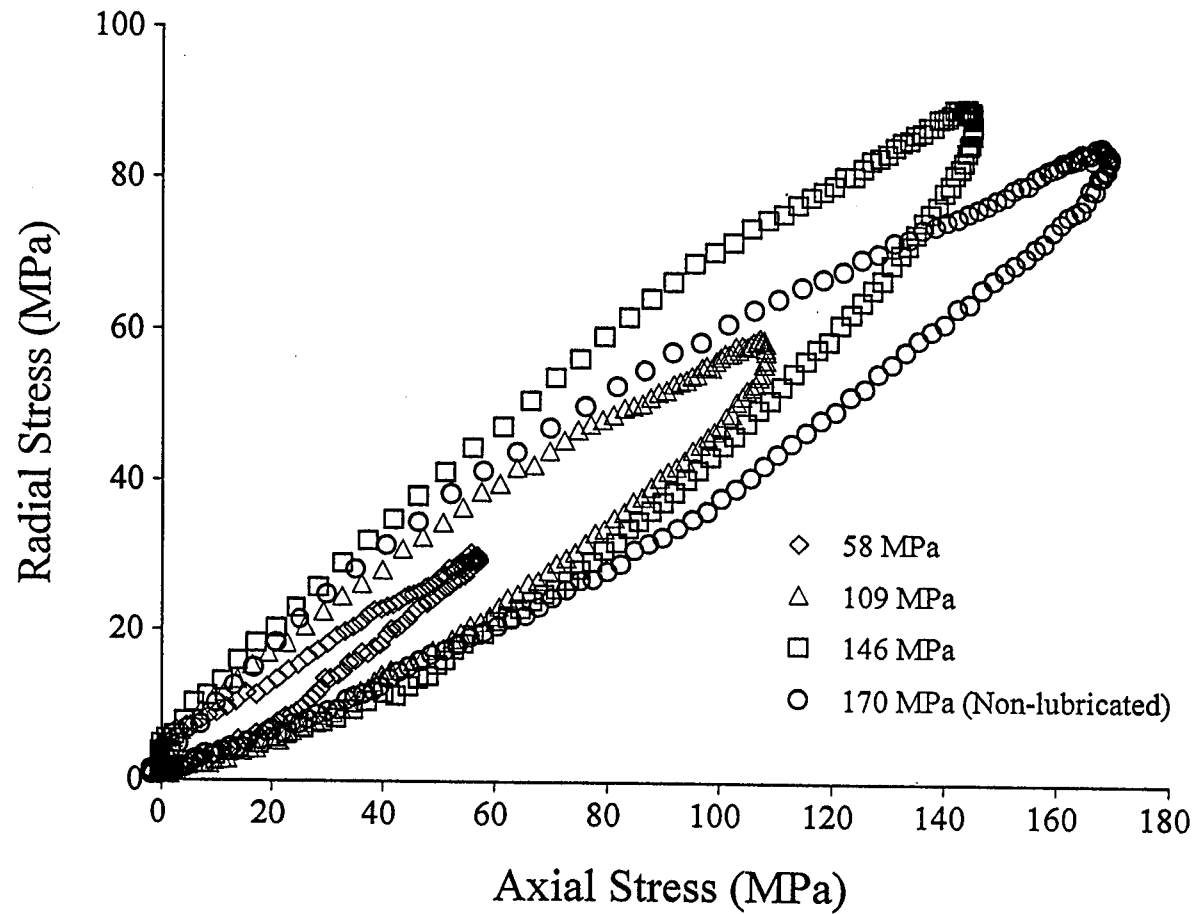
Table III.2 Initial and Terminal Slopes and Poisson's Ratio Calculated from Pressure-Cycle Curves.

Material	Initial Slope	Terminal Slope	Poisson's Ratio
APAP	0.36	0.45	0.27
Avicel PH-101	0.24	0.74	0.19
Dipac	0.35	0.51	0.26
Sodium chloride	0.25	0.56	0.20
Starch 1500	0.26	0.78	0.21



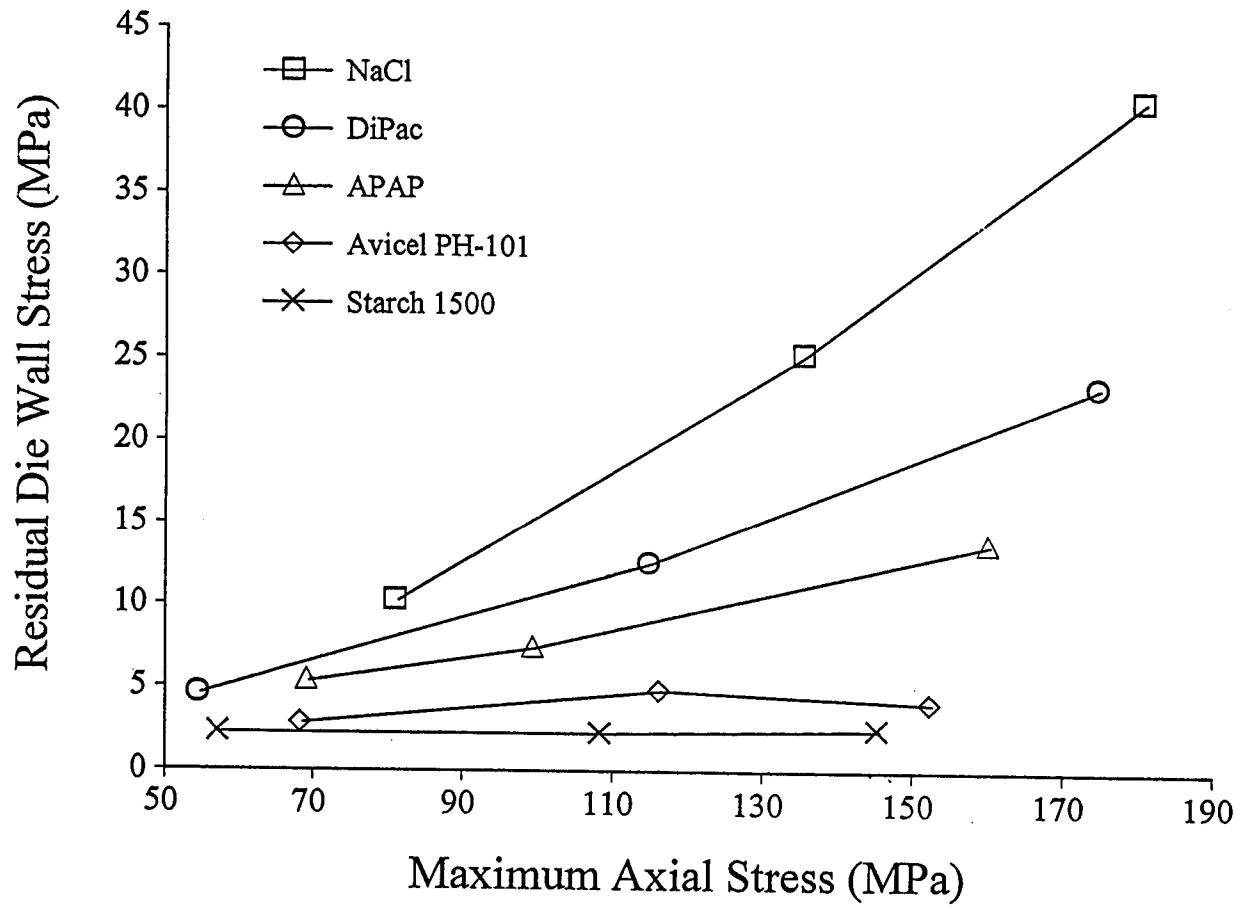


III.9 Radial versus axial stress transmission curves for sodium chloride using 1/8 in. sensing web. Legend indicates peak axial pressures.



III.10 Radial versus axial stress transmission curves for Starch 1500 using 1/8 in. sensing web. Legend indicates peak axial pressures.

from residual die wall stress (RDWS) measurements because they relate directly to the irreversible deformation undergone during compaction (21). The RDWS versus maximum applied stress is plotted in Figure III.11 for the excipients used in this study. NaCl, DiPac (compressible sugar) and acetaminophen (APAP) possess the highest RDWS of the excipients studied and they exhibit the greatest effect of increasing pressure, resulting in higher RDWS, indicating plastic behavior. For sodium chloride, the RDWS increases linearly with the increase in applied pressure. The increase in residual die wall stress associated with each increment of pressure was also observed by Shotton and Obiorah (19). Starch doesn't show any significant effect of pressure on RDWS, indicating the high elastic recovery characteristics of this material. The RDWS for Avicel PH-101 increases linearly with pressure, but levels off at about 120 MPa applied stress, as observed by Krycer et al. (21). In the case of starch, an increase in pressure did not effect RDWS.



III.11 Residual die wall stress versus maximum axial stress using 1/8 in. sensing web for the excipients studied.

## CONCLUSIONS

The split-web die concept developed by the authors, encloses the sensing web in a cylinder, thereby allowing the instrumented die to be mounted without modification of the die table. This design overcomes a significant problem with three-layered die transducer and thus improves DWS measurement. The optimal web thickness and strain gage position were determined using the optimal design process (ODP) transducer. The output signal for this design is linear ( $r^2 = 0.999$ ) and independent of tablet height. Based upon FEA, the authors recommend the use of the 1/8 in. sensing web and a strain gage positioned at  $\phi = 0^\circ$ , or two gages at  $\phi = \pm 30^\circ$ , for optimal signal output. This system showed no hysteresis, which indicates that there is no permanent distortion of the 1/8 in. sensing web in the range of pressures studied.

Residual die wall stress and pressure-cycle curves were used to analyze the compaction characteristics of some of the commonly used excipients. The split web die design has the ability to detect material as well as formulation differences which is important to the understanding of tablet compaction. The study has shown that FEA can accurately predict the performance of a transducer design, thus proving FEA to be a powerful tool for structural design optimization.

In summary, the optimal design process (ODP) and FEA employed in this and the previous paper (8) for the design of press instrumentation has not been reported in the pharmaceutical literature previously. Because this method can produce efficient transducer designs with less cost and time, the authors believe that this method represents a significant advancement over the existing trial-and-error method of transducer design.

## ACKNOWLEDGMENTS

The authors wish to thank Eli Lilly and Company and the American Association of Colleges of Pharmacy (AACCP) Young Investigator Program for their generous financial support.

## REFERENCES

- (1) Nelson, E., The physics of tablet compression VIII - Some preliminary measurements of die wall pressure during tablet compression. *J. Am. Pharm. Assn. Sci. Ed.* 44(8):494-497 (1955).
- (2) Windheuser, J., Misra, J., Eriksen, S. T., Higuchi. Physics of tablet compression XIII - Development of die-wall pressure during compression of various materials. *J. Am. Pharm. Assn. Sci.* 52(8):767-768 (1963).
- (3) Ridgway, K. and Rosser, P. H., The application of photoelastic techniques to a rotary tableting machine. *J. Pharm. Pharmacol.* 23:202S-209S (1971).
- (4) Conte, U., Colombo, P., La Manna, A., and Caramella, C., La mesure de la force radiale a l'aide d'une matrice divisee: Applications aux problemes pharmaceutiques. *Il Farmaco - Ed. Pr.* 32(11):551-559 (1977).
- (5) Kanaya, Y., Ando, T., and Asahina, K., A technique for measurements of die wall pressure during tablet compression. *Yakuzaigaku.* 39(1):26-33 (1979).
- (6) Rippie, E. G., and Danielson, D. W., Viscoelastic stress/strain behavior of pharmaceutical tablets: Analysis during unloading and postcompression periods *J. Pharm. Sci.* 70(5):476-482 (1981).
- (7) Amidon, G. E., Smith, D. P., Hiestand, E. N., Rotary press utilizing a flexible die wall. *J. Pharm. Sci.* 70(6):613-617 (1981).
- (8) Yeh, C. T., Altaf, S. A., and Hoag, S. W., Force transducer design for die wall stress measurement during tablet compaction. I: General theory of design optimization using traditional stress analysis and finite element analysis. *Pharm. Res.* Submitted with part II (January, 1996).
- (9) Hölzer, A. W. and Sjögren, J., Instrumentation and calibration of a single punch press for measuring the radial force during tableting. *Int. J. Pharm.* 3:221-230 (1979).
- (10) Huckle, P. D. and Summers, M. P., The use of strain guages for radial stress measurement during tableting. *J. Pharm. Pharmacol.* 37:722-725 (1985).
- (11) Cocolas, H. G. and Lordi, N. G., Axial to radial pressure transmission of tablet excipients using a novel instrumented die. *Drug. Dev. Ind. Pharm.* 19(17&18):2473-2497 (1993).

- (12) Timoshenko, S.P. and Goodier, J.N., *Theory of Elasticity*, 3rd edition, McGraw-Hill Inc., New York, (1970).
- (13) Champion, E. R. jr., Fundamentals of applied finite element analysis. In *Finite element analysis in manufacturing engineering: A pc-based approach*, McGraw-Hill Inc., New York, pp. 31-66 (1992).
- (14) COSMOS/M, *User Guide*, SRAC, (1990).
- (15) Dally, J. W. and Riley, W. F., Strain measurement methods and related instrumentation. In *Experimental stress analysis*, 3rd edition, McGraw-Hill Inc., New York, p 184 (1991).
- (16) Long, W. M., Radial Pressures in Powder Compaction. *J Powder Metall.* 6:73-86(1960).
- (17) Long, W. M., Die Design and Related Questions in Powder Compaction. In *Special Ceramics*, Academic Press, New York, pp. 327-340 (1962).
- (18) Leigh, S., Carless, J. E., and Burt, B. W., Compression characteristics of some pharmaceutical materials" *J. Pharm. Sci.* 56: 888-892 (1967).
- (19) Shotton, E. and Obiorah, B. A., The effect of particle shape and crystal habit on properties of sodium chloride. *J. Pharm. Pharmacol.* 25 Suppl.:37-43 (1973).
- (20) Obiorah, B. A. and Shotton, E., The effect of waxes, hydrolyzed gelatin and moisture on the compression characteristics of paracetamol and phenacetin. *J. Pharm. Pharmacol.* 28:629-632 (1976).
- (21) Krycer, I., Pope, D. G., and Hersey, J. A., The interpretation of powder compaction data - a critical review. *Drug. Dev. Ind. Pharm.* 8(3):307-342 (1982).



## **CHAPTER IV**

### **BEAD COMPACTS: I. COMPRESSION OF POLYMER COATED MULTI-LAYERED BEAD FORMULATIONS**

## ABSTRACT

Little information is available on the compactability of polymer coated beads into oral sustained release dosage forms. It is known that polymer coated beads may fuse together to produce a non-disintegrating controlled release matrix tablet when compressed. This study evaluates the effect of compression on beads with multiple layers of polymer and drug coat, and the effect of cushioning excipients and compaction pressure on drug release from compressed bead formulations. The multi-layered beads consist of several alternating layers of acetaminophen (APAP) and polymer coats (Aquacoat<sup>®</sup>) with an outer layer of mannitol or Avicel as a cushioning excipient. Percent drug release versus time profiles show that release of drug decreases from non-compacted beads as the amount and number of coatings increases, with only 43% of drug released in 24 hours for 10 layer coated beads. All polymer layers broke on compression, and both mannitol and Avicel as cushioning excipients were not effective in preventing bead fracture upon compaction of multi-layered beads, even at the very low pressure of 500 lb.. The results showed a loss of sustained release properties upon compaction. In general, compaction pressure greater than 500 lb. caused breaking and fusion of the polymer coating, leading to a useful sustained release non-disintegrating matrix caplet. If the caplet is crushed or disintegrates, the controlled release property were lost. Compaction pressures less than 500 lb. also resulted in disruption of all polymer coats and failed to produce intact caplets for larger size

coated beads. It is noted that overlaying large beads with Avicel results in readily compressible, non segregating formulations which may be useful for either immediate release or controlled release formulations.

## INTRODUCTION

Compression of polymer coated beads into tablets raises concerns regarding the segregation and mixing with cushioning excipients as well as integrity of the function of the polymer coat. The polymer coat must have the right combination of strength, ductility, and thickness to withstand the forces generated during compaction without rupturing. The need to develop such a dosage form arises from product tampering and the high cost of capsule production. Juslin et al. (1) reported an increase in drug release when acrylic-coated phenazone spheres were compacted at low pressure; however, at higher compaction pressures a decrease in drug release was observed. The slower drug release at a higher compaction pressure may be due to the fusion of the polymer coat, which forms a matrix. Chang and Rudnic (2) evaluated the effect of solvent and latex-based polymer coatings on potassium chloride crystals. They found that latex/pseudolatex films fractured upon compaction of coated crystals; however, solvent-based coatings caused only an insignificant increase in release rate compared to the non-compacted coated crystals. Bechard and Leroux (3) studied the effect of particle size and the use of various excipients in maintaining polymer coat integrity. They showed a loss of sustained release properties upon compaction of polymer coated

beads, which was also shown by Maganti and Celik (4) who concluded that regardless of the amount of coating applied, sustained release properties of the compacted coated beads were lost. A review of the limited information available in the literature on microparticulate compaction is given by Metin Celik (5).

In addition to polymer coat integrity, another major concern that has not been stressed in the literature is segregation of polymer coated beads from cushioning excipients during normal production conditions. The use of Avicel PH-101 as a cushioning agent in powder form (3, 6, 7), granulations (8), and in the form of spheres (9) has been investigated for the prevention of polymer coat fracture. It was thought that mixing placebo spheres of the same size as that of polymer coated spheres would solve the segregation problem. However, as investigated by Aulton et al. (10), the use of placebo spheres requires additional consideration of factors such as density and strength of the spheres. Ragnarsson et al. (11) were able to develop a rapidly disintegrating multiple-unit system comprising of polymer coated beads mixed with tablet forming excipients, however, there was no mention of the segregation that may occur during scale-up. A 1:1 mixture of microcrystalline cellulose and polyethylene glycol (PEG 8000) has previously been spray layered on polymer coated beads (12). These beads were then compacted without any additional tableting excipients, to produce a non-disintegrating matrix tablet which provided sustained release properties similar to the non-compacted polymer coated beads. The similarity in release may be happenstance with the intact matrix tablet controlling release while containing beads with ruptured coats.

The purpose of this study was to evaluate the effects of compression on a new design concept i.e. multi-layered beads with alternating multiple layers of polymer and drug coat. The rationale for the multi-layering was that when these multi-layered beads are compressed into caplets the outer layers would absorb the pressure and undergo fracture providing immediate release, while the innermost layers would be protected from fracture and provide sustained drug release. This study also examines the utility of spray coating cushioning excipients onto polymer coated beads to eliminate segregation and improve flow. In addition, the effect of cushioning excipient type and amount and compaction pressure on drug release from compressed multi-layered beads was investigated.

## EXPERIMENTAL

### Materials

Acetaminophen (4-Acetamido-phenol) (APAP) and dibutyl sebacate (sebacic acid dibutyl ester) were purchased from Sigma Chemical Co., St. Louis, MO; Polyvinylpyrrolidone K-25 (PVP) was supplied by GAF corporation; Hydroxypropyl ethylcellulose (HPC); Aquacoat<sup>®</sup> ECD-30 and Avicel<sup>®</sup> PH-101 samples were provided by FMC Corporation, Philadelphia, PA; triethyl citrate and mannitol were purchased from Morflex Chemical Co. Inc., Greensboro, NC and J. T. Baker Chemical Co., Phillipsburg, NJ, respectively; and Nu-Pariel PG - Sugar spheres 25/30 mesh from Crompton and Knowles Corp., Pennsauken, NJ.

### Coating Procedure

A weighed amount (100 g) of Nu-Pariel sugar beads were placed into the coating chamber of a fluid-bed spray coater with an Aeromatic<sup>®</sup> chamber over a Wurster column insert and fluidized for 20 minutes to equilibrate the temperature (40°C) of the coating process. The APAP drug solution was prepared in ethanol (95%) using HPC:PVP (1:2) as binders. The drug solution was then sprayed onto the beads. A 6% w/w polymer coat (Aquacoat<sup>®</sup> with 30% plasticizer i.e. dibutyl sebacate(DBS):triethyl citrate(TEC), 1:1) was applied over each drug layer on the beads. The 30% w/w plasticizer content with DBS:TEC (1:1) was selected based upon the findings of Hossain et al. (13) who reported that a better flexibility of the polymer coat is achieved with a combination of plasticizers (DBS:TEC) at the 30% level. Also, the glass transition temperature ( $T_g$ ) of Aquacoat (27% w/w ethylcellulose dispersion) decreases from 130°C to 43°C with 30% plasticizer added to Aquacoat. The lowering of  $T_g$  also prevents any flammable hazards associated with the drug coating solution in ethanol. Curing temperatures higher than 40°C caused tackiness among the beads, which lead to bead agglomeration. A 20 minute curing time at 40°C was allowed after each coating layer in order for the polymer coat to coalesce and form a film. Note that as multiple layers are applied to each batch of beads, layers which were 6% of previous batches becomes a smaller percent in the final product. This process of coating drug and polymer layers was repeated until the last layer (layer 10) of polymer coat was applied (see Figure IV.1, Table IV.1). A 14% w/w mannitol layer was applied under

the last polymer coat. Figure IV.1 represents the final polymer coat percentages by weight of a 10 layered bead. Since it was difficult to fluidize the beads in the coating chamber after the 10th layer, further polymer coating onto the beads was stopped. This was possibly due to the size of the individual beads getting bigger i.e.  $\sim 800$   $\mu\text{m}$ .

Multi-layered beads with Avicel PH-101 as the outer four layers were also prepared to determine the percentage of excipient needed to protect the polymer coats from fracturing upon compression. Avicel was coated as one big batch and the samples were collected after the 20, 40, 60 and 80% Avicel w/w coating layers were applied, this corresponds to layers 7, 8, 9 and 10, respectively (Table IV.2). Spray coating conditions for all ingredients are summarized in Table IV.3. These coating conditions can be optimized by using a bigger charge which will allow faster application of excipients onto beads with a higher efficiency leading to shorter processing times.

#### Bead Compaction and Dissolution Testing

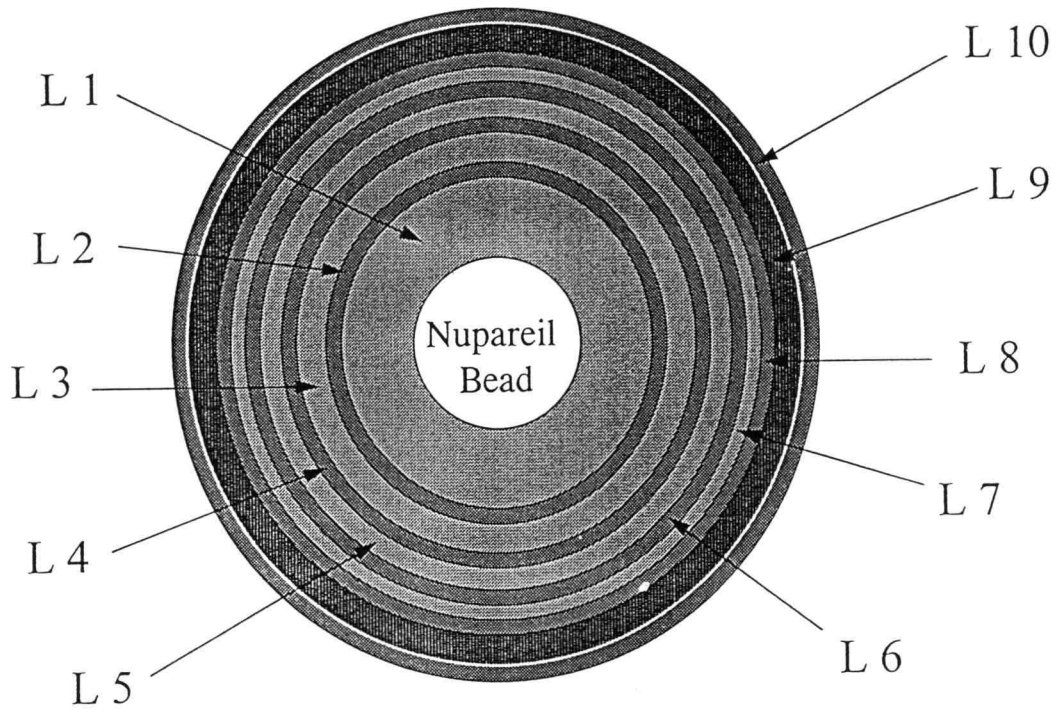
Caplets (1000 mg- capsule shaped tablets) were made on a Carver hydraulic press. The beads were compressed without the addition of any filler material and empirical observation showed them to have excellent flow characteristics. Dissolution studies on the uncompacted and compacted beads were conducted using USP dissolution apparatus II at 50 rpm with simulated intestinal fluid ( $\text{pH } 7.4 \pm 0.1$ ) maintained at  $37 \pm 0.5^\circ\text{C}$ . Samples (5 ml aliquot) were collected with replacement and after filtration and proper dilution samples were analyzed with a UV spectrophotometer

at  $\lambda = 244$  nm. All dissolution experiments were done in duplicate. The maximum standard deviation observed for any batch was not more than 5%; therefore, error bars were not included in the dissolution profiles to avoid visual complexity of the several dissolution curves in individual graphs.

#### Scanning Electron Microscopy (SEM)

An AmRay (model 1000A) microscope at an accelerating voltage of 10 kV was used for SEM. Samples for SEM were prepared by freezing the beads and caplets in liquid nitrogen and then fracturing the beads in a mortar with a pestle. Samples were also prepared by simply slicing the beads and caplets with razor blades. The samples were then coated with 60:40 gold/palladium alloy prior to microscopic examination. The samples prepared by two different techniques produced similar SEM results, as has been shown earlier in our laboratory (13).





IV.1 Cross sectional view of a 10 layer multi-layered bead. L = Layer number.

Table IV.1 Formulation Compositions for the Multi-Layered Beads

Layer #	L 1	L 2	L 3	L 4	L 5	L 6	L 7	L 8	L 9	L 10
Ingredient	(%)	(%)	(%)	(%)	(%)	(%)	(%)	(%)	(%)	(%)
Beads	56.0	52.6	43.3	40.9	34.0	32.0	26.9	25.3	21.6	20.3
APAP 1	44.0	41.4	34.2	30.5	24.2	23.0	19.0	17.5	15.2	14.3
AC 1	-	6.0	4.9	4.7	3.9	3.6	3.1	2.9	2.5	2.3
APAP 2	-	-	17.6	18.2	14.9	14.0	11.6	11.0	9.3	8.6
AC 2	-	-	-	5.7	4.7	4.4	3.7	3.5	3.0	2.8
APAP 3	-	-	-	-	18.3	17.0	14.0	13.2	11.0	10.4
AC 3	-	-	-	-	-	6.0	5.1	4.8	4.0	3.8
APAP 4	-	-	-	-	-	-	16.6	15.8	13.4	12.7
AC 4	-	-	-	-	-	-	-	6.0	5.1	4.8
M	-	-	-	-	-	-	-	-	14.9	14.0
AC 5	-	-	-	-	-	-	-	-	-	6.1

L = Layer on bead, APAP = Acetaminophen, APAP solution for all layers was prepared in Hydroxypropyl cellulose (2.2%): polyvinylpyrrolidone (4.5%); M = Mannitol; AC = Aquacoat with 30% w/w plasticizer (dibutyl sebacate:triethyl citrate, 1:1);.

Table IV.2 Formulation Compositions for the Multi-Layered Beads with Avicel PH-101 as the outer layers

Layer #	L 1	L 2	L 3	L 4	L 5	L 6	L 7	L 8	L 9	L 10
Ingredient	(%)	(%)	(%)	(%)	(%)	(%)	(%)	(%)	(%)	(%)
Beads	56.0	52.6	43.3	40.9	34.0	32.0	25.6	19.2	12.8	6.4
APAP 1	44.0	41.4	34.2	30.5	24.2	23.0	18.5	13.9	9.0	4.6
AC 1	-	6.0	4.9	4.7	3.9	3.6	2.9	2.2	1.5	0.7
APAP 2	-	-	17.6	18.2	14.9	14.0	11.0	8.4	5.6	2.8
AC 2	-	-	-	5.7	4.7	4.4	3.5	2.7	1.8	0.9
APAP 3	-	-	-	-	18.3	17.0	13.5	10.0	6.8	3.5
AC 3	-	-	-	-	-	6.0	4.8	3.6	2.4	1.2
AV 1	-	-	-	-	-	-	20.2	17.3	14.7	12.4
AV 2	-	-	-	-	-	-	-	22.7	19.3	16.3
AV 3	-	-	-	-	-	-	-	-	26.1	22.0
AV 4	-	-	-	-	-	-	-	-	-	29.2

L = Layer on bead, APAP = Acetaminophen, APAP solution for all layers was prepared in Hydroxypropyl cellulose (2.2%):Polyvinylpyrrolidone (4.5%); AC = Aquacoat with 30% w/w plasticizer (dibutyl sebacate:triethyl citrate, 1:1); AV = Avicel PH-101;.

Table IV.3 Spray coating conditions for the Multi-layered beads using a fluid-bed spray coater

Ingredients	Product Charge (g)	Inlet Air Temperature (°C)	Atomizing Air (psi)	Nozzle Diameter (mm)	Spray Rate (g/min)
APAP	100	40	18-20	1.2	2
Aquacoat*	100	<40	15-18	0.8	0.5
Mannitol	100	40	10-15	0.8	0.75
Avicel PH-101	100	40	18-20	0.8	0.4

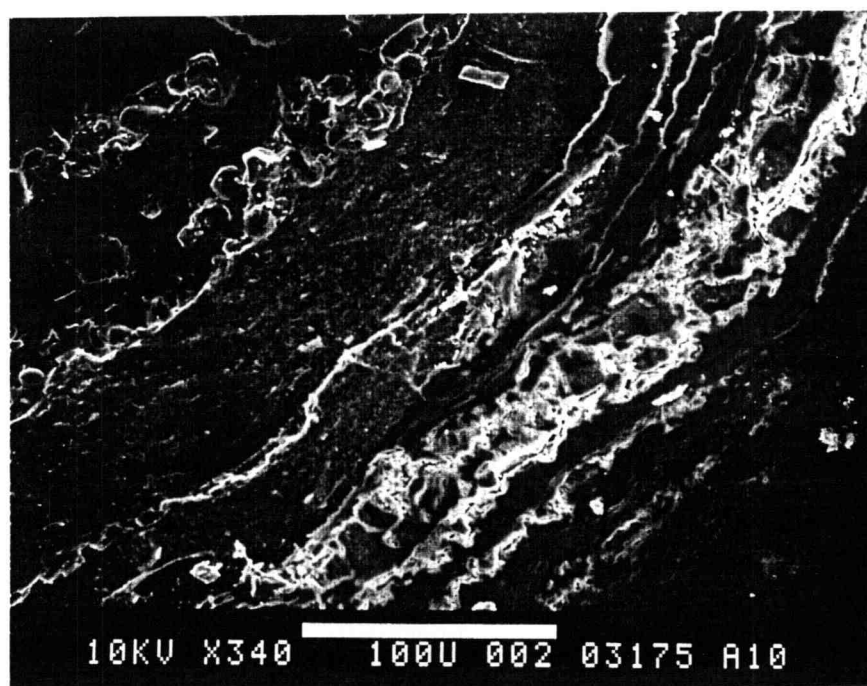
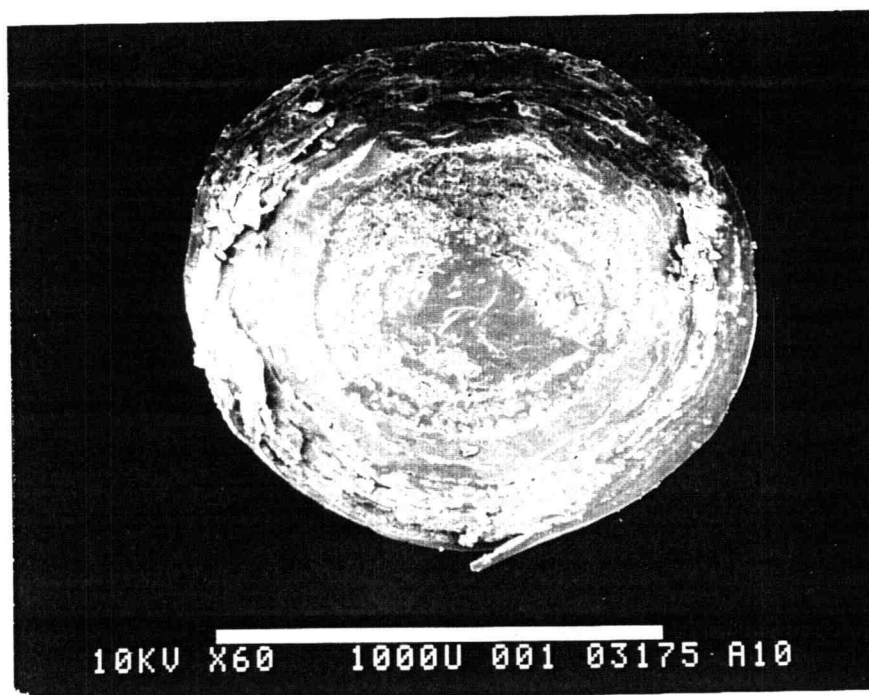
\* with 30% w/w plasticizer (dibutyl sebacate:triethyl citrate, 1:1)

## RESULTS AND DISCUSSION

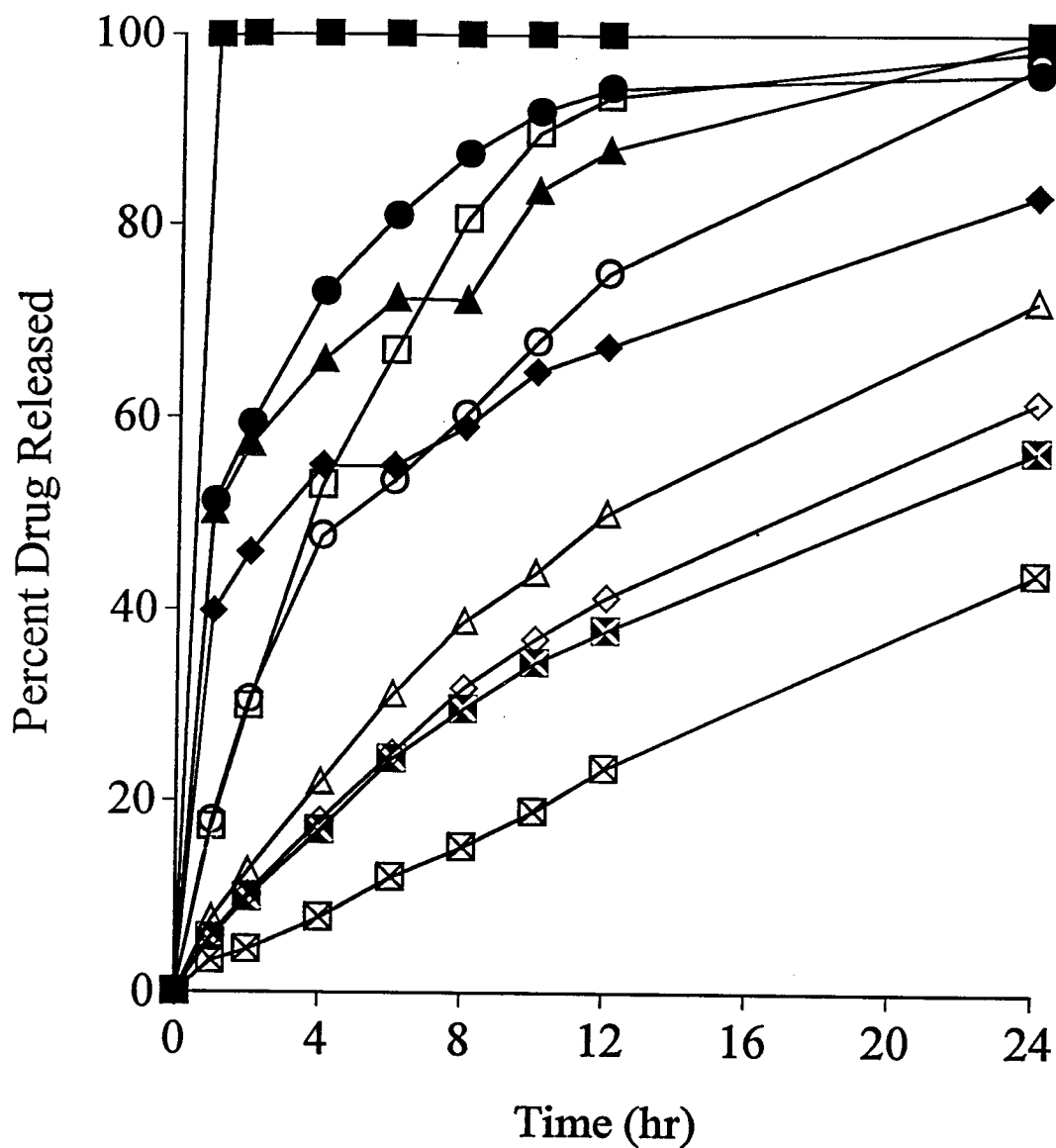
### Multi-Layered Beads

Multi-layered beads consisting of several alternating layers of APAP and polymer (Aquacoat) with an outer layer of mannitol or Avicel as an additional cushioning excipient (Figure IV.1). As shown in the photomicrographs (Figure IV.2) the drug/polymer layers are prominent, at higher magnification the layers are very distinct. Figure IV.1 shows artist's conception of a 10 layered bead. Percent drug release versus time profiles for non-compacted multi-layered beads are plotted in Figure IV.3. As expected, the percent drug release rate decreases as the amount of coating increases, with only 43% of drug being released in 24 hours for the highest level coated beads. Notice that the beads with an outer layer of drug releases drug at a faster rate even when there is a 6% w/w polymer coat underneath the final drug layer. However, mannitol as an outer layer does not result in greater drug release rate (see layer 8 and layer 9 profiles in Figure IV.3), possibly due to its non-hygroscopic nature.

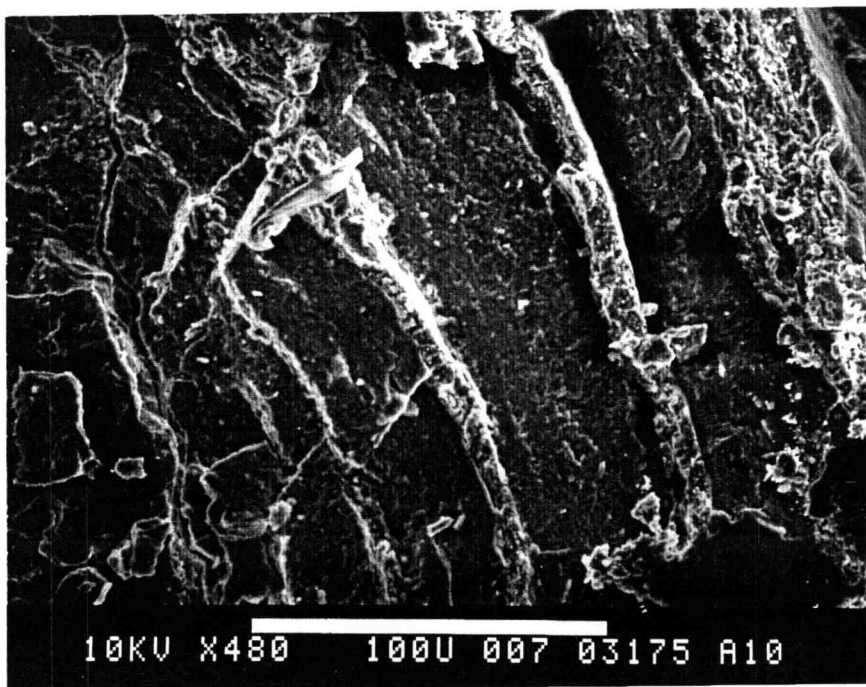
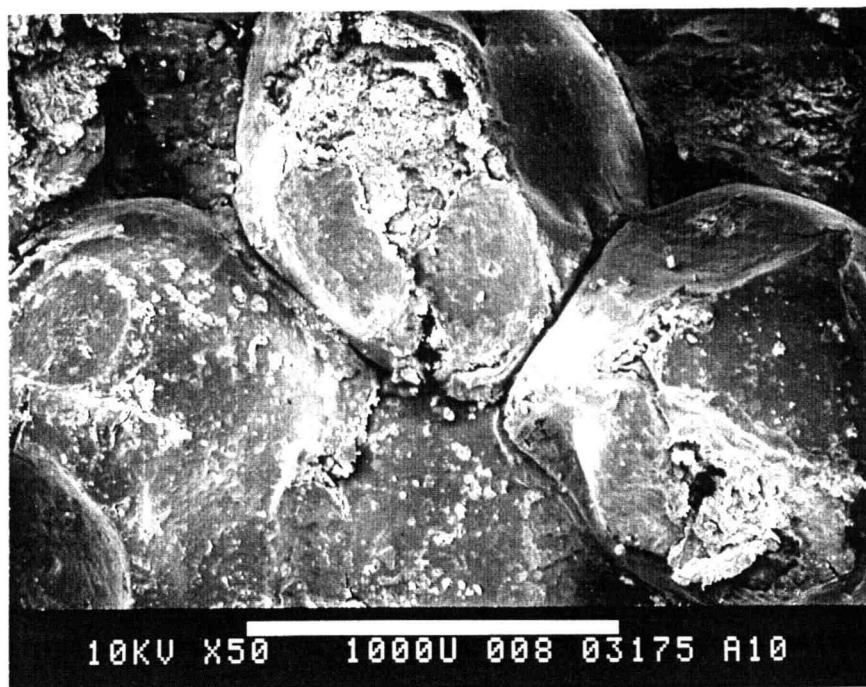
The multi-layered beads were then compressed into caplets at 500 lb pressure without the addition of any tableting excipient. Beads with 5 to 10 layers (Table IV.1) were used to study the compaction behavior of the multi-layered beads. Upon compaction, discrete beads can still be clearly distinguished within the caplet; however, significant deformation of the beads is observed (Figure IV.4). Compaction of the beads into caplets also leads to densification of the drug/polymer layers; cracks in some of the layers can also be observed (Figure IV.4). Figure IV.5 compares dissolution



IV.2 Scanning electron micrographs (SEM) of a L 10 Multi-Layered Bead; magnification, A = X60 & B =X340.

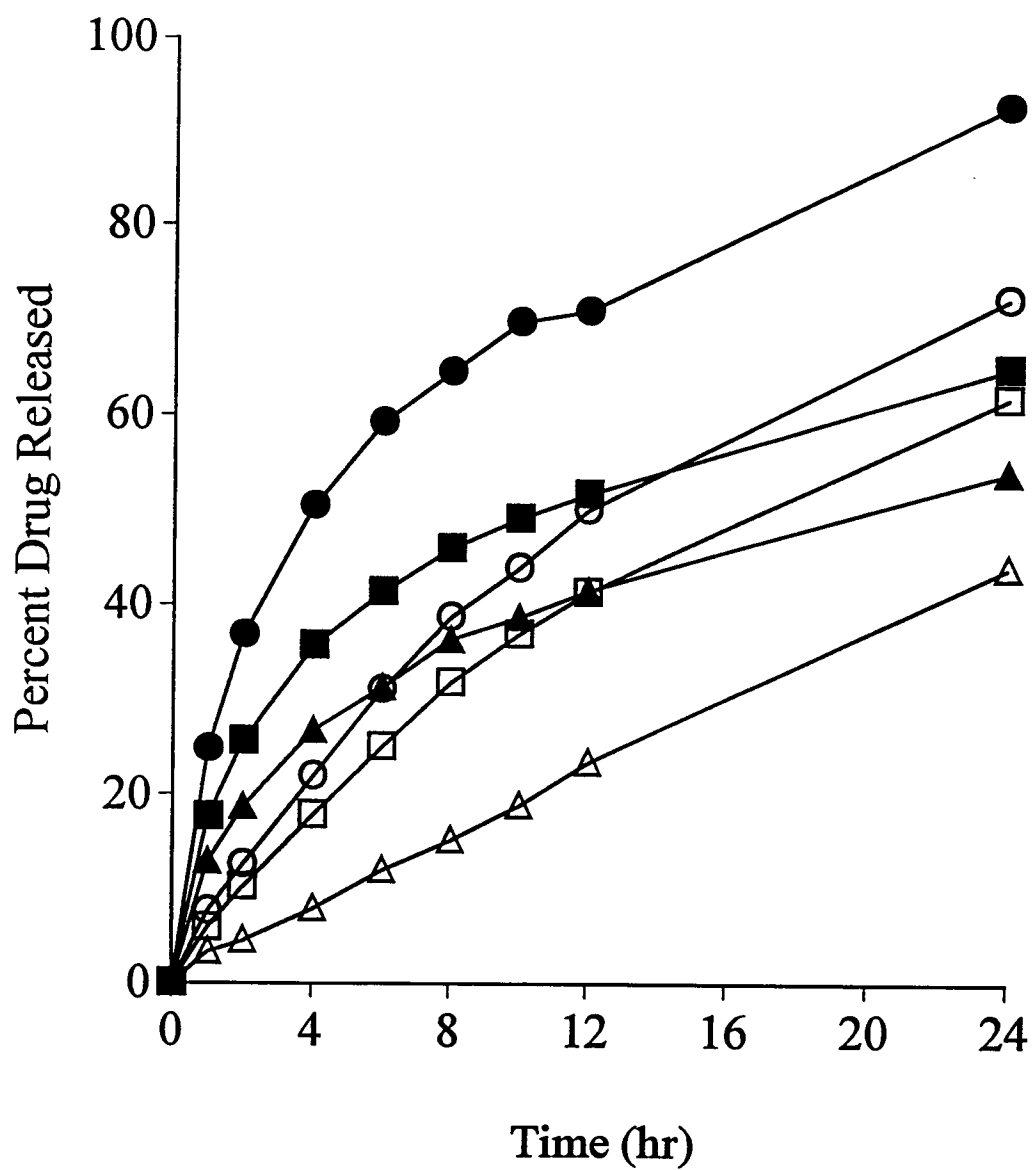


IV.3 Percent drug release versus time profiles for the non-compacted Multi-Layered Beads. ■ = L1, □ = L2, ● = L3, ○ = L4, ▲ = L5, △ = L6, ◆ = L7, ◇ = L8, ⊠ = L9, ⊞ = L10.



IV.4 SEM's of the deformed Multi-Layered Bead upon compaction at 500 lb.; magnification, A = X50 & B = X480.





IV.5 Dissolution profiles of the compacted (500 lb) versus non-compacted Multi-Layered Beads., ● = L6(Caplet), ○ = L6(Bead), ■ = L8(caplet), □ = L8(Bead), ▲ = L10(Caplet), △ = L10(Bead).

profiles of compacted (500 lb.) and non-compacted beads for layers 6, 8, and 10.

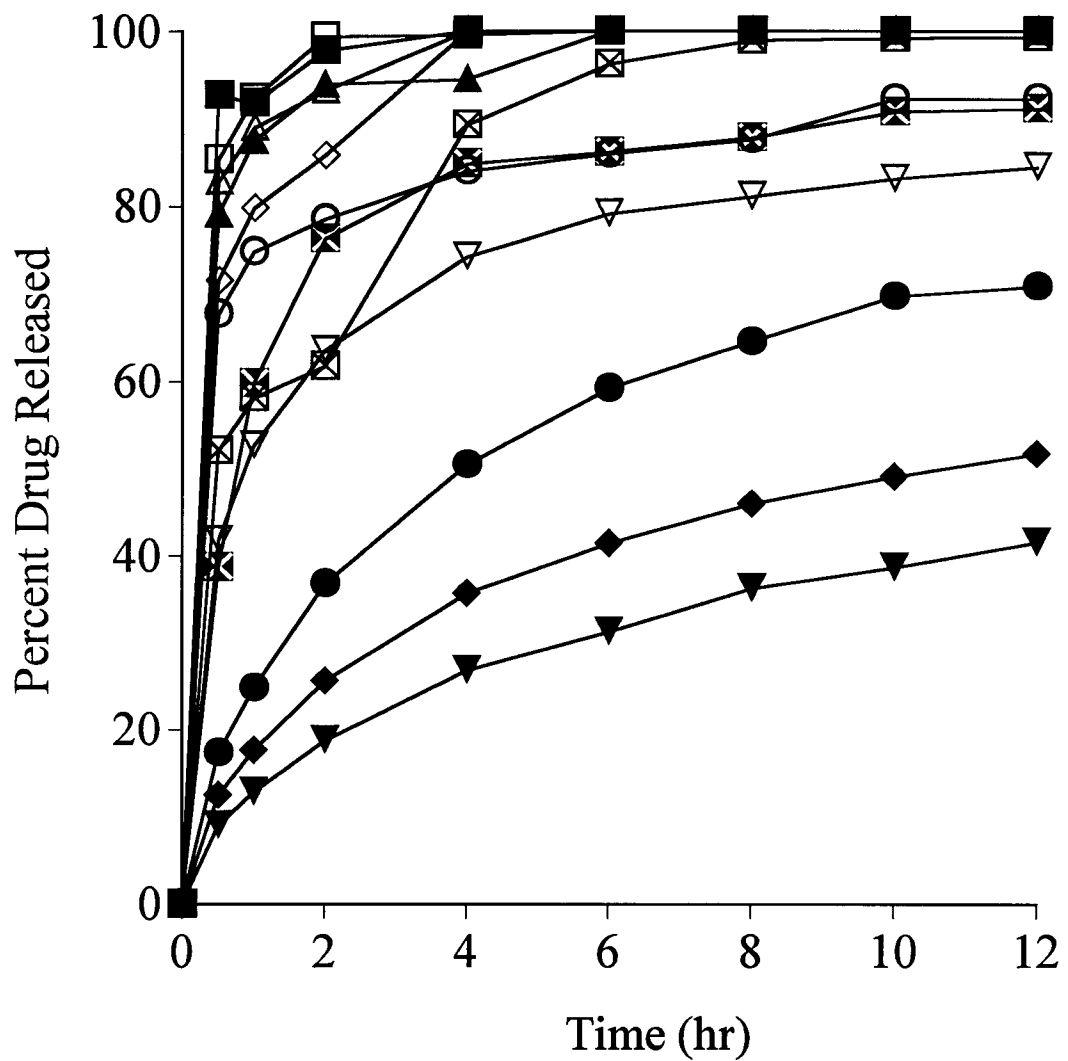
Release patterns show that compression resulted in an increase in drug release from caplets compared to non-compacted beads, indicating that bead coatings were ruptured.

Some of the caplets made with multi-layered beads at 500 lb pressure were gently crushed with a pill crusher and dissolution conducted to compare release profiles of intact and crushed caplets (Figure IV.6). Intact caplets with an outer layer of drug on the beads disintegrated in 2-3 minutes, and with mannitol as the outer layer disintegrated within 20 minutes. Caplets with 6 layers and polymer on the outside disintegrated after 12 hours, while layer 8 and 10 layered beads with outermost polymer coat formed non-disintegrating matrix. Non-disintegrating intact caplets with an outer layer of polymer coat on the multi-layered beads showed sustained release properties but released faster than the same non-compacted beads. Crushed or intact caplets with drug or mannitol as the outer layer released all drug in about 4 hours, except for the crushed caplet formulation containing the 10 layered beads. In this case, 50% of drug was released in 1/2 hour while the other 50% of drug was released over an 8 hour period (Figure IV.6). Multiple alternating layers of drug with polymer did not prevent cracking of polymer during caplet compression. Mannitol was not effective as a cushioning excipient in the prevention of bead fracture.

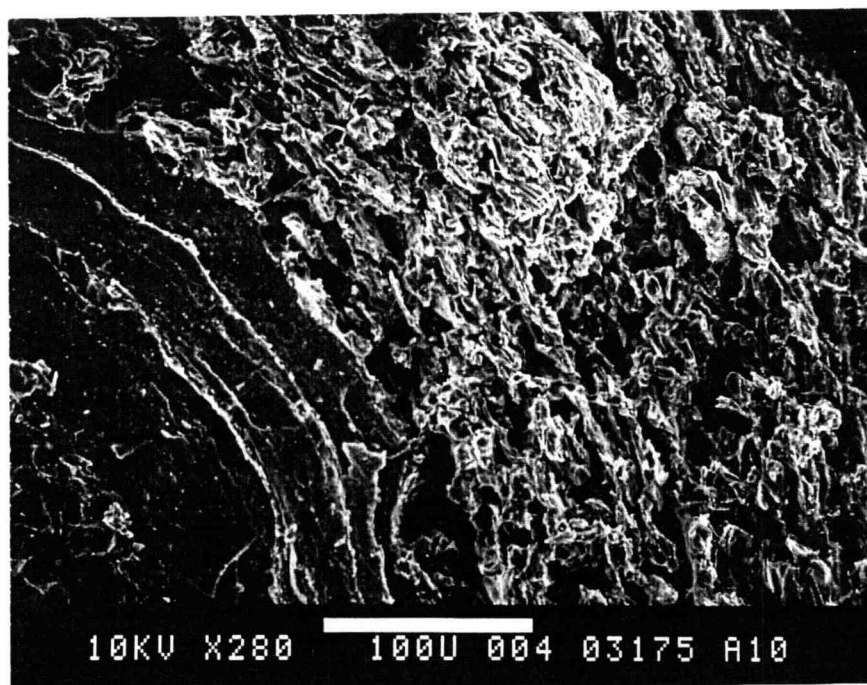
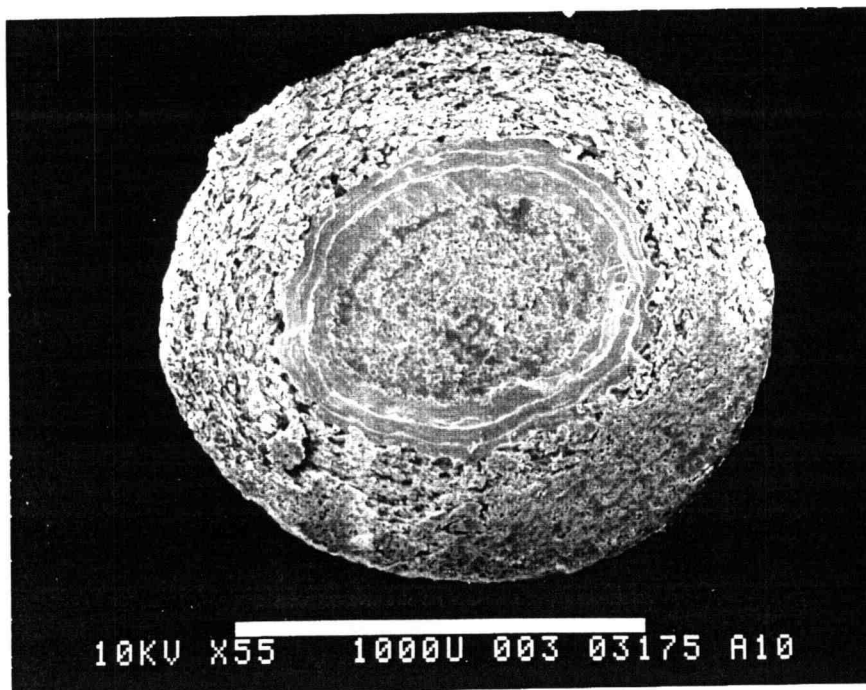
Figure IV.7 shows a cross-section of an Avicel coated non-compacted bead. Distinct drug, polymer, and Avicel layers are observed. Upon compaction at 100 lb.

pressure, deformation of the bead and densification of the drug/polymer layers is observed (Figure IV.8). Results show loss of sustained release properties upon compaction with total drug released in 4 hours (Figure IV.9), i.e., all polymer coats in the multi-layered beads were again disrupted. At lower pressures it was difficult to make physically stable caplets, especially with 80% Avicel coated beads. Thus, a mixture of different percentage Avicel coated beads were also compacted, where smaller beads would fill in the voids and form better quality caplets. For some combinations of Avicel coated beads, a pressure of 500 lb. rather than 100 lb. was required to produce physically stable caplets. The percentage Avicel coating on beads did not produce any significant effect on drug release from either non-compacted or compacted beads (Figure IV.9). Avicel was not effective as a cushioning agent.

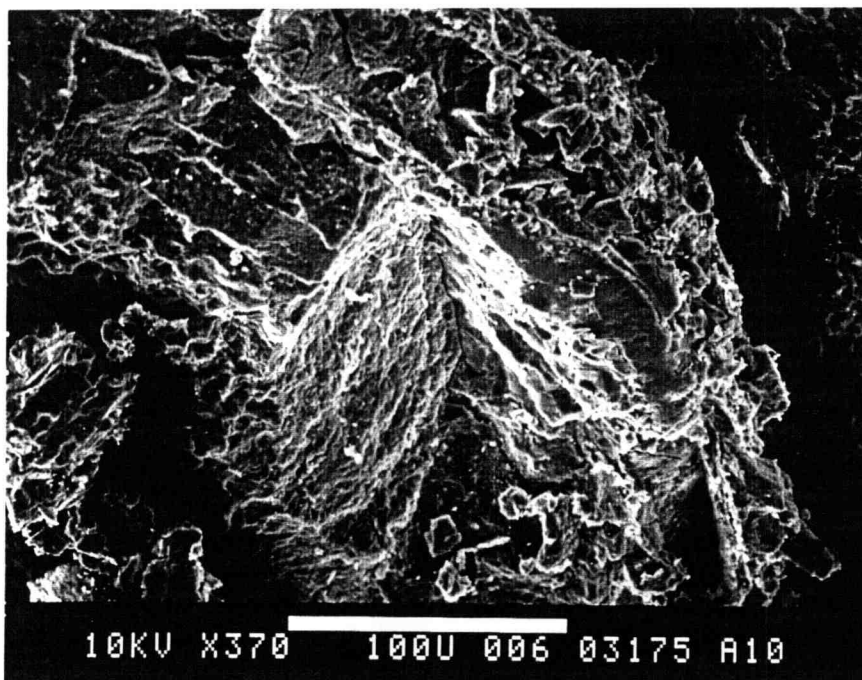
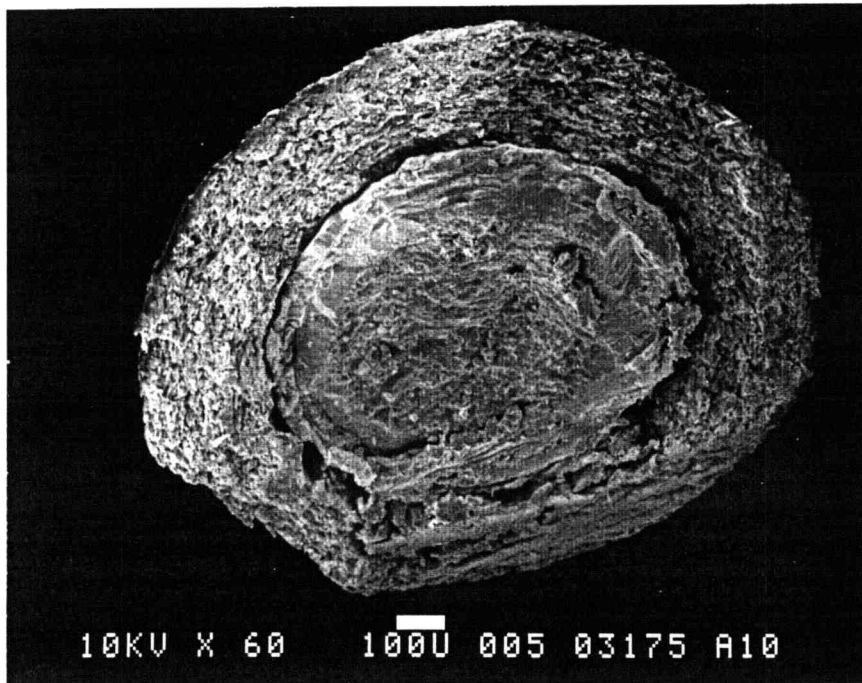
Multi-layered beads with Aquacoat as outer polymer layers upon storage in plastic or glass containers tended to agglomerate. With drug, mannitol or Avicel as the outer layers the beads do not stick to each other and a free flowing formulation is achieved which flows into the die which eliminates the need to hand fill the die with the beads for caplet compaction. Also, there is no need to mix the powdered excipients with polymer-coated beads with our system which avoids the segregation of two different size materials during normal production.



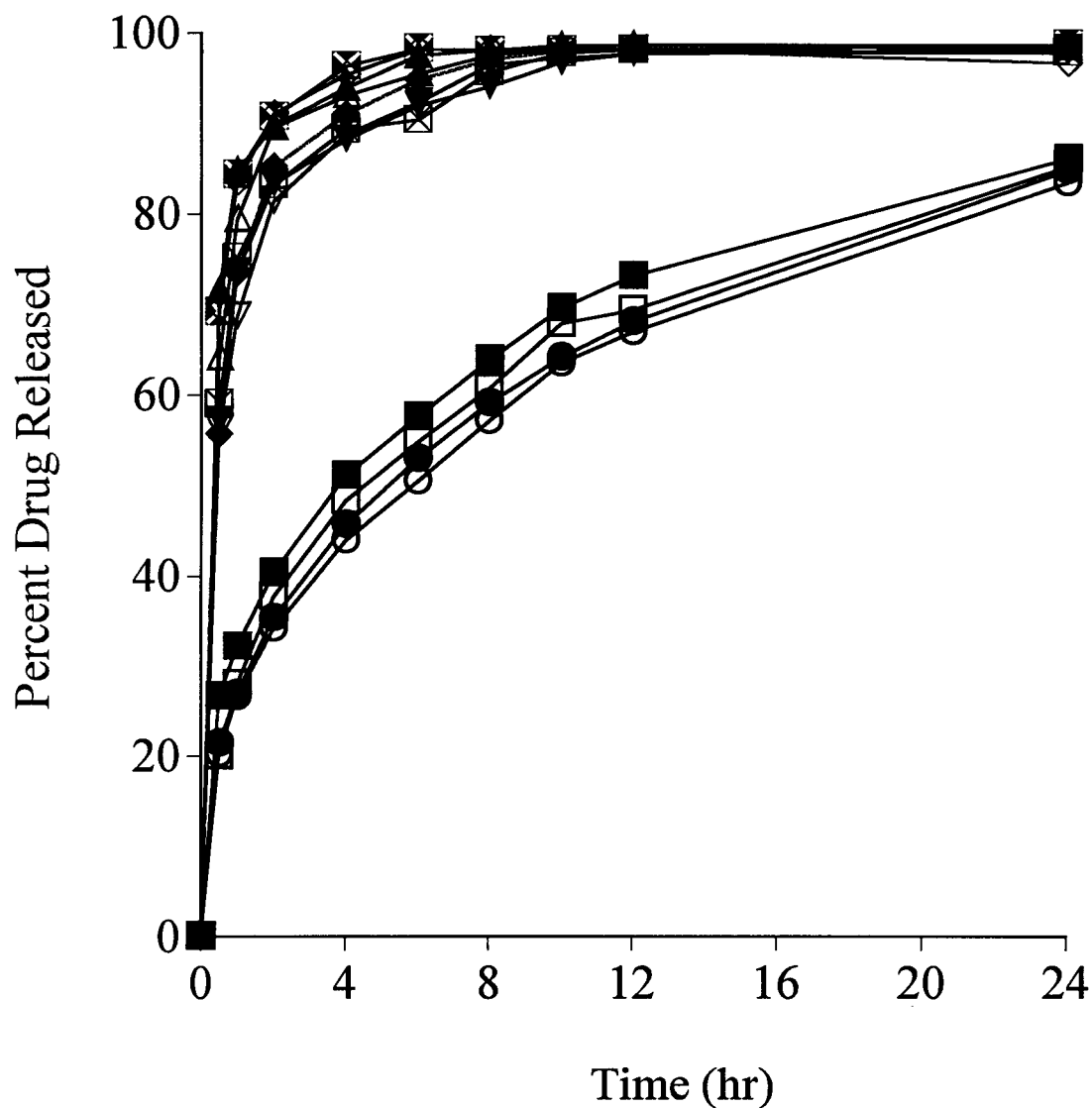
IV.6 Multi-Layered Beads compressed at 500 lb.: Effect of drug release from intact (IC) and crushed caplets (CC). ■ = L5(ic), □ = L5(cc), ● = L6(ic), ○ = L6(cc), ▲ = L7(ic), △ = L7(cc), ◆ = L8(ic), ◇ = L8(cc), ⊠ = L9(ic), ⊠ = L9(cc), ▼ = L10(ic), ▽ = L10(cc).



IV.7 SEM's of the cross section of non-compacted Avicel PH-101 coated Multi-Layered Bead; magnification, A = X55 & B = X280.



IV.8 SEM's of the cross section of deformed Avicel PH-101 coated Multi-Layered Bead upon compaction at 100 lb.; magnification, A = X60 & B = X370.



IV.9 Effect of Avicel PH-101 coating as cushioning excipient on drug release from compressed Multi-Layered Beads. ■=AV1, □=AV2, ●=AV3, ○=AV4, ▲=AV1@100lb., △=AV2@100lb., ◆=AV3@100lb., ◇=AV1+AV2@100lb., ⊞=AV1+AV3@500lb., ⊠=AV2+AV3@100lb., ▼=AV2+AV4@500lb., ▽=AV3+AV4@500lb..

## CONCLUSIONS

The effect of compression on multi-layered beads was investigated and it was found that the amount of polymer coating, compression pressure, bead size and type of cushioning excipient affects drug release characteristics. Although upon compaction, permanent deformation of the beads was observed and polymer coats were broken, spray coating of cushioning excipient onto beads can provide an effective way to prevent segregation associated with mixing of the polymer coated beads and powdered or spherical/non-spherical cushioning excipients. Spray coating of cushioning excipient also provides excellent flow properties of the final formulation as visually observed in our experiments.

The sustained release property of the multi-layered coated beads was lost upon compaction. At higher compression pressures (>500 lb.) fusion of the broken polymer coats occur which leads to a sustained release non-disintegrating matrix caplet. Crushing of these caplets eliminates the sustained release characteristics of the resultant non-disintegrating matrix caplets, confirming that polymer coats were disrupted during compaction. It is concluded that beads of drug prepared by any method can be layered with excipients such as Avicel and mannitol. Also, larger size beads, especially with Avicel as the outer coating layer are hard to compress into intact caplets. In such cases higher pressures (>1000 lb.) are required to make acceptable caplets.



## ACKNOWLEDGMENTS

The authors wish to thank Eli Lilly and company for partial financial support. The authors would also like to thank Al Soldner for the SEM work and FMC Corp. and Crompton and Knowles Corp. for the generous donation of excipient samples and sugar spheres, respectively.

## REFERENCES

- (1) Juslin, M.; Turakka, L.; Puumalainen, P. *Pharm. Ind.* 42:829 (1980).
- (2) Chang, R.-K.; Rudnic, E. M., The effect of various polymeric coating systems on the dissolution and tableting properties of potassium chloride microcapsules. *Int. J. Pharm.* 70:261-270 (1991).
- (3) Béchard, S. R.; Leroux, J. C., Coated Pelletized Dosage Form: Effect of Compaction on Drug Release *Drug. Dev. Ind. Pharm.* 18(18):1927-1944 (1992).
- (4) Maganti, L.; Celik, M., Compaction studies on pellets: II. Coated pellets. *Int. J. Pharm.* 103:55-67 (1994).
- (5) Celik, M. In *Multiparticulate Oral Drug Delivery*, Marcel Dekker Inc., New York, pp. 181-215 (1994).
- (6) Ruiz, R.; Sakr, A.; Sprockel, O. L., A study on the manufacture and in vivo dissolution of terbutaline sulfate microcapsules and their tablets. *Drug. Dev. Ind. Pharm.* 16(11):1829-1842 (1990).
- (7) Sayed, H. A. M.; Price, J.C., Tablet properties and dissolution characteristics of compressed cellulose acetate butyrate microcapsules containing succinyl sulfathiazole. *Drug. Dev. Ind. Pharm.* 12(4):577-587 (1986).
- (8) Torrado, J. J. ; Augsburger, L. L., Effect of different excipients on the tableting of coated particles. *Int. J. Pharm.* 106:149-155 (1994).
- (9) Celik, M.; Maganti, L., Formulation and compaction of microspheres. *Drug. Dev. Ind. Pharm.* 20(20):3151-3173 (1994).
- (10) Aulton, M. E.; Dyer, A. M.; Khan, K., The strength and compaction of millispheres: The design of a controlled-release drug delivery system for ibuprofen in the form of a tablet comprising compacted polymer-coated millispheres. *Drug. Dev. Ind. Pharm.* 20(20):3069-3104 (1994).
- (11) Ragnarsson, G.; Sandberg, A.; Jonsson, U. E.; Sjögren, J., Development of a new controlled release metoprolol product. *Drug. Dev. Ind. Pharm.* 13(9-11):1495-1509 (1987).

- (12) Colorcon<sup>®</sup> Bulletin, Surelease<sup>®</sup> 0601-78 coating for chlorpheniramine maleate non-pareils compressed into tablets., West point, PA. (1994).
- (13) Hossain, M, Ph. D. Thesis, Oregon State University (1992).

**CHAPTER V****BEAD COMPACTS: II. EVALUATION OF RAPIDLY DISINTEGRATING  
FORMULATIONS FROM COMPRESSED POLYMER-COATED BEADS****Syed A. Altaf, Stephen W. Hoag, and James W. Ayres**

## ABSTRACT

In this study several formulation approaches were investigated for their ability to prevent polymer coat fracture upon compaction of sustained release beads into tablets. In one case polymer-coated beads were overcoated with 20% polyethylene glycol (PEG), 10% Avicel, and 5% disintegrant. These beads were compressed at 125, 500, and 1000 lb. pressure into caplets or tablets of 5 kg hardness, and dissolution profiles indicated that the polymer coat was disrupted during compaction. All caplets and tablets disintegrated into individual beads when the dissolution medium was switched from simulated gastric to intestinal fluid. Polyethylene oxide (PEO) was spray coated over Aquacoat coated beads in a second approach. These beads were then coated with Avicel and a disintegrant. The beads upon compaction showed sustained release properties for 8 hours. Triple layered caplets (TLC) were also prepared with outer layers of Avicel PH-101 or polyethylene oxide (PEO), and a center layer of polymer coated beads. The polymer coating on the beads fractured, and non-disintegrating matrix formulations were obtained with both caplet formulations. Drug release from the PEO based TLC was affected by the swelling/diffusion characteristics of the PEO caplet layers. Polymer coated beads were also granulated with cushioning excipient and compressed. This approach also resulted in ruptured polymer coat on the beads but provide a partially disintegrating matrix caplet which showed sustained drug release for 24 hours. It was concluded

that segregation during product manufacturing can be avoided by spray coating excipients onto beads instead of mixing powdered excipients with spherical beads. Also, drug release from compressed bead formulations was affected by polymer coat thickness, bead size, compression pressure, and excipient type.

## INTRODUCTION

Rapid disintegration of a compressed bead formulation into its individual units has the advantage of minimizing the risk of dose dumping and product tampering, lower production cost than capsules, and ease of esophageal transport. These systems include compaction of polymer-coated beads into tablets (1-8), emulsion-solvent evaporation to produce microcapsules (9-11), extrusion/marumerization technology for bead manufacture (12), coated-particle compacts (13), melt granulation technique for individual dose units (14), and microencapsulation techniques (15-17). Most of these systems require the use of excipients that act as cushioning agents and allow for rapid disintegration of compressed beads. The cushioning agents are powders which are mixed with the polymer coated beads or particles before compression into a tablet, leading to one major concern that has not been stressed in the literature i.e. segregation of polymer coated beads or granules from cushioning excipients during normal production. Laboratory samples can be prepared by hand loading each die during production of a single tablet, but in scale-up of the process segregation of the different size materials will occur during product development (18-19).

Use of microcrystalline cellulose as a cushioning agent in powder form (3, 6, 7), in the form of spheres (9), and as granules (13) has been investigated for the prevention of polymer coat fracture. It was thought that mixing placebo spheres of the same size as polymer coated spheres would solve the segregation problem. However, as investigated by Aulton et al. (2), the use of placebo spheres require additional consideration of factors such as density and strength of the spheres. The pilot study done by Aulton et al. did not show a segregation problem, but the authors suggest that segregation could occur upon scale-up. Ragnarsson et al. (1) were able to develop a rapidly disintegrating multiple-unit system comprising of polymer coated beads mixed with tablet forming excipients. There was no mention of how the segregation problem was solved. A 1:1 mixture of microcrystalline cellulose and polyethylene glycol (PEG 8000) has previously been spray coated on polymer coated beads (6). These beads were then compacted without any additional tableting excipients and a non-disintegrating matrix tablet was produced which provided sustained release properties similar to the non-compacted polymer coated beads.

The current study is an extension of an earlier study done by the authors (see chapter IV); in that study the effects of compression on beads with alternating multiple layers of drug and polymer was examined. This study evaluates four new concepts in the development of compressed polymer coated beads that would minimize segregation. They are Excipient / disintegrant coated bead compacts, Sealant-effect compacts, Triple-layered caplets, and Granulated bead compacts. In addition, the

effect of cushioning excipient type, compaction pressure, polymer coat thickness, and bead size on drug release from compressed bead formulations were investigated.

## EXPERIMENTAL

### Materials

Acetaminophen (4-Acetamido-phenol) and Dibutyl sebacate (Sebacic Acid Dibutyl Ester) were purchased from Sigma Chemical Co., St. Louis, MO; Polyvinylpyrrolidone K-30 was supplied by E. M. Science, Gibbstown, NJ; Hydroxypropyl cellulose was purchased by Aqualon, Wilmington, DE; Aquacoat<sup>®</sup> ECD-30 and Avicel<sup>®</sup> PH-101 samples were provided by FMC Corporation, Philadelphia, PA; Triethyl Citrate was purchased from Morflex Chemical Co. Inc., Greensboro, NC; Polyethylene glycol (PEG 8000) and polyethylene oxide (Polyox N-3000) were supplied by Union Carbide Corporation, Danbury, CT; Sodium Starch Glycolate (Explotab) was supplied by Edward Mendell Co., Patterson, NY; and Nu-Pariel PG - Sugar spheres 25/30 & 45/60 mesh from Crompton and Knowles Corp., Pennsauken, NJ.

### Coating Procedure

A weighed amount (100 g) of Nu-Pariel sugar beads were placed into the coating chamber of a fluid-bed spray coater with an Aeromatic<sup>®</sup> chamber over a Wurster column insert and fluidized for 20 minutes to equilibrate with the temperature (40°C) used in the coating process. The drug-binder solution in ethanol (95%) was



then sprayed onto the beads. The drug layered beads were then spray coated with different percentages by weight of the solids content of Aquacoat (with 30% plasticizer, DBS:TEC (1:1)). The same process of coating drug, different polymer layers, cushioning excipients and disintegrant were applied to all the formulations studied (Table V.1). Spray coating conditions for all ingredients are summarized in Table V.2.

#### Bead Compaction and Dissolution

Caplets (1000 mg- capsule shaped tablets) were made on a Carver hydraulic press by compressing coated beads at different compaction pressures. Formulation G was also compressed with a single punch press. Beads were compressed without addition of any filler material. Empirical observation showed these coated beads to have excellent flow characteristics as observed by Hadley et al. (20). In case of granulated bead compacts, formulation D beads were granulated with 30%w/w Avicel PH-101 using 54.5% w/w deionized water (21). The granulation was sieved through 25/35 mesh screen and dried in a vacuum oven overnight. The dried granulation was then passed through a 8/10 mesh screen. The screening of the dried granules produced <5 % fines and the granules obtained were physically stable. Dissolution studies on non-compacted and compacted beads were conducted using USP dissolution apparatus II at 50 rpm with simulated gastric (pH 1.4±0.1) for 2 hours followed by simulated intestinal fluid (pH 7.4±0.1). The temperature was maintained at 37±0.5°C. Samples (5 ml aliquot) were collected with replacement and after filtration and proper dilution, the samples were analyzed with a UV spectrophotometer at  $\lambda=244$  nm. All dissolution studies were

done at least in duplicate and the average of the runs are plotted. Percent drug released was calculated based upon the maximum amount released from the formulations after running dissolution for a maximum of 72 hours.

Table V.1 Percentage Compositions for the Various Bead Formulations

Formulation Ingredient	A (%)	B (%)	C (%)	D (%)	E (%)	F (%)	G (%)	H (%)	I (%)
Nupariel Beads	45.5	42.75	32.75	40	30	27.5	22.5	28	21
APAP	45.5	42.75	32.75	40	30	27.5	22.5	28	21
Aquacoat	9	14.5	14.5	20	20	20	20	9	6
APAP	-	-	-	-	-	-	-	-	13
Aquacoat	-	-	-	-	-	-	-	10	6
PEG 8000	-	-	20	-	20	20	20	-	-
Polyox N3000	-	-	-	-	-	-	-	10	33
Avicel PH-101	-	-	-	-	-	-	10	10	-
Explotab	-	-	-	-	-	5	5	5	-

APAP = Acetaminophen, APAP solution for all layers was prepared in Hydroxypropyl cellulose (2.2%); polyvinylpyrrolidone (4.5%); Aquacoat dispersions were added with 30% w/w plasticizer (dibutyl sebacate:triethyl citrate, 1:1).

Note: In formulation I, Polyox is not spray coated but applied as top and bottom layers of a triple layer caplet.

Table V.2 Coating conditions for the Various bead Formulations on a Fluid-Bed Spray Coater

Ingredients	Product Charge (g)	Inlet Air Temperature (°C)	Atomizing Air (psi)	Nozzle Diameter (mm)	Spray Rate (g/min.)
APAP	100	40	18-20	1.2	2
Aquacoat*	100	<40	15-18	0.8	0.5
Polyethylene Glycol	100	40	10-15	0.8	0.75
Avicel PH-101	100	40	18-20	0.8	0.4
Polyox N3000	100	40	10-15	0.8	0.25
Explotab	100	40	15-20	0.8	0.5

\*with 30% w/w plasticizer (dibutyl sebacate:triethyl citrate, 1:1)

## RESULTS AND DISCUSSION

Effect of Polymer Coat Thickness:

The effect of polymer coat thickness on drug release from different size beads at different pressures was included in this investigation. The following equation was used to predict coating wall thickness for the two different size beads (Madan et al., 1974):

$$t = (W_w / W - W_w) (P / P_w) (d / 6) \quad (\text{Equation 1})$$

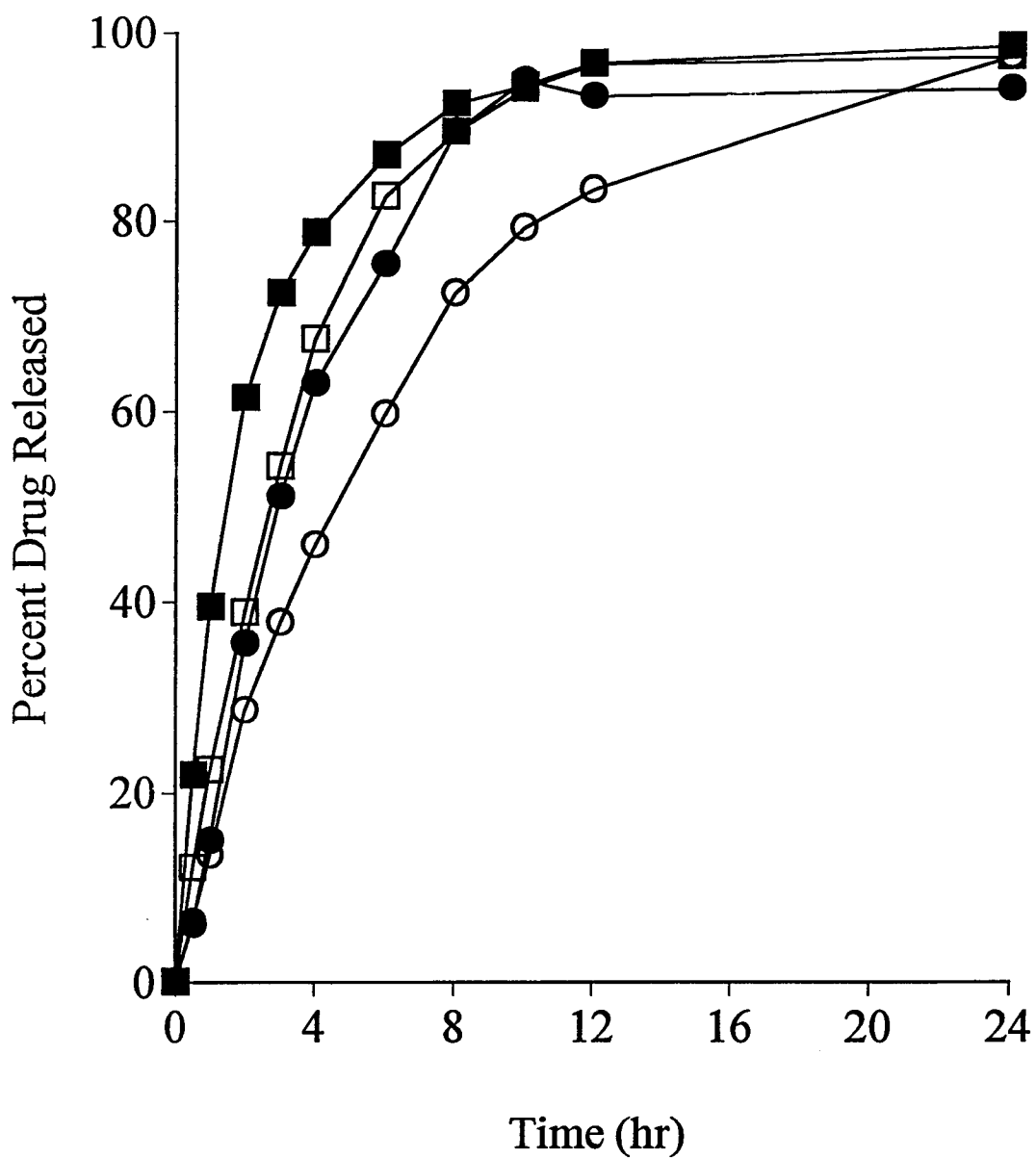
where,  $t$  = wall thickness,  $W_w$  = weight of wall (coating) material recovered,  $W$  = weight of coated particles taken,  $P_w$  = density of the encapsulated (core drug bead particles),  $P$  = density of wall material,  $d$  = diameter of the uncoated particle.

A theoretical coat thickness of  $\sim 8 \mu\text{m}$  was obtained when a 6% w/w polymer coat was applied on 25/30 mesh drug beads. The same 6%w/w coating on 30/40 and 40/60 mesh beads predicted different thickness of polymer coats i.e.  $5.17 \mu\text{m}$  and  $3.04 \mu\text{m}$ , respectively. So, when the Equation 1 was used to calculate the amount of coating needed for a wall thickness of  $\sim 8 \mu\text{m}$  on 30/40 or 40/60 mesh beads, it was determined that a polymer coat of 9% (Formulation A) and 14.5% (Formulation B) is required, respectively. This is due to the larger surface area of the smaller size beads, requiring more polymer coat to achieve the same thickness. Figure V.1 shows drug release profiles for caplets made with two different bead sizes that have the same polymer coat thickness. It can be seen that caplets made from 40/60 mesh bead released drug at a

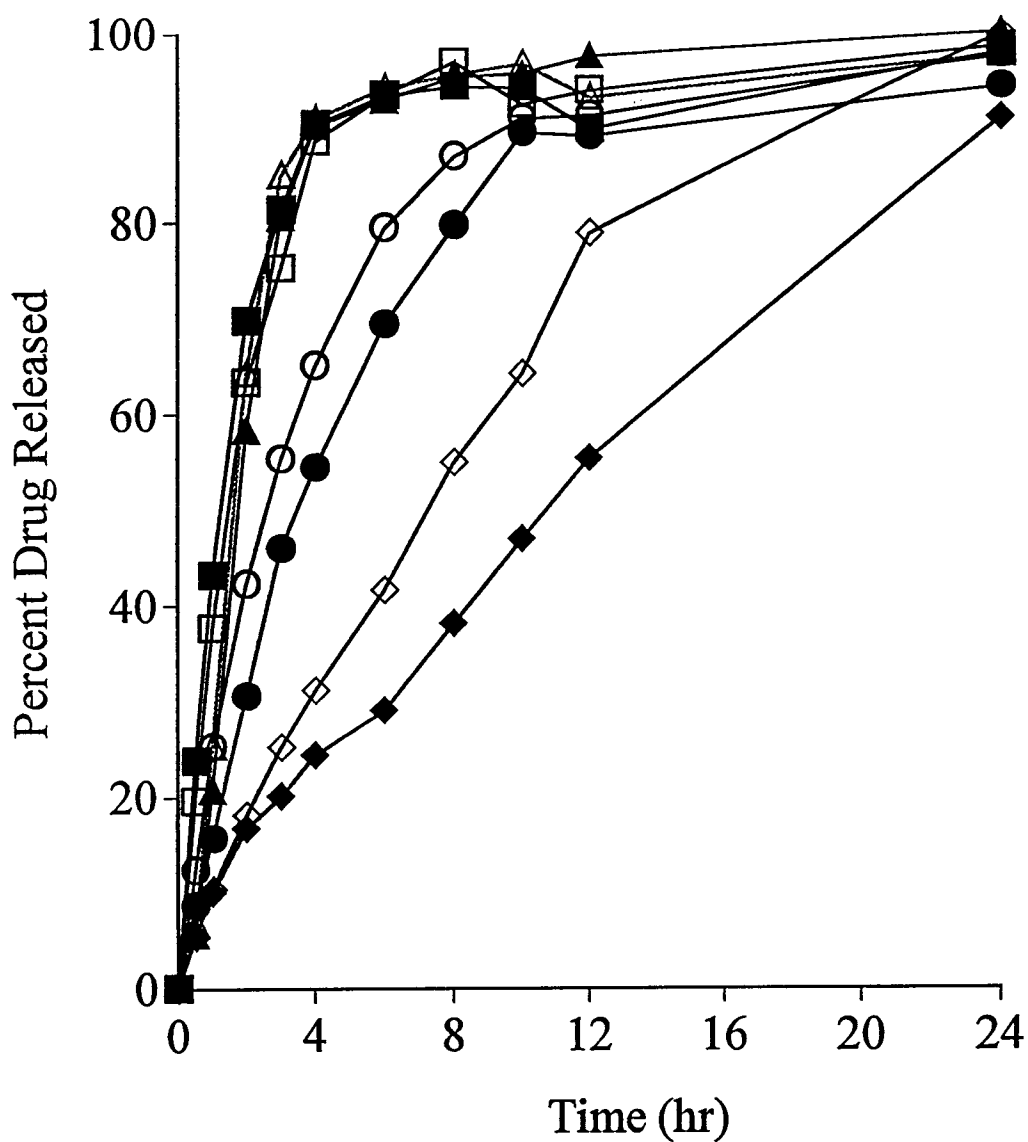
slower rate than the caplets made with 30/40 mesh beads. Drug release was even slower when compaction pressure was increased from 300 lb. to 800 lb. producing a non-disintegrating sustained release matrix. In this case, diffusion through the non-disintegrating matrix is controlling release since release is slower than occurs from non-compacted beads.

The 14.5% Aquacoat coated formulation B beads (Table V.1) were screened to obtain beads retained on 30/40 or 40/60 mesh. These beads were then spray coated with 20% Polyethylene glycol (PEG 8000) (formulation C). Results of dissolution are shown in Figure V.2 and it can be seen that the bigger size beads (30/40 mesh) tend to have slower release of the drug than smaller size beads (40/60 mesh), due to the difference in polymer coat thickness for the two size beads. Smaller beads however were observed to form physically more stable caplets at a lower compression pressure. Beads compacted at 300 and 500 lb. pressure released all drug in about 4 hours while beads compacted at 800 lb. produced a non-disintegrating matrix caplet with constant drug release for 24 hours for both size beads (Figure V.2).

Since 14.5% Aquacoat was not enough to prevent film fracture upon compaction (Figure V.2), a 20% Aquacoat was spray coated onto drug-layered beads (formulation D), which was then coated with 20% PEG 8000 (formulation E). The beads were compacted at 300 lb. pressure and as seen from Figure V.3, the release of drug was sustained for 6 hours with 40% drug released in 6 hours and then a burst



V.1 Effect of polymer coat thickness on drug release from different size beads. ● = 40/60 mesh (14.5%) @ 300lb., ○ = 40/60 mesh (14.5%) @ 800lb., ■ = 30/40 mesh (9%) @ 300lb., □ = 30/40 mesh (9%) @ 800lb.



V.2 Effect of bead size on drug release from compressed beads at different compaction pressures. ● = 30/40 mesh uncompacted beads, ■ = 30/40 mesh @ 300 lb., ▲ = 30/40 mesh @ 500 lb., ◆ = 30/40 mesh @ 800 lb., ○ = 40/60 mesh uncompacted beads, □ = 40/60 mesh @ 300 lb., △ = 40/60 mesh @ 500 lb., ◇ = 40/60 mesh @ 800 lb.

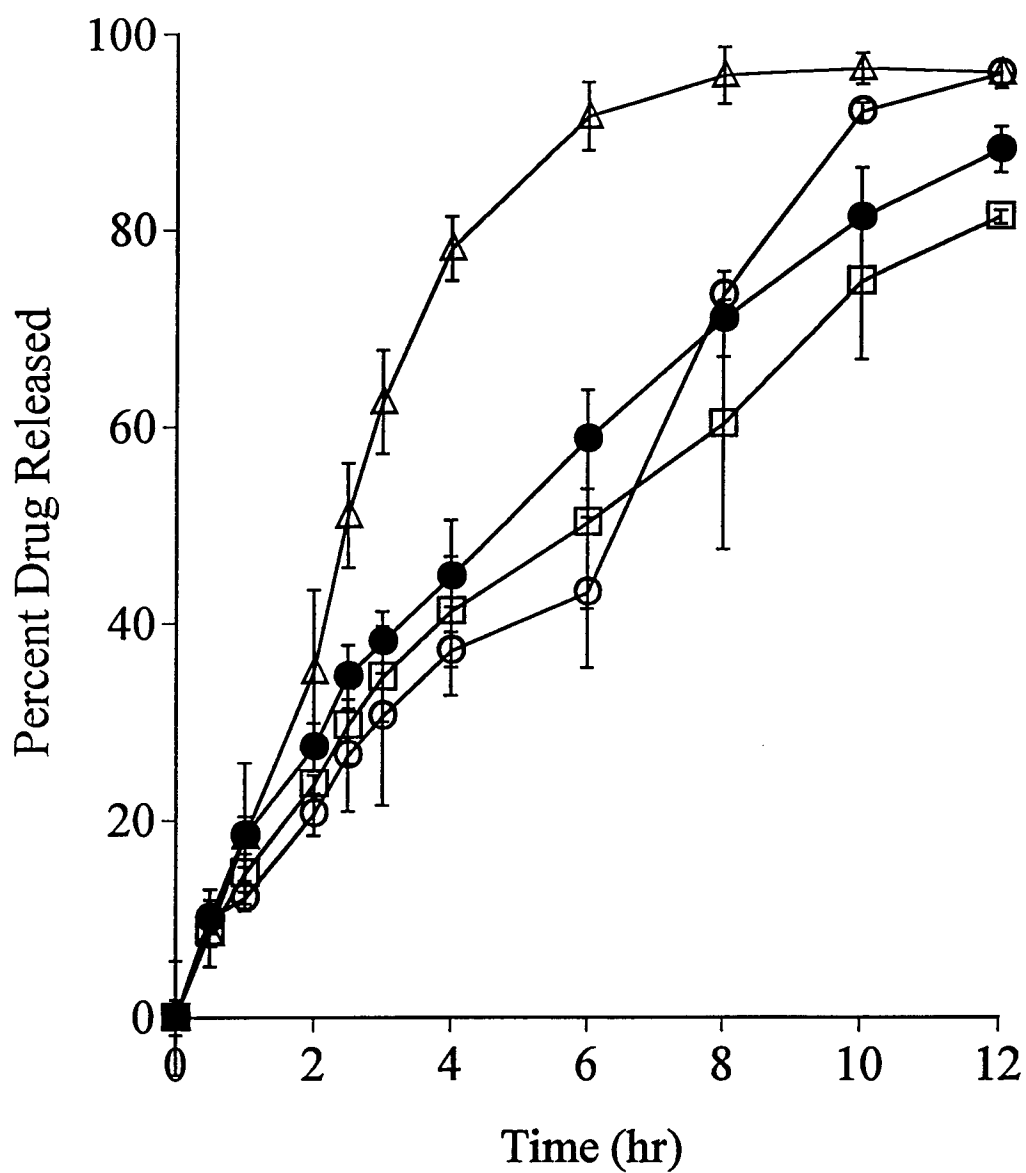


effect is observed, releasing the remaining 60% drug in the next 6 hours. These caplets disintegrated into individual beads after 4 hours. However, when formulation E beads were compressed at a 10 times higher pressure of 3150 lb., drug release profiles for the beads and caplets were very similar. This may be due to fusion of the polymer film at the higher pressure forming a non-disintegrating matrix, thereby slowing the drug release.

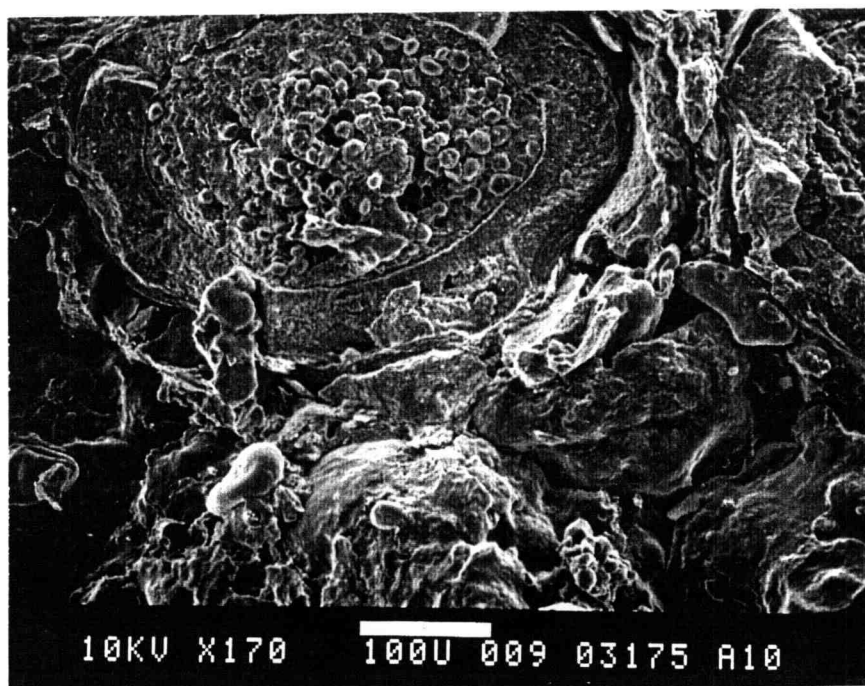
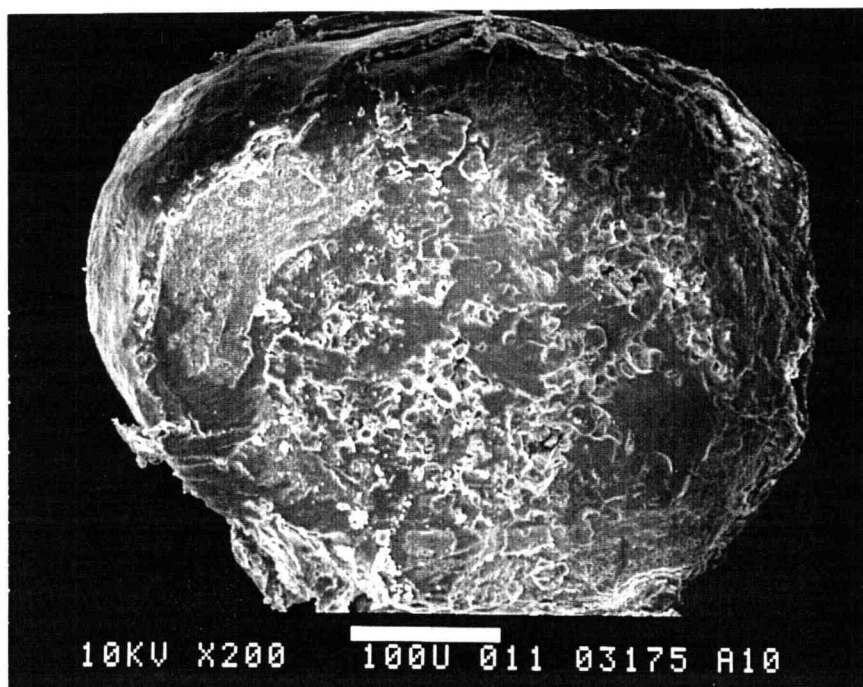
Since the 20% PEG coated formulation E compressed beads produced good release profiles, the beads were mixed with 5% Explotab (formulation F) before compaction at 200 lb.. This was done to see if the caplets would disintegrate into individual beads while still maintaining their sustained release properties. The caplets began to disintegrate within 1/2 hour and were completely disintegrated into individual beads within 2 hours; however, in 4 hours almost 80% of the drug was released. Since the caplet disintegration into individual units was still slower and an increase in drug release profile was observed upon disintegration of the caplets, a layer of cushioning excipient and a disintegrant was then applied.

#### Excipient/Disintegrant Coated Compacts:

In order to formulate a rapidly disintegrating caplet, formulation E beads were spray coated with 10% layer of Avicel PH-101 and a 5% layer of the disintegrant sodium starch glycolate (Explotab) (formulation G). Figure V.4 shows scanning electron micrographs (SEM's) of the formulation G beads before and after compression at 125 lb. pressure. It is apparent from this figure that some of the beads remain intact



V.3 Effect of pressure on drug release from formulation E (● = uncompact beads, ○ = caplet @ 300 lb., □ = caplet @ 3150 lb.); and formulation F (Δ = caplet @ 200 lb.) compressed beads.

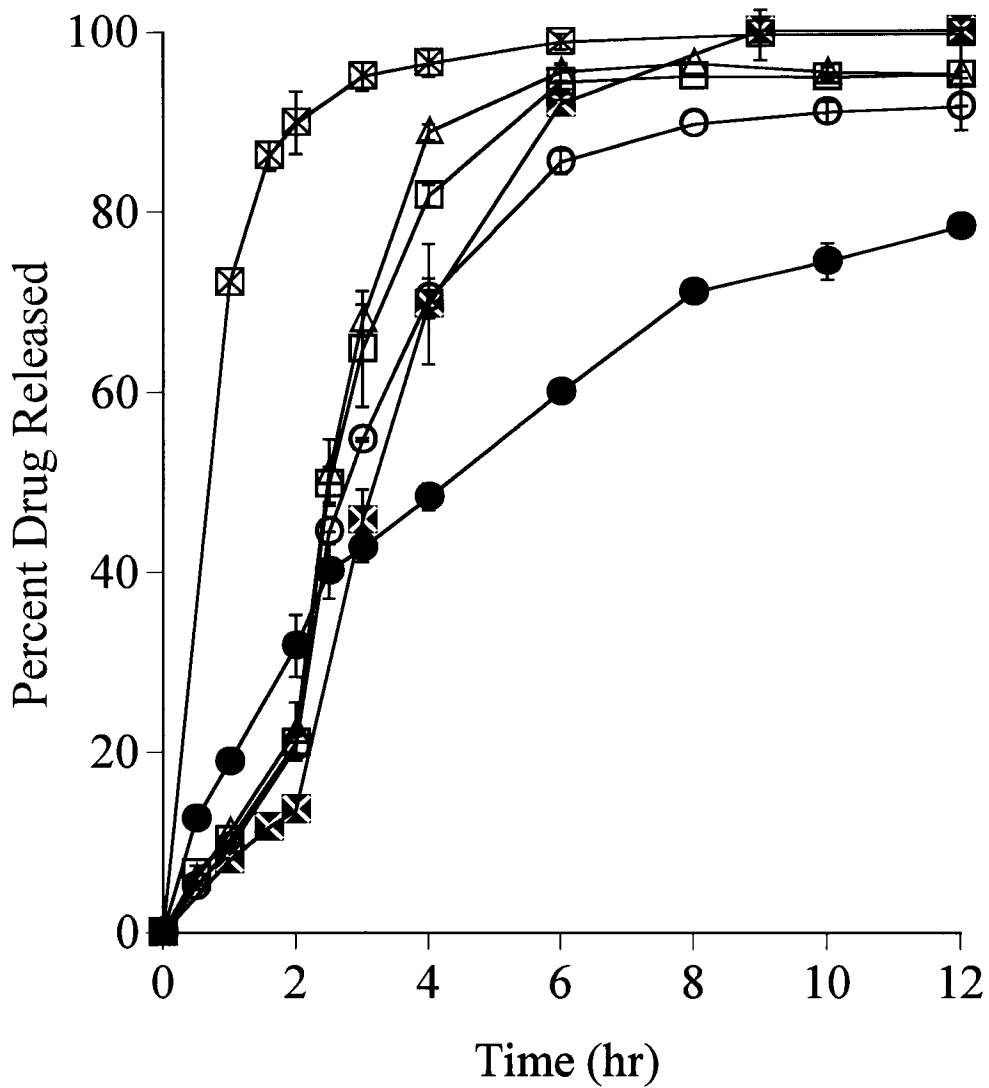


V.4 Scanning electron micrographs of formulation G - uncompact beads (A) and beads compacted at 125 lb. pressure (B).

upon compaction thereby maintaining their sustained release characteristics. Figure V.5 shows the dissolution profiles of these beads compressed at different pressures. All caplets disintegrated into individual beads at 2 hours when the simulated gastric fluid (pH  $1.4 \pm 0.1$ ) was replaced with simulated intestinal fluid (pH  $7.4 \pm 0.1$ ); this disintegration was followed by a sharp rise in drug release independent of compaction pressure. As seen from Figure V.5 that the total drug is released in 6 hours for the caplets compressed at 500 and 1000 lb.; however, at a pressure 125 lb. it takes 8 hours for the total drug to be released. As evident from the figure, higher pressures may cause more fracture to the polymer coat causing the drug to be released at a faster rate. When the same formulation (formulation G) was compressed into a tablet on a single punch press (hardness of 5 Kg), upon switching from simulated gastric to intestinal fluid the same drug release pattern is observed as with caplets made on a Carver press. Crushing these tablets resulted in more than 90% drug release in 3 hours.

#### Sealant-Effect Compacts:

Next, the 45/60 mesh drug loaded spheres were coated with a 9% w/v Aquacoat to provide a seal coat which would prevent drug loss while coating the polyethylene oxide layer. The 10% polyethylene oxide (Polyox N-3000) solution was then spray coated over the Aquacoat seal-coat followed by another 10% w/w Aquacoat layer. the polyethylene oxide (PEO) layered beads. The 10% Avicel PH-101 as a cushioning agent and an outermost layer of 5% w/w disintegrant was then applied (formulation H). The rationale for formulation H is that when these beads are compressed, the Aquacoat

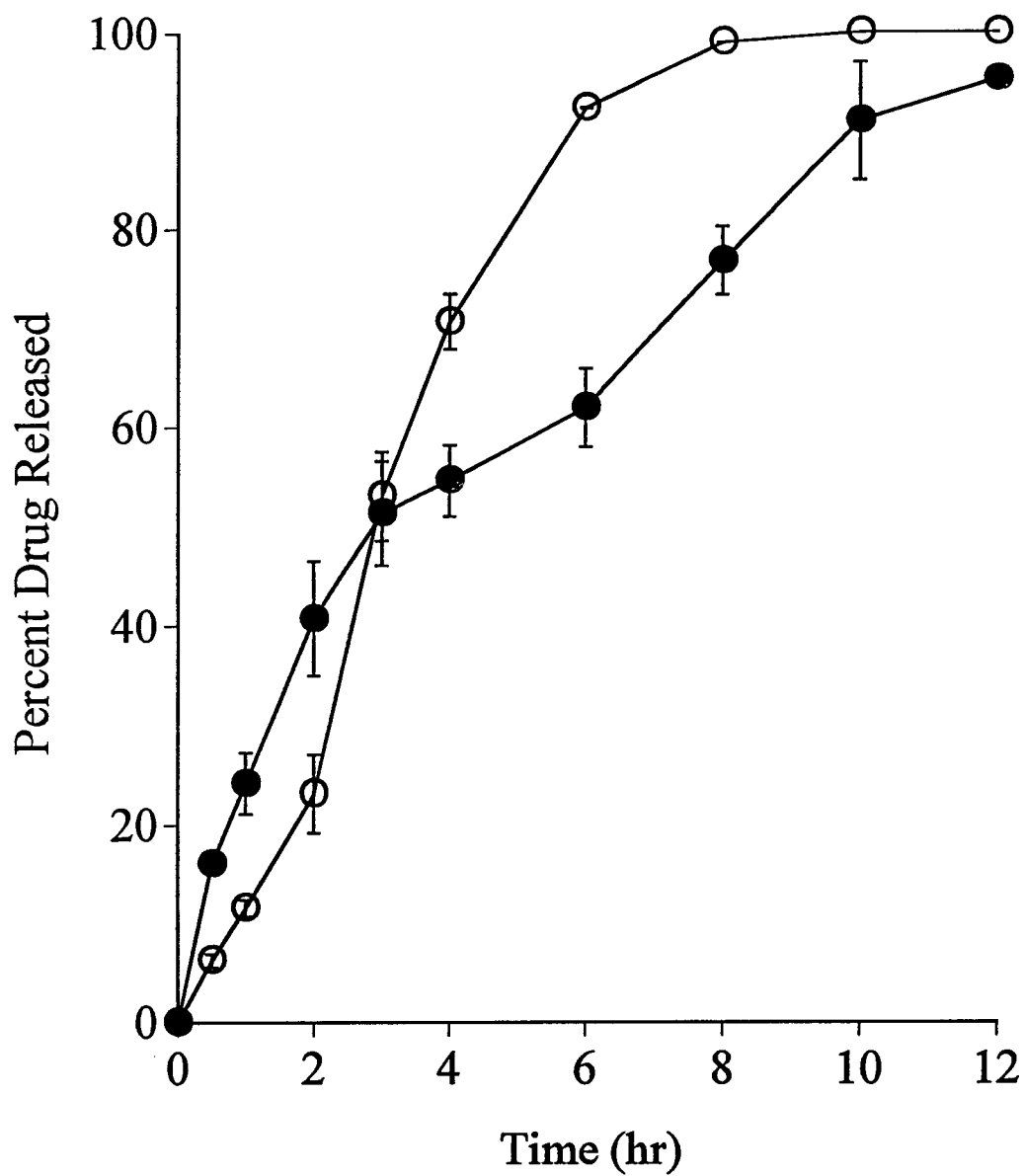


V.5 Effect of Excipient/disintegrant coating on drug release from compressed formulation beads at different compaction pressure. Uncompacted beads (●); caplets @ 125 lb. (○), 500 lb. (□), 1000 lb. (△); tablet of 5 kg hardness (⊠), crushed tablet (⊞).

and PEO layers will break or cracks due to the compaction pressure. However, as soon as these beads are hydrated in the dissolution media, the PEO will swell and block the pores or cracks in the outer layers. Avicel and Explotab will facilitate the rapid disintegration of the caplets into the original beads with sustained release properties. Figure V.6 shows the dissolution profile of spray coated PEO beads and caplets made at 1000 lb. pressure. As evident from the Figure V.6 the drug release for caplets is slower for the first 2 hours; however, after 2 hours when the dissolution medium is changed from simulated gastric to intestinal fluid an increase in the release rate is observed with total drug released in 8 hours. The caplets disintegrated completely into individual beads within 20 minutes. Spray coating PEO onto the beads is a difficult process, because the PEO solution is sticky and the beads agglomerate in the fluid-bed chamber. Talc or some anti-tackiness excipient may be added to the PEO solution to reduce tackiness and improve the coating efficiency. More work is needed to optimize PEO coating process and a seal coat of about 5% or less may be sufficient to prevent drug loss during PEO coating.

#### Triple Layer Caplets:

Next triple layered caplets with the polymer coated beads in the center layer between a top and bottom cushioning excipient layer was studied. Avicel PH-101 or polyethylene oxide were used as cushioning excipients for the two outer layers of the triple layered caplet. When Avicel was used to make triple layer caplet using different thickness polymer coats, the drug release was sustained for 24 hours (Figure V.1). Almost all

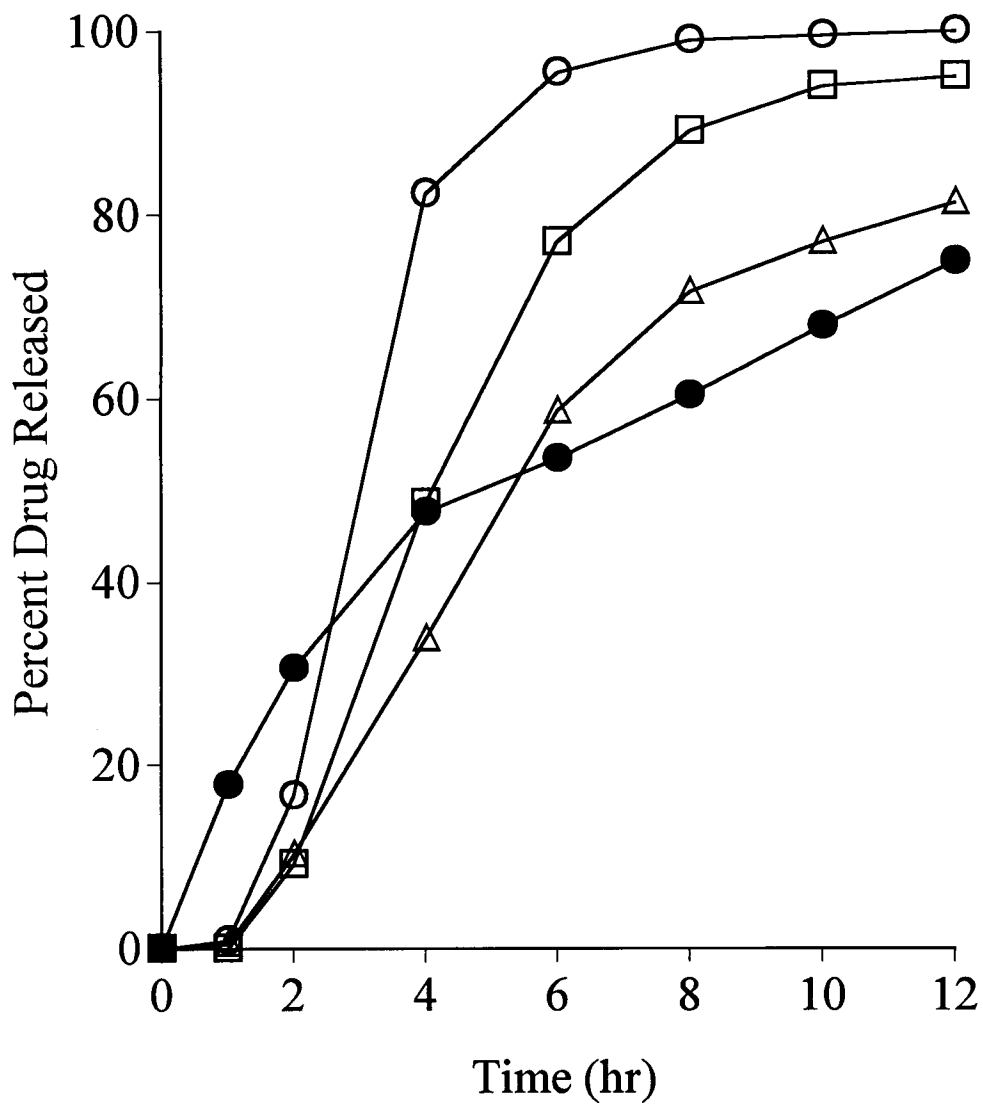


V.6 Effect of spray coated Polyox on drug release from compressed beads. ● = uncompacteds beads, ○ = caplets @ 1000 lb.

the triple layered caplets made with Avicel as the outer layers started to disintegrate immediately with the top and bottom Avicel layers falling apart. The center layer was intact for at least 4 hours, at which time it was completely or partially disintegrated into smaller chunks. Avicel was premixed with 1% magnesium stearate for lubrication prior to caplet compaction.

The triple layer caplets made with outer PEO layers produced decreased drug release with an increase in pressure (Figure V.7). The 21% w/w drug coated beads were spray coated with 6% Aquacoat, which was followed by 13% w/w drug coating and then another 6% Aquacoat layer over it (formulation I). The beads were then compressed into triple layered caplets using about 16.5% w/w PEO on the top and bottom layers. As seen from Figure V.7, there is a lag time of 1 hour before the drug starts to diffuse through the swollen PEO layers. PEO swelled to almost twice the original size forming a translucent barrier to drug release. The triple layered caplets made at 50 lb. pressure disintegrated into two relatively large chunks with about 25% of the beads separated from the translucent gel after 2 hours. This is evident from the sharp rise in the drug-release profile, with 70% drug released in 4 hours. The layers from caplets made at 100 and 250 lb. pressures fell apart after 2 hours with the bottom layer sticking to the bottom of the dissolution flask, while the remainder of the caplet with the top PEO layer still attached to the center layer swirled under the paddle. The caplets made at 500 lb. pressure; however, were intact with only part of the gel eroded away at the end of 55 hours. All PEO based triple layered caplets, except the one made at 500 lb. disintegrated into distinct individual beads. Drug release from PEO based





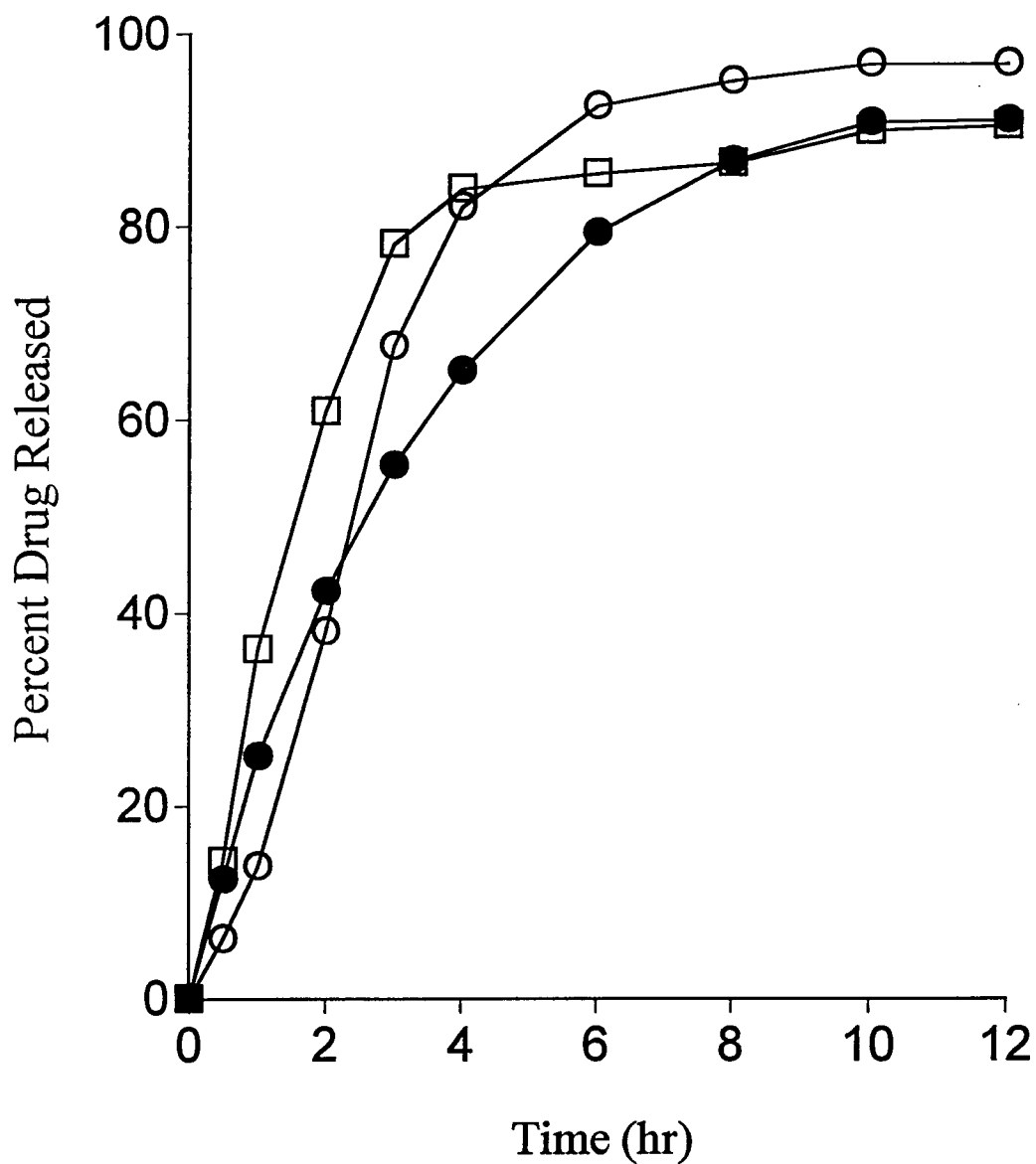
V.7 Triple layered caplets: Effect of pressure with PEO layers (33%) on drug release from compressed beads. ● = uncompacteds beads, ○ = 50 lb. □ = 250 lb., △ = 500 lb.

matrix tablets from these triple layer caplets can be characterized through swelling and diffusion of the polymer as reported by Cherng-Ju Kim (21).

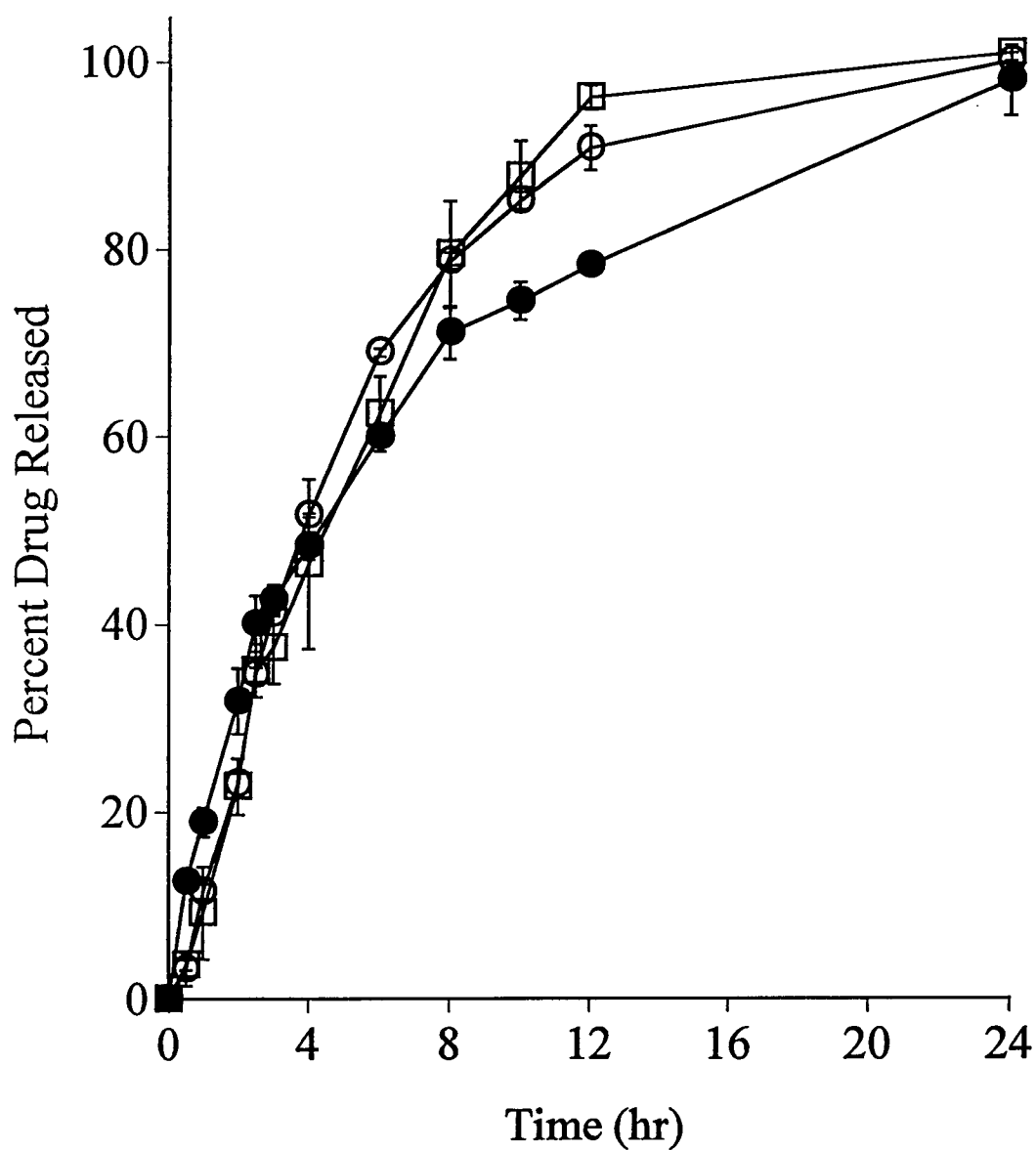
Triple layered caplets were also made with Avicel or PEO using formulation C beads. Figure V.8 shows that TLC's made with PEO release total drug in 4 hours while for Avicel based TLC's, it takes about 8 hours for the total drug to be released. The difference in drug release between the two is more prominent when the release is compared at individual time points. However, when TLC's were made using formulation D beads, there appears to be insignificant difference in drug release from the beads compressed with Avicel and PEO layers (Figure V.9).

#### Granulated Bead Compacts:

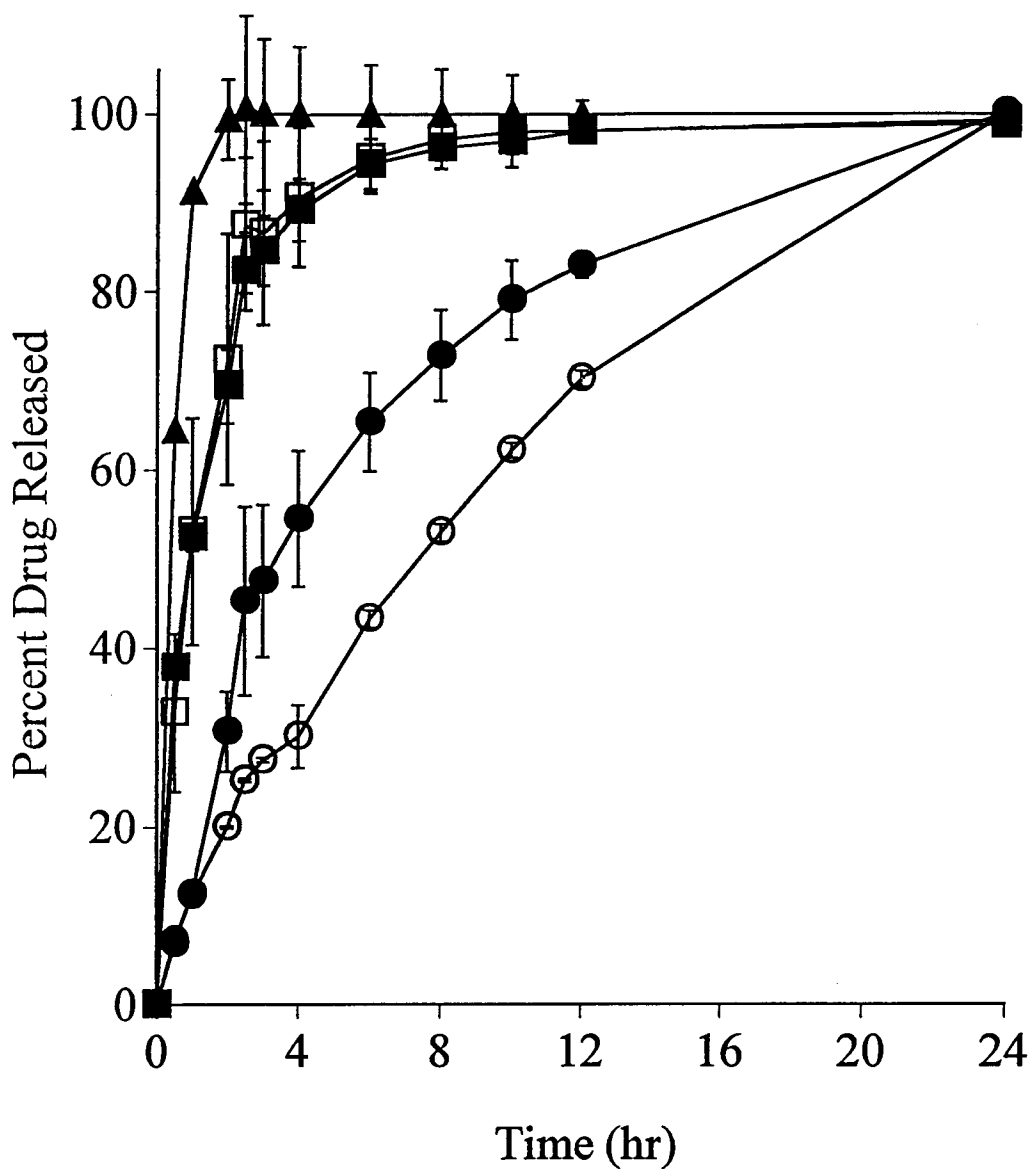
Another way to prevent the fracture of polymer coated beads and the segregation of cushioning excipients is to granulate the polymer coated beads with the cushioning agent. This way the granulating agent acts as a cushion between the beads and prevent polymers coat fracture upon compression. Avicel granules alone were also made that were mixed with the polymer coated beads before compaction for comparison of drug release with Avicel-granulated bead compacts. Figure V.10 shows the dissolution profiles of Avicel granulated formulation D bead compacts and also mixture of Avicel granules with formulation B or C beads compacted at different pressures. As can be seen from the Figure V.10, mixing Avicel granules (25/35 mesh) with formulations C or D beads did not protect the polymer coat from fracture at low pressure, total drug was released in 4 hours. Also, when caplets made with formulation



V.8 Triple layered caplets: Effect of Avicel and PEO layers on formulation C compressed beads. ● = uncompact beads, ○ = Avicel 20% @ 500 lb. □ = PEO 20% @ 500 lb.



V.9 Triple layered caplets: Effect of Avicel and PEO layers on formulation E compressed beads. ● = uncompacteds beads, ○ = Avicel 20% @ 300 lb. □ = PEO 20% @ 300 lb.



V.10 Granulated bead compacts: Effect of compression of Avicel-granulated polymer-coated beads on drug release. ● = Avicel granulated formulation E beads @ 250 lb., ○ = Avicel granulated formulation E beads @ 500 lb., ■ = Avicel granules + formulation D @ 250lb., □ = Avicel granules + formulation E @ 250lb., ▲ = Avicel granulated formulation D @ 250 lb.

C beads were granulated with Avicel, total drug was released in 2 hours. However, when formulation D beads were granulated with Avicel, only 57% drug is released in 4 hours when compacted at a low pressure of 250 lb.. The same granulation when compacted at 500 lb. pressure released only about 32% drug in 4 hours and gives a nice sustained release profile for 24 hours. In both cases of Avicel granulated beads, the caplets partially disintegrated into individual beads.

### CONCLUSIONS

Segregation of polymer coated beads in mixtures with cushioning excipients can be avoided by spray coating the cushioning excipients onto polymer coated beads.

Also, tackiness that develops between the Aquacoat coated beads during storage in containers is avoided by spray coating excipients such as Avicel leading to free flowing characteristics of the coated beads into the die during tablet compaction. It was found that the level of polymer coating, compression pressure, bead size and the type of cushioning excipient affects the drug release characteristics. Smaller size beads compress better producing better quality caplets.

Excipient/Disintegrant coating and Sealant effect compacts show promise in developing a rapidly disintegrating caplet. Triple layer caplets were not able to protect the polymer coat on beads upon compression, but produced to a sustained release non-disintegrating matrix. Granulated beads also lead to a useful non-disintegrating constant release matrix caplet.

## REFERENCES

- (1) Ragnarsson, G. , Sandberg, A., Jonsson, U. E., and Sjögren, J. Development of a new controlled release metoprolol product. *Drug. Dev. Ind. Pharm.* 13(9-11):1495-1509 (1987).
- (2) Aulton, M. E., Dyer, A. M., and Khan, K. A. The strength and compaction of millispheres: The design of a controlled release drug delivery system for ibuprofen in the form of a tablet comprising compacted polymer-coated millispheres. *Drug. Dev. Ind. Pharm.* 20(20):3069-3104 (1994).
- (3) Celik, M. and Maganti, L. Formulation and compaction of microspheres. *Drug. Dev. Ind. Pharm.* 20(20):3151-3173 (1994).
- (4) Béchard, S. R. and Leroux, J. C. Coated pelletized dosage form: Effect of compaction on drug release. *Drug. Dev. Ind. Pharm.* 18(18):1927-1944 (1992).
- (5) Chang, R.-K., and Rudnic, E. M. The effect of various polymeric coating systems on the dissolution and tableting properties of potassium chloride microcapsules. *Int. J. Pharm.* 70:261-270 (1991).
- (6) Company's monograph, Colorcon<sup>®</sup>, Surelease 0601-78 coating for chlorpheniramine maleate non-pariels compressed into tablets. West point, PA (1994).
- (7) Maganti, L. and Celik, M. Compaction studies on pellets: II. Coated pellets. *Int. J. Pharm.* 103:55-67 (1994).
- (8) Juslin, M., Turakka, L., and Puumalainen, P. *Pharm. Ind.* 42:829- (1980).
- (9) Prapaitrakul, W. and Whitworth, C. W. Compression of microcapsules I: Effect of excipients and pressure on drug release. *Drug. Dev. Ind. Pharm.* 15(12):2049-2053 (1989).
- (10) Ruiz, R., Sakr, A., and Sprockel, O. L. A study of the manufacture and in vitro dissolution of terbutaline sulfate microcapsules. *Drug. Dev. Ind. Pharm.* 16(11):1829-1842 (1990).
- (11) Sayed, H. A. M. and Price, J. C. Tablet properties and dissolution characteristics of compressed cellulose acetate butyrate microcapsules containing succinyl sulfathiazole. *Drug. Dev. Ind. Pharm.* 12(4):577-587 (1986).

- (12) Scwhartz, J. B., Nguyen, N. H., and Schnaare, R. L. Compaction studies on beads: Compression and consolidation parameters. *Drug. Dev. Ind. Pharm.* 20(20):3105-3129 (1994).
- (13) Torrado, J. J. and Augsburger, L. L. Effect of different excipients on the tableting of coated particles. *Int. J. Pharm.* 106:149-155 (1994).
- (14) McTaggart, C. M., Ganley, J. A., Sickmueller, A., and Walker, S. E. The evaluation of formulation and processing conditions of a melt granulation process. *Int. J. Pharm.* 19, 139-148 (1984).
- (15) Chemtob, C., Chaumeil, J. C., and N'Dongo, M. Tablets of metronidazole microcapsules: release characteristics. *Int. J. Pharm.* 29:83-92 (1986).
- (16) Badwan, A. A., Abumaloooh, A., Sallam, E., Abukalaf, A., and Jawan, O. A sustained release drug delivery system using calcium alginate beads. *Drug. Dev. Ind. Pharm.* 11(2&3):239-256 (1985).
- (17) Jalšenjak, I., Nixon, J. R., Senjkovic, R., and Štivic, I. Sustained-release dosage forms of microencapsulated isoniazid. *J. Pharm. Pharmacol.* 32:678-680 (1980).
- (18) Chowhan, Z. T. Segregation of Particulate Solids, Part I. *Pharm. Technol.* 19 (5), 56-70 (1995).
- (19) Chowhan, Z. T. Segregation of Particulate Solids, Part II. *Pharm. Technol.* 19 (6), 80-94 (1995).
- (20) Connie, J. W. and Hadley, H. R. Small Solid Pharmaceutical Spheres, Drug and Cosmetic Industry, 106, 38-41 (1970).
- (21) FMC manual, FMC Corporation, Nutley, NJ
- (22) Kim, C.-J. Drug release from compressed hydrophilic POLYOX-WSR tablets. *J. Pharm. Sci.* 84(3):303-306 (1995).



CHAPTER VI  
CONCLUSION

There are two major parts of this thesis, first part involves developing tablet machine instrumentation for studying the compaction characteristics of the excipients used in the pharmaceutical industry. In this section, the deformation of the Stokes B2 rotary machine was quantitatively characterized. These deformation studies were done with a cathetometer and conclusively show that the Stokes B2 tablet press undergoes elastic deformation. This deformation can be characterized with two different elastic moduli (one for the upper and one for the lower compression roller assemblies); both elastic moduli are independent of compaction phase and lower punch penetration setting. The cathetometer data was validated by the lead compact studies. Therefore, on the basis of these results, the authors recommend that, when calculating punch displacement for the Stokes B2, press deformation be accounted for by using the corrected displacement equations and the elastic constants as determined in chapter II.

The incremental work of compaction studies showed that press deformation absorbs energy during the loading phase and then releases this energy later in the compaction cycle. The rate at which the press stores and releases elastic energy depends in part upon the viscoelastic properties of the tablet. The coupling between the material properties of the tablet and press work together to change the punch-displacement profile, so that different tablet formulations, compression pressures, and operating conditions will lead to different compaction/punch-displacement profiles. On the basis of these results, if a tablet press undergoes significant deformation during compaction, the coupling between the press and tablet should be accounted for when

analyzing tablet compaction or trying to simulate the punch-displacement profile of that tablet press.

In addition to studying press deformation, the split-web die concept for die wall stress measurements was also developed as part of the instrumentation section of the thesis. This die design encloses the sensing web in a cylinder, thereby allowing the instrumented die to be mounted without modification of the die table. This design overcomes a significant problem with three-layered die transducer and thus improves DWS measurement. The optimal web thickness and strain gage position were determined using an optimal design process (ODP). The output signal for this design is linear ( $r^2 = 0.999$ ) and independent of tablet height. Based upon FEA, the authors recommend the use of the 1/8 in. sensing web and a strain gage positioned at  $\phi = 0^\circ$ , or two gages at  $\phi = \pm 30^\circ$ , for optimal signal output. This system showed no hysteresis, which indicates that there is no permanent distortion of the 1/8 in. sensing web in the range of pressures studied. The study has shown that FEA can accurately predict the performance of a transducer design, thus proving FEA to be a powerful tool for structural design optimization.

In summary, the optimal design process (ODP) and FEA employed for the design of press instrumentation has not been reported in the pharmaceutical literature previously. Because this method can produce efficient transducer designs with less cost and time, the authors believe that this method represents a significant advancement over the existing trial-and-error method of transducer design for tablet press instrumentation.

The second part of this thesis examines factors that affect of polymer coat integrity during the compaction of the sustained release polymer-coated beads. By spray coating beads with cushioning excipients the segregation that can occur when polymer coated beads are mixed with cushioning excipients can be avoided. Also, tackiness that can develop with the Aquacoat coated beads during storage is avoided by spray coated cushioning excipients such as Avicel and mannitol. This improves free flowing characteristics of the coated beads. It was found that the level of polymer coating, compression pressure, bead size and the type of cushioning excipient affects the drug release characteristics. Smaller size beads compress better producing better quality caplets even at the very low pressures of 100 lb..

Excipient/Disintegrant coating and Sealant effect compacts show promise as a rapidly disintegrating caplet with sustained release properties. Triple layer caplets were not able to protect the polymer coat on beads upon compression, but produced to a sustained release non-disintegrating matrix. Granulated beads also lead to a useful non-disintegrating constant release matrix caplet. Crushing of these caplets eliminates the sustained release characteristics of the resultant non-disintegrating matrix caplets, confirming that polymer coats were disrupted during compaction. Also, larger size beads, especially with Avicel as the outer coating layer are hard to compress into intact caplets. In such cases higher pressures (>1000 lb.) are required to make acceptable caplets.

## BIBLIOGRAPHY

Amidon, G. E., Smith, D. P., Hiestand, E. N., Rotary press utilizing a flexible die wall. *J. Pharm. Sci.* 70(6):613-617 (1981).

Aulton, M. E.; Dyer, A. M.; Khan, K., The strength and compaction of millispheres: The design of a controlled-release drug delivery system for ibuprofen in the form of a tablet comprising compacted polymer-coated millispheres. *A. Drug. Dev. Ind. Pharm.* 20(20):3069-3104 (1994).

Badwan, A. A., Abumalooch, A., Sallam, E., Abukalaf, A., and Jawan, O. A sustained release drug delivery system using calcium alginate beads. *Drug. Dev. Ind. Pharm.* 11(2&3):239-256 (1985).

Béchar, S. R.; Leroux, J. C., Coated Pelletized Dosage Form: Effect of Compaction on Drug Release *Drug. Dev. Ind. Pharm.* 18(18):1927-1944 (1992).

Celik, M. In *Multiparticulate Oral Drug Delivery*, Marcel Dekker Inc., New York, pp. 181-215 (1994).

Celik, M.; Maganti, L., Formulation and compaction of microspheres. *Drug. Dev. Ind. Pharm.* 20(20):3151-3173 (1994).

Champion, E. R. jr., Fundamentals of applied finite element analysis. In *Finite element analysis in manufacturing engineering: A pc-based approach*, McGraw-Hill Inc., New York, pp. 31-66 (1992).

Chang, R.-K.; Rudnic, E. M., The effect of various polymeric coating systems on the dissolution and tableting properties of potassium chloride microcapsules. *Int. J. Pharm.* 70:261-270 (1991).

Chemtob, C., Chaumeil, J. C., and N'Dongo, M., Tablets of metronidazole microcapsules: release characteristics. *Int. J. Pharm.* 29:83-92 (1986).

Chowhan, Z. T., Segregation of Particulate Solids, Part I. *Pharm. Technol.* 19 (5), 56-70 (1995).

Chowhan, Z. T., Segregation of Particulate Solids, Part II. *Pharm. Technol.* 19 (6), 80-94 (1995).

Cocolas, H. G. and Lordi, N. G., Axial to radial pressure transmission of tablet excipients using a novel instrumented die. *Drug. Dev. Ind. Pharm.* 19(17&18):2473-2497 (1993).

- Collins, J. A., *Failure of materials in mechanical design: analysis, prediction, prevention*, John Wiley & Sons, (1993).
- Colorcon<sup>®</sup> Bulletin, Surelease<sup>®</sup> 0601-78 coating for chlorpheniramine maleate non-pareils compressed into tablets., West point, PA. (1994).
- Connie, J. W. and Hadley, H. R., Small Solid Pharmaceutical Spheres, *Drug and Cosmetic Industry*, 106, 38-41 (1970).
- Conte, U., Colombo, P., La Manna, A., and Caramella, C., La mesure de la force radiale a l'aide d'une matrice divisee: Applications aux problemes pharmaceutiques. *II Farmaco - Ed. Pr.* 32(11):551-559 (1977).
- Cook, R. D., *Concepts and applications of finite element analysis*, 2nd edition, John Wiley & sons, (1981).
- COSMOS/M, *User Guide*, SRAC, (1990).
- Dally, J. W. and Riley, W. F., Strain measurement methods and related instrumentation. In *Experimental stress analysis*, 3rd edition, McGraw-Hill Inc., New York, p 184 (1991).
- Devore, J.; Peck, R., *Statistics, the Exploration and Analysis of Data*; West Publishing: St. Paul, 474-477 (1986).
- Errors Due to Wheatstone Bridge Non-Linearity*, TN-507, Measurements Group Inc., Raleigh, USA, (1982).
- Fenner, R. T., *Engineering elasticity*, Ellis Horwood, Chichester, England, (1986).
- FMC manual, FMC Corporation, Nutley, NJ
- Garratt, J. D., Survey of displacement transducers below 50 mm. *J. Phys. E: Sci. Instrum.*, 12, 563-573 (1979).
- Ho, A.; Barker, J. F.; Spence, J.; Jones, T. M., A comparison of three methods of mounting a linear variable displacement transducer on an instrumented tablet machine. *J. Pharm. Pharmacol.*, 31, 471-472 (1979).
- Hoag, S. W.; Rippie, E. G., Thermodynamic Analysis of Energy Dissipation by Pharmaceutical Tablets During Stress Unloading. *J. Pharm. Sci.*, 83, 903-908 (1994).

- Hoblitzell, J. R.; Rhodes, C. T., Determination of a relationship between force-displacement and force-time compression curves. *Drug Dev. Ind. Pharm.*, 16, 201-229 (1990).
- Holman, L. E.; Marshall, K., Calibration of a Compaction Simulator for the Measurement of Tablet Thickness During Compression. *Pharm. Res.*, 10, 816-822 (1993).
- Hölzer, A. W. and Sjögren, J., Instrumentation and calibration of a single punch press for measuring the radial force during tableting. *Int. J. Pharm.* 3:221-230 (1979).
- Hossain, M, Ph. D. Thesis, Oregon State University (1992).
- Huckle, P. D. and Summers, M. P., The Effects of Strain Gauge Size and Configuration on Radial Stress Measurement During Tableting. *J. Pharm. Pharmacol.*, 36, Suppl. 6P, (1984).
- Huckle, P. D. and Summers, M. P., The use of strain gauges for radial stress measurement during tableting. *J. Pharm. Pharmacol.* 37:722-725 (1985).
- Jalšenjak, I., Nixon, J. R., Senjkovic, R., and Štivic, I. Sustained-release dosage forms of microencapsulated isoniazid. *J. Pharm. Pharmacol.* 32:678-680 (1980).
- Juslin, M. J.; Paronen, T. P., On the accuracy of displacement measurements by instrumented single-punch machines. *J. Pharm. Pharmacol.*, 32, 796-798 (1980).
- Juslin, M., Turakka, L., and Puumalainen, P., *Pharm. Ind.* 42:829- (1980).
- Kanaya, Y., Ando, T., and Asahina, K., A technique for measurements of die wall pressure during tablet compression. *Yakuzaigaku.* 39(1):26-33 (1979).
- Kennerley, J. W.; Newton, J. M.; Stanley, P., Tablet thickness variation and machine stiffness. *Acta Pharm. Suecica*, 18, 106-107 (1981).
- Kim, C.-J., Drug release from compressed hydrophilic POLYOX-WSR tablets. *J. Pharm. Sci.* 84(3):303-306 (1995).
- Krycer, I., Pope, D. G., and Hersey, J. A., The interpretation of powder compaction data - a critical review. *Drug. Dev. Ind. Pharm.* 8(3):307-342 (1982).
- Lammens, R. F.; Polderman, J.; deBlaey, C. J., Evaluation of force-displacement measurements during powder compaction: Precision and accuracy of force measurements. *Int. J. Pharm. Technol. Prod. Manuf.*, 1, 26-35 (1979).

Lammens, R. F.; Polderman, J.; deBlaney, C. J., Armstrong, N. A., Evaluation of force-displacement measurements during powder compaction: Precision and accuracy of powder height and punch displacement measurements. *Int. J. Pharm. Technol. Prod. Manuf.*, 1, 26-35 (1980).

Leigh, S., Carless, J. E., and Burt, B. W., Compression characteristics of some pharmaceutical materials" *J. Pharm. Sci.* 56: 888-892 (1967).

Long, W. M., Die Design and Related Questions in Powder Compaction. In *Special Ceramics*, Academic Press, New York, pp. 327-340 (1962).

Long, W. M., Radial Pressures in Powder Compaction. *J Powder Metall.* 6:73-86(1960).

Maganti, L.; Celik, M., Compaction studies on pellets: II. Coated pellets. *Int. J. Pharm.* 103:55-67 (1994).

McTaggart, C. M., Ganley, J. A., Sickmueller, A., and Walker, S. E., The evaluation of formulation and processing conditions of a melt granulation process. *Int. J. Pharm.* 19, 139-148 (1984).

Measurements Group, Inc., *Strain Gage Based Transducers*, Measurements Group, Inc. Raleigh, NC, (1988).

Morehead, W. T. and Rippie, E. G., Timing Relationships among Maxima of Punch and Die-wall Stress and Punch Displacement during Compaction of Viscoelastic Solids. *J. Pharm. Sci.*, 79, 1020-1022 (1990).

Muller, V. F.; Schierstedt, D. *Pharm. Ind.*, 44, 834-837 (1982).

Nelson, E., Naqvi, S. M., Busse, L.W., and Higuchi, T. The Physics of Tablet Compression IV. Relationship of Ejection, and Upper and Lower Punch Forces during Comprssional Process: Application of Measurements to Comparison of Tablet Lubricants. *J. Am. Pharm. Assn.*, 43, 596-602, (1954).

Nelson, E., The physics of tablet compression VIII - Some preliminary measurements of die wall pressure during tablet compression. *J. Am. Pharm. Assn. Sci. Ed.* 44(8):494-497 (1955).

Oates, R. J.; Mitchell, A. G., Calculation of punch displacement and work of powder compaction on a rotary tablet press. *J. Pharm. Pharmacol.*, 41, 517-523 (1989).

Obiorah, B. A. and Shotton, E., The effect of waxes, hydrolyzed gelatin and moisture on the compression characteristics of paracetamol and phenacetin. *J. Pharm. Pharmacol.* 28:629-632 (1976).



- Prapaitrakul, W. and Whitworth, C. W., Compression of microcapsules I: Effect of excipients and pressure on drug release. *Drug. Dev. Ind. Pharm.* 15(12):2049-2053 (1989).
- Ragnarsson, G. , Sandberg, A., Jonsson, U. E., and Sjögren, J., Development of a new controlled release metoprolol product. *Drug. Dev. Ind. Pharm.* 13(9-11):1495-1509 (1987).
- Rao, S. S., *The finite element method in engineering*, Pergamon Press, (1982).
- Ridgway, K. and Rosser, P. H., The application of photoelastic techniques to a rotary tableting machine. *J. Pharm. Pharmacol.* 23:202S-209S (1971).
- Rippie, E. G.; Danielson, D. W., Viscoelastic stress/strain behaviour of pharmaceutical tablets: Analysis during unloading and postcompression periods. *J. Pharm. Sci.*, 70, 476-482 (1981).
- Ruiz, R., Sakr, A., and Sprockel, O. L., A study of the manufacture and in vitro dissolution of terbutaline sulfate microcapsules. *Drug. Dev. Ind. Pharm.* 16(11):1829-1842 (1990).
- Salpekar, A. M., and Augsburger, L. L., Magnesium Lauryl Sulfate in Tableting: Effect on Ejection Force and Compressibility. *J. Pharm. Sci.*, 63, 289-293, (1974).
- Sayed, H. A. M.; Price, J.C., Tablet properties and dissolution characteristics of compressed cellulose acetate butyrate microcapsules containing succinyl sulfathiazole. *Drug. Dev. Ind. Pharm.* 12(4):577-587 (1986).
- Scwhartz, J. B., Nguyen, N. H., and Schnaare, R. L., Compaction studies on beads: Compression and consolidation parameters. *Drug. Dev. Ind. Pharm.* 20(20):3105-3129 (1994).
- Shotton, E. and Obiorah, B. A., The effect of particle shape and crystal habit on properties of sodium chloride. *J. Pharm. Pharmacol.* 25 Suppl.:37-43 (1973).
- Strickland, W.A. Jr., Higuchi, T., and Busse, L.W., The Physics of Tablet Compression X. Mechanism of Action and Evaluation of Tablet Lubricants. *J. Am. Pharm. Assn.*, 49, 35-40, (1960).
- Timoshenko, S.P. and Goodier, J.N., *Theory of Elasticity*, 3rd edition, McGraw-Hill Inc., New York, (1970).
- Torrado, J. J. and Augsburger, L. L., Effect of different excipients on the tableting of coated particles. *Int. J. Pharm.* 106:149-155 (1994).

Ugural, A. C. and Fenster, S. K., *Advanced Strength and Applied Elasticity*, Elsevier, (1987).

Ullman, D. G., *The Mechanical Design Process*, McGraw-Hill, New York, (1992).

Walter, J. T. and Augsburg, L., A computerized force/displacement instrumented system for a rotary press. *Pharm. Technol.*, 10, (2), 26-34 (1986).

Watt, P. R., *Tablet Machine Instrumentation in Pharmaceutics: Principles and Practice*, Ellis Horwood Limited, (1988).

Windheuser, J., Misra, J., Eriksen, S. T., Higuchi. Physics of tablet compression XIII - Development of die-wall pressure during compression of various materials. *J. Am. Pharm. Assn. Sci.* 52(8):767-772 (1963).

Window, A. L., *Strain Gauge Technology*, Elsevier Science Publishers Ltd., (1992).

Yeh, C. T., Altaf, S. A., and Hoag, S. W., Force transducer design for die wall stress measurement during tablet compaction. I: General theory of design optimization using traditional stress analysis and finite element analysis. *Pharm. Res.* Submitted with part II (January, 1996).

**APPENDICES**

**APPENDIX A**

**SUMMARIZED TABLES FOR DATA ON DEFORMATION OF STOKES B2  
ROTARY TABLET PRESS AT DIFFERENT COMPACTION PHASES AND  
PUNCH PENETRATION SETTINGS**

Table A.1 Punch Displacement Measurements at the Loading Phase with Lower Punch Penetration setting of 6.99 mm for the Lower and Upper Punch of a Stokes B2 Rotary Tablet Machine

Pressure (MPa)	Lower Punch (cm)	Upper Punch (cm)	STATISTICS				
				$r^2$	Slope	DF	F
<u>Run 1</u>							
61	85.7030±0.0000	95.6670±0.0000	k(lp)	0.9917	-0.00015	3	360.0126
103	85.6950±0.0000	95.6723±0.0006	k(up)	0.9772	7.23E-05	3	128.2661
150	85.6880±0.0000	95.6743±0.0006					
199	85.6797±0.0006	95.6777±0.0006					
252	85.6740±0.0010	95.6817±0.0006					
<u>Run 2</u>							
65	85.7053±0.0006	95.6670±0.0000	k(lp)	0.9940	-0.00014	3	497.0025
108	85.6987±0.0006	95.6710±0.0000	k(up)	0.9983	9.51E-05	3	1753.179 0
157	85.6920±0.0000	95.6760±0.0000					
200	85.6877±0.0006	95.6803±0.0006					
257	85.6777±0.0006	95.6850±0.0000					
<u>Run 3</u>							
63	85.6990±0.0000	95.6657±0.0006	k(lp)	0.9889	-0.00013	2	178.2214
105	85.6967±0.0006	95.6717±0.0006	k(up)	0.9971	7.73E-05	2	682.3617
156	85.6920±0.0000	95.6750±0.0000					
203	85.6853±0.0006	95.6790±0.0010					
253	85.6780±0.0000	95.6830±0.0000					

Table A.2 Punch Displacement Measurements at the Dwell Phase with Lower Punch Penetration setting of 6.99 mm for the Lower and Upper Punch of a Stokes B2 Rotary Tablet Machine

Pressure (MPa)	Lower Punch (cm)	Upper Punch (cm)	STATISTICS				
			$r^2$	Slope	DF	F	
<u>Run 1</u>							
63	86.1913±0.0006	95.6543±0.0006	k(lp)	0.9654	-0.00011	2	55.7882
102	86.1873±0.0012	95.6583±0.0006	k(up)	0.9828	8.38E-05	2	114.5965
152	86.1790±0.0010	95.6610±0.0000					
204	86.1760±0.0000	95.6667±0.0006					
252	86.1743±0.0006	95.6700±0.0000					
<u>Run 2</u>							
66	85.7470±0.0000	95.6777±0.0006	k(lp)	0.9923	-0.00011	3	388.0537
102	85.7423±0.0006	95.6800±0.0000	k(up)	0.9934	6.97E-05	3	448.5635
161	85.7350±0.0000	95.6833±0.0006					
198	85.7320±0.0000	95.6870±0.0000					
254	85.7267±0.0012	95.6907±0.0006					
<u>Run 3</u>							
65	84.9667±0.0006	95.6500±0.0000	k(lp)	0.9779	-0.00015	2	88.2985
103	84.9610±0.0000	95.6533±0.0006	k(up)	0.9964	7.17E-05	2	559.7102
155	84.9557±0.0012	95.6567±0.0006					
202	84.9457±0.0006	95.6600±0.0000					
245	84.9270±0.0000	95.6650±0.0000					

Table A.3 Punch Displacement Measurements at the Unloading Phase with Lower Punch Penetration setting of 6.99 mm for the Lower and Upper Punch of a Stokes B2 Rotary Tablet Machine

Pressure (MPa)	Lower Punch (cm)	Upper Punch (cm)		STATISTICS			
				$r^2$	Slope	DF	F
<u>Run 1</u>							
61	84.9300±0.0010	95.6373±0.0006	k(lp)	0.9937	-0.00014	3	475.5132
102	84.9220±0.0000	95.6400±0.0010	k(up)	0.9944	8.86E-05	3	535.8151
151	84.9160±0.0000	95.6450±0.0000					
204	84.9093±0.0006	95.6490±0.0000					
249	84.9027±0.0006	95.6540±0.0000					
<u>Run 2</u>							
60	84.9310±0.0000	95.6370±0.0000	k(lp)	0.9894	-0.00014	2	186.3840
101	84.9223±0.0006	95.6413±0.0006	k(up)	0.9494	0.000101	2	37.5296
152	84.9173±0.0006	95.6493±0.0006					
201	84.9093±0.0006	95.6540±0.0000					
255	84.9010±0.0000	95.6570±0.0017					
<u>Run 3</u>							
63	84.9297±0.0012	95.6373±0.0006	k(lp)	0.9960	-0.00015	3	743.4672
103	84.9220±0.0000	95.6423±0.0006	k(up)	0.9852	9.31E-05	3	199.3205
154	84.9160±0.0000	95.6460±0.0000					
201	84.9080±0.0000	95.6493±0.0006					
252	84.9010±0.0000	95.6560±0.0000					

Table A.4 Punch Displacement Measurements at the Loading Phase with Lower Punch Penetration setting of 11.05 mm for the Lower and Upper Punch of a Stokes B2 Rotary Tablet Machine

Pressure (MPa)	Lower Punch (cm)	Upper Punch (cm)	STATISTICS				
			$r^2$	Slope	DF	F	
<u>Run 1</u>							
55	85.3470±0.0000	95.6470±0.0000	k(lp)	0.9935	-0.00012	2	306.0791
104	85.3410±0.0000	95.6533±0.0006	k(up)	0.9965	7.74E-05	2	566.7750
156	85.3360±0.0000	95.6573±0.0006					
205	85.3287±0.0006	95.6617±0.0006					
257	85.3230±0.0000	95.6650±0.0000					
<u>Run 2</u>							
56	85.3443±0.0006	95.6437±0.0006	k(lp)	0.9953	-0.00012	2	425.1869
108	85.3380±0.0000	95.6490±0.0000	k(up)	0.9953	8.11E-05	2	425.1869
147	85.3320±0.0000	95.6530±0.0000					
203	85.3260±0.0000	95.6570±0.0000					
253	85.3200±0.0000	95.6610±0.0000					
<u>Run 3</u>							
56	85.3470±0.0000	95.6540±0.0000	k(lp)	0.9846	-0.00015	2	127.7480
103	85.3400±0.0010	95.6570±0.0000	k(up)	0.9840	0.000102	2	122.6625
146	85.3310±0.0000	95.6630±0.0000					
202	85.3250±0.0000	95.6683±0.0006					
242	85.2827±0.0006	95.6710±0.0000					



Table A.5 Punch Displacement Measurements at the Dwell Phase with Lower Punch Penetration setting of 11.05 mm for the Lower and Upper Punch of a Stokes B2 Rotary Tablet Machine

Pressure (MPa)	Lower Punch (cm)	Upper Punch (cm)		STATISTICS			
				$r^2$	Slope	DF	F
<u>Run 1</u>							
60	85.3560±0.0000	95.6360±0.0010	k(lp)	0.9947	-0.00015	2	375.7603
101	85.3510±0.0000	95.6407±0.0012	k(up)	0.9877	8.99E-05	2	160.1786
148	85.3443±0.0006	95.6450±0.0000					
197	85.3360±0.0000	95.6483±0.0006					
249	85.3070±0.0010	95.6520±0.0000					
<u>Run 2</u>							
57	85.3560±0.0000	95.6377±0.0006	k(lp)	0.9934	-0.00014	2	300.5070
102	85.3487±0.0006	95.6393±0.0006	k(up)	0.9775	6.69E-05	2	86.6968
155	85.3430±0.0000	95.6433±0.0006					
199	85.3360±0.0000	95.6470±0.0000					
246	85.3113±0.0040	95.6510±0.0000					
<u>Run 3</u>							
62	85.3550±0.0000	95.6337±0.0006	k(lp)	0.9983	-0.00015	2	1192.0609
103	85.3487±0.0012	95.6380±0.0000	k(up)	0.9828	7.49E-05	2	114.4100
152	85.3423±0.0006	95.6413±0.0006					
202	85.3343±0.0006	95.6443±0.0006					
250	85.3113±0.0006	95.6473±0.0006					

Table A.6 Punch Displacement Measurements at the Unloading Phase with Lower Punch Penetration setting of 11.05 mm for the Lower and Upper Punch of a Stokes B2 Rotary Tablet Machine

Pressure (MPa)	Lower Punch (cm)	Upper Punch (cm)	STATISTICS				
				$r^2$	Slope	DF	F
<u>Run 1</u>							
54	85.3360±0.0010	95.6400±0.0000	k(lp)	0.9663	-0.00014	2	57.3680
103	85.3250±0.0000	95.6417±0.0006	k(up)	0.9711	9.52E-05	2	67.1215
152	85.3143±0.0006	95.6450±0.0000					
204	85.3080±0.0010	95.6493±0.0006					
251	85.3033±0.0006	95.6560±0.0000					
<u>Run 2</u>							
57	85.3277±0.0006	95.6287±0.0006	k(lp)	0.9886	-0.00014	2	173.2794
104	85.3220±0.0000	95.6343±0.0006	k(up)	0.9931	7.1E-05	2	289.9534
150	85.3140±0.0000	95.6380±0.0000					
204	85.3060±0.0000	95.6410±0.0000					
250	85.3013±0.0006	95.6450±0.0000					
<u>Run 3</u>							
55	85.3330±0.0000	95.6400±0.0000	k(lp)	0.9909	-0.00016	2	218.3577
103	85.3243±0.0006	95.6447±0.0006	k(up)	0.9759	9.43E-05	2	80.8665
151	85.3147±0.0006	95.6470±0.0000					
202	85.3080±0.0000	95.6533±0.0006					
250	85.3010±0.0000	95.6580±0.0010					

Table A.7 Punch Displacement Measurements at the Loading Phase with Lower Punch Penetration setting of 14.06 mm for the Lower and Upper Punch of a Stokes B2 Rotary Tablet Machine

Pressure (MPa)	Lower Punch (cm)	Upper Punch (cm)		STATISTICS			
				$r^2$	Slope	DF	F
<u>Run 1</u>							
57	85.645±0.0000	95.644±0.0000	k(lp)	0.9983	-0.00015	2	1164.474
101	85.640±0.0000	95.648±0.0000	k(up)	0.9903	8.03E-05	2	205.1351
150	85.633±0.0006	95.653±0.0000					
201	85.626±0.0000	95.656±0.0000					
250	85.618±0.0000	95.660±0.0006					
<u>Run 2</u>							
59	65.990±0.0006	76.160±0.0006	k(lp)	0.9904	-0.00016	2	205.8876
104	65.981±0.0006	76.163±0.0006	k(up)	0.9675	8.34E-05	2	59.46465
152	65.975±0.0006	76.166±0.0006					
199	65.968±0.0006	76.172±0.0021					
249	65.957±0.0000	76.174±0.0006					
<u>Run 3</u>							
56	65.990±0.0006	76.158±0.0000	k(lp)	0.9711	-0.00014	3	100.7546
105	65.982±0.0000	76.163±0.0006	k(up)	0.9991	0.000107	3	3234.538
157	65.976±0.0012	76.168±0.0012					
204	65.972±0.0000	76.174±0.0010					
249	65.961±0.0006	76.179±0.0012					

Table A.8 Punch Displacement Measurements at Dwell Phase with Lower Punch Penetration setting of 14.06 mm for the Lower and Upper Punch of a Stokes B2 Rotary Tablet Machine

Pressure (MPa)	Lower Punch (cm)	Upper Punch (cm)		STATISTICS			
				$r^2$	Slope	DF	F
<u>Run 1</u>							
63	66.041±0.0006	76.170±0.0000	k (lp)	0.9852	-0.00012	3	199.0664
109	66.036±0.0006	76.174±0.0000	k (up)	0.9460	8.36E-05	3	52.4617
154	66.029±0.0006	76.179±0.0010					
198	66.027±0.0010	76.184±0.0050					
255	66.018±0.0000	76.185±0.0000					
<u>Run 2</u>							
66	85.517±0.0015	95.643±0.0021	k (lp)	0.9954	-0.00015	2	434.0432
105	85.511±0.0021	95.645±0.0021	k (up)	0.9229	8.18E-05	2	23.9290
155	85.503±0.0010	95.648±0.0020					
199	85.497±0.0006	95.655±0.0006					
255	85.494±0.0010	95.656±0.0010					
<u>Run 3</u>							
59	85.656±0.0006	95.631±0.0006	k(lp)	0.9964	-0.00012	3	828.0777
99	85.652±0.0000	95.636±0.0006	k(up)	0.9847	7.63E-05	3	192.6949
152	85.644±0.0006	95.640±0.0000					
200	85.639±0.0006	95.643±0.0000					
236	85.635±0.0000	95.645±0.0000					

Table A.9 Punch Displacement Measurements at the Unloading Phase with Lower Punch Penetration setting of 14.06 mm for the Lower and Upper Punch of a Stokes B2 Rotary Tablet Machine

Pressure (MPa)	Lower Punch (cm)	Upper Punch (cm)		STATISTICS			
				r <sup>2</sup>	Slope	DF	F
<u>Run 1</u>							
59	66.0080±0.0000	76.1467±0.0006	k(lp)	0.9923	-0.00013	3	384.7188
102	66.0033±0.0006	76.1503±0.0015	k(up)	0.9858	9.05E-05	3	208.1443
158	65.9933±0.0006	76.1573±0.0006					
202	65.9890±0.0000	76.1593±0.0006					
251	65.9827±0.0012	76.1640±0.0020					
<u>Run 2</u>							
63	66.0103±0.0023	76.1457±0.0006	k(lp)	0.9929	-0.00016	3	421.3933
103	66.0023±0.0006	76.1530±0.0000	k(up)	0.9214	8.42E-05	3	35.1845
153	65.9937±0.0006	76.1547±0.0006					
205	65.9870±0.0000	76.1570±0.0000					
251	65.9803±0.0015	76.1640±0.0017					
<u>Run 3</u>							
61	66.0033±0.0015	76.1417±0.0015	k(lp)	0.9875	-0.00014	3	236.9661
104	65.9953±0.0006	76.1463±0.0006	k(up)	0.9840	8.4E-05	3	184.8919
153	65.9900±0.0000	76.1487±0.0006					
201	65.9850±0.0010	76.1547±0.0006					
256	65.9750±0.0000	76.1580±0.0000					

**APPENDIX B****FORCE TRANSDUCER DESIGN FOR DIE WALL STRESS MEASUREMENT  
DURING TABLET COMPACTION: I. GENERAL THEORY OF DESIGN  
OPTIMIZATION USING TRADITIONAL STRESS ANALYSIS AND FINITE  
ELEMENT ANALYSIS**

**Chuntien Yeh, Syed A. Altaf and Stephen W. Hoag**

## ABSTRACT

Traditionally, transducers for tablet press instrumentation have been designed by a trial-and-error. The goal of this paper is to take advantage of recent developments in computer aided engineering stress analysis and propose procedures by which transducers for tablet press instrumentation can be designed and optimized in a more systematic manner. In this study, an optimal design process (ODP) which can significantly increase the accuracy and efficiency of a force transducer will be used to design tablet press instrumentation for die-wall stress measurement. This design-by-analysis approach uses engineering stress analysis to simulate the performance of a transducer. With this transducer performance information the designer can study the effect of in-service loading upon the design configuration and strain gage arrangement without building a prototype. Using this approach the dimensions and associated strain gage arrangements can easily be changed and then optimized to obtain the best initial design configuration. This paper examines the geometric optimization of the cylindrical and segmented die designs. Discussion includes the selection of optimal die wall thickness, segment cutting angle, strain gage placement, Wheatstone bridge configuration, and the influence of tablet height and position within the die on signal output. The stress analyses were done by closed-form analytical solution, and a 3D finite element analysis (FEA) software package.

**KEY WORDS:** die wall stress measurement; finite element analysis FEA; segmented die; force transducer optimization.

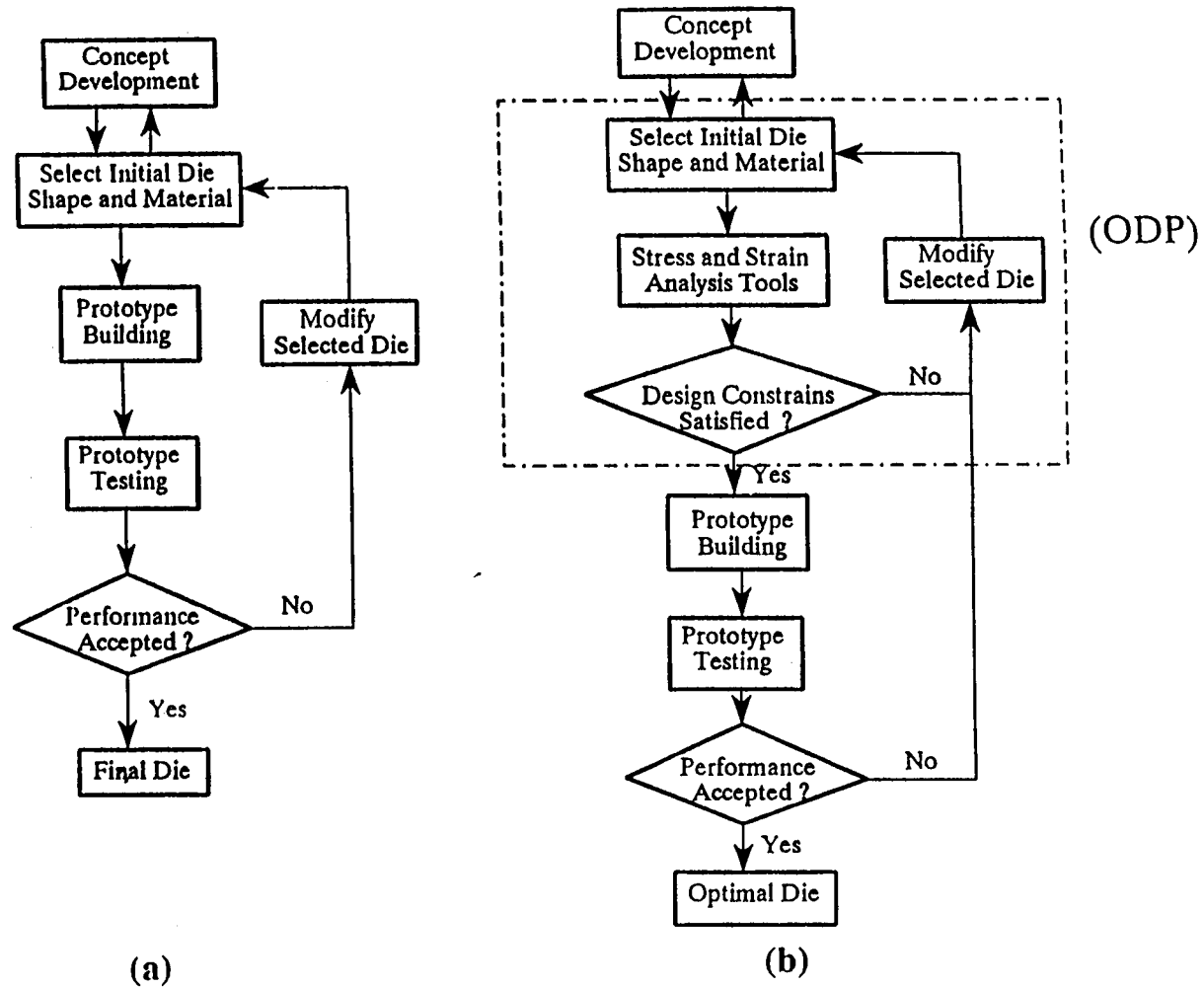
## INTRODUCTION

The radial transmission of the applied axial punch force to the die wall is very important to the understanding of tablet compaction. Over the years, many different types of transducers have been developed for the measurement of die wall stress. A comprehensive review of these measurement systems is given by Watt (1). Because it is the design geometry and associated strain gage arrangement which determines the performance characteristics of a transducer, there have been many different designs and special gage configurations developed for the optimization of die wall stress measurement. At present, various modifications of the segmented die originally developed by Windheuser et al. (2) are most commonly used to measure die wall stress.

These current segmented die designs have resulted from a great deal of experimental trial-and-error. Figure B.1a divides the current trial-and-error design process into four distinct phases: concept development, shape and materials selection, prototype building, and prototype testing. In this process, a prototype is built and tested. If it doesn't deliver the desired performance, the design is modified and the cycle of prototype building and testing is repeated until the design has the desired performance characteristics. Drawbacks of this traditional design process are the time and expense associated with prototype building and physical testing. As a result, the number of design concepts that can be developed is limited.

To overcome the limitations associated with the trial-and-error method, this research will use an optimal design process (ODP), which is based upon a design-by-





B.1 Traditional die design procedure (a) and the proposed optimal die design procedure ODP (b).

analysis approach. The closed-loop algorithm for the ODP is shown in Figure B.1b. The difference between the trial-and-error method and the ODP is that, instead of building and testing a prototype, engineering-stress analysis is used to simulate the performance characteristics of a transducer design. With this information the initial design decisions can be made without building a prototype, and the cycle of design modification and testing can be done with fewer prototypes and a wider range of test conditions. Thus, important design constraints such as material failure, strain gage failure, and bridge output signal level can be simultaneously studied and optimized, ensuring the best performance possible from a particular design concept.

Except for the simplest geometry's, this design-by-analysis approach is not practical without the use of high-performance computers. However, with the commercialization of low-cost user-friendly software, engineering stress analysis can now be performed without the extensive training and theoretical background once required, and with the ready availability of high-performance personal computers the ODP is now feasible for most researchers practiced in the art of tablet compaction. At present, tablet press instrumentation is primarily designed by trial-and-error, but with all of these recent advances in engineering stress analysis the authors feel that the design-by-analysis approach is now feasible for pharmaceutical researchers and merits further investigation. Consequently, the goal of this paper will be to show how the design-by-analysis approach can be used to improve the transducer design process for press instrumentation. In addition, because transducers for die-wall stress

measurement can produce ambiguous results, the improved theoretical understanding gained through the design-by-analysis approach will help researchers better interpret data and better understand the data's limitations.

To illustrate how engineering stress analysis can be adapted to the design of tablet press instrumentation: 1) First, the general principles needed for a design-by-analysis approach will be discussed; 2) then the geometric (dimensional) optimization of a cylindrical and symmetrically segmented die will be performed; 3) In addition, guide lines for the design of the cylindrical and segmented die will be given. Additional factors that will be discussed include strain gage selection, bridge configuration, gage location and overload protection (a safety factor).

## OPTIMAL DESIGN METHODOLOGY

### Stress and Strain Analysis Tools

Engineering stress analysis can be accomplished either by the closed-form analytical method (from classical strength of materials) (3,4), or by numerical methods such as the finite element analysis (FEA). Each of these techniques has advantages and disadvantages. The analytical method is good for determining stress or strain in a simple geometry, and with the analytical stress/strain equations, the effects of a change in design parameters can be easily visualized. With numerical methods the calculations must be repeated with the new design parameters to see the effects of any design changes. However, with complex loading conditions and/or die shapes numerical analysis tools are required.

## DESIGN CONSTRAINTS

Two of the major concerns in the dimensional optimization of a force transducer are the sensitivity of the output signal to die wall stress and the effect of tablet height and position within the die on output signal linearity. For a transducer to have a measurable signal the strain at the gage site must exceed the minimum detection limit of the strain gage and data acquisition system. Because reducing the die wall thickness concentrates the forces into a smaller area which increases the strain (at the gage site) and hence the signal output, the die wall must be thin enough so that forces generated during compaction produce a measurable strain. Yet, the die wall must be thick enough to withstand the forces generated during compaction without yielding. Because of these competing demands, the dimensions of the transducer must be selected in a way that optimizes signal output without yielding or rupturing during compaction.

Another major concern in transducer design is signal linearity. Generally, a linear response is best for experimental work. Whether the calibration is linear or nonlinear, depends upon the design configuration (i.e. shape), strain gage placement, bridge configuration, materials used for construction and calibration method. A nonlinear response due to geometric nonlinearity is an inherent concern for the cylindrical and segmented die [1]. Because a transducer's response depends upon so many factors, it is very difficult to design and verify the linearity of a force transducer without using stress/strain analysis to simulate the design's performance. Thus, the

transducer configuration and associated strain gage arrangement should be selected in a way that minimizes the effects of tablet height and position on output signal linearity.

### Material Failure

There is an infinite number of combinations for the multiaxial loading of a material that can lead to its failure. Because it is impossible to characterize all of these combinations, failure criteria have been developed which use the uniaxial tensile strength to predict when multiaxial failure will occur. There are many accepted methods for predicting when material failure will occur, such as the maximum normal stress criteria, maximum shear stress criteria and Von Mises stress criteria (distortion energy theory). Collins (5) provides a comprehensive review of these methods. Generally, failure criteria give rules for the calculation of a single equivalent applied stress ( $\sigma_{app}$ ) from the multiaxial loading conditions, which may be compared to the uniaxial yield strength. Thus, to avoid failure within any part of the transducer, the  $\sigma_{app}$  must not exceed the uniaxial yield strength ( $\sigma_{yd}$ ) of the transducer material.

$$\sigma_{app} \leq \sigma_{yd} \quad (1)$$

In this way, the failure criteria can be used to estimate the point at which in-service stresses are likely to cause material yielding or rupture (5), making Equation (1) a very important design constraint in the determination of the die wall dimensions.

In this paper, the equivalent applied stress is defined by the distortional energy theory, or Von Mises stress ( $\sigma_{vm}$ ), which can be expressed as

$$\sigma_{vm} = \sqrt{\frac{1}{2}[(\sigma_1 - \sigma_2)^2 + (\sigma_2 - \sigma_3)^2 + (\sigma_3 - \sigma_1)^2]} \quad (2)$$

where  $\sigma_1$ ,  $\sigma_2$ , and  $\sigma_3$  are the material principal normal stresses [5].

To reduce the chances of catastrophic material failure brought about by uncertainties in material strength and in the loads acting upon the die, a safety factor ( $SF$ ) (6) is inserted into the applied stress equation. Thus, the equivalent applied stress ( $\sigma_{app}$ ) defined by the Von Mises' criteria can be written as

$$\sigma_{app} = SF \cdot \sigma_{vm} = SF \cdot \sqrt{\frac{1}{2}[(\sigma_1 - \sigma_2)^2 + (\sigma_2 - \sigma_3)^2 + (\sigma_3 - \sigma_1)^2]} \quad (3)$$

### Signal Measurement Limitations

Typically, detection of stress is accomplished by bonded electrical-resistance strain gages configured in a Wheatstone bridge that is calibrated for stress measurement. The output voltage ( $V_o$ ) from a Wheatstone bridge is usually in the millivolt range. With such low level signals, obtaining a satisfactory signal-to-noise ratio is difficult, especially with the electrical noise in a die stress measurement environment. In this section, the limitations imposed by electronic factors in signal processing and minimum detection level is discussed. Particular attention is paid to the relationship between signal output and strain, which dictates the minimum detectable strain for a given electronic measurement system. This information is of critical importance for the design of an efficient transducer.

When electrical-resistance strain gages are strained, their resistance changes; the equation governing this change is (7)

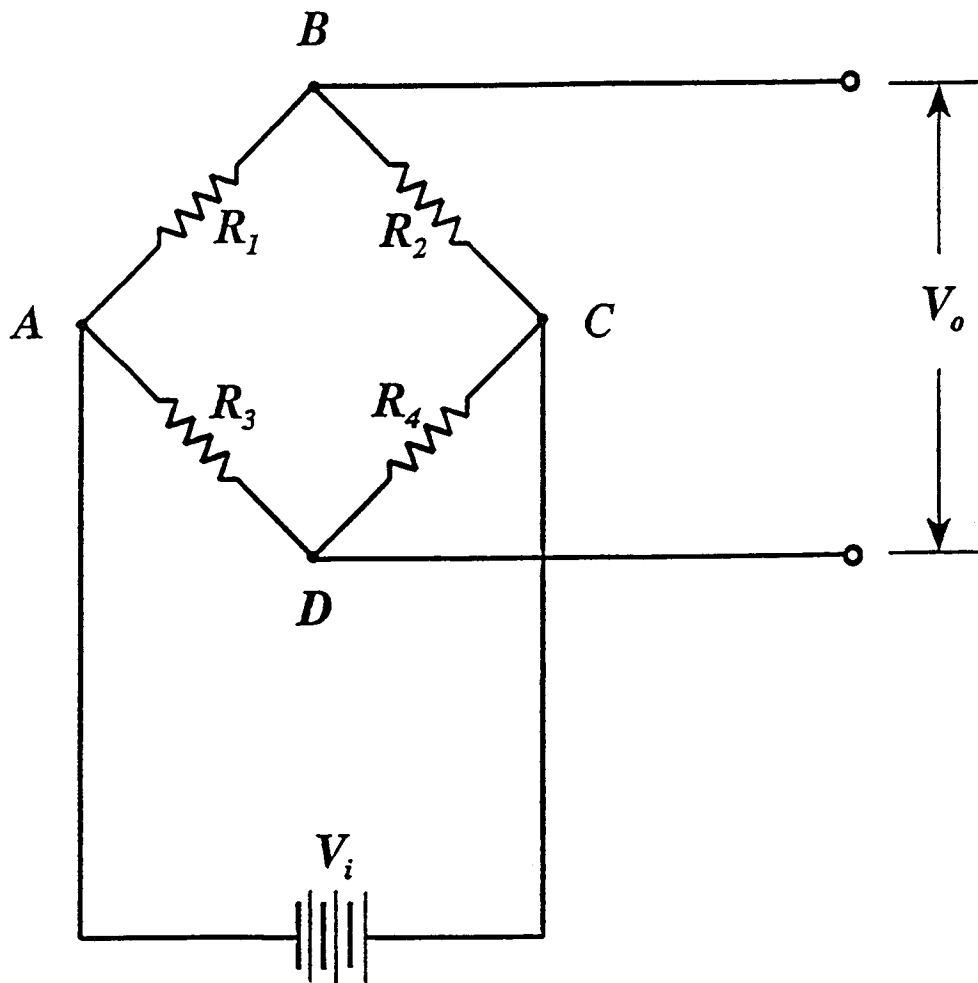
$$\frac{\Delta R}{R} = GF \varepsilon_a \quad (4)$$

where  $\Delta R$  is the change in resistance  $R$ , and  $\varepsilon_a$  is the axial strain. The gage factor  $GF$  is the proportionality constant between the axial strain and the change in resistance (i.e. the sensitivity of the gage to strain). Because bonded electrical-resistance strain gages are designed to measure strain in the axial direction, the primary determinant of the gage factor is the axial sensitivity of the gage; however, strain gages do respond to nonaxial or transverse strains. Thus, the gage factor also depends on the Poisson's ratio ( $\nu$ ) of the specimen and the transverse sensitivity of the gage. For most applications, the transverse sensitivity of the gage has an insignificant influence on the value of  $GF$ .

A Wheatstone bridge is one of the best ways to measure the small resistance changes produced by bonded electrical-resistance strain gages (see Figure B.2). The equation governing the output of the Wheatstone bridge is

$$V_o = V_i \frac{\rho}{(1+\rho)^2} \left( \frac{\Delta R_1}{R_1} - \frac{\Delta R_2}{R_2} + \frac{\Delta R_3}{R_3} - \frac{\Delta R_4}{R_4} \right) \quad (5)$$

where  $V_i$  is the bridge excitation voltage,  $R_1$ ,  $R_2$ ,  $R_3$ , and  $R_4$  are the resistances of the bridge arms, and  $\rho$  is the ratio  $R_2/R_1$  (7). The second order nonlinear terms have been neglected in Equation (5), and for some bridge configurations this limits the linear range of the equation to strains less than 10,000  $\mu\varepsilon$ . For a single-arm bridge, the nonlinearity in this strain range is less than 0.5% and can be ignored (8); however, for larger strains the nonlinearity increases rapidly and cannot be ignored.



B.2 The Wheatstone bridge circuit.



By substituting Equation (4) into Equation (5), the general linear relationship for bridge output  $V_o$  and the surface strain  $\epsilon_i$  at the different gage sites can now be expressed as:

$$V_o = S_r \epsilon_{eff} \quad (6)$$

where  $S_r$  is the overall bridge sensitivity, and  $\epsilon_{eff}$  is the effective strain for the bridge, which is expressed as:

$$\epsilon_{eff} = \sum_{i=1}^n \epsilon_i \quad (7)$$

where  $n$  is the number of active strain gages used to configure the bridge.

Consequently, the bridge sensitivity, which depends on bridge configuration, can be expressed as:

$$S_r = V_i \frac{\rho}{(1+\rho)^2} nGF \quad (8)$$

Every data acquisition system has an optimal detection range with a lower limit ( $V_{min}$ ). To acquire data the lower detection limit imposes the constraint,  $V_o \geq V_{min}$ , on bridge output; and with the application of Equation (6), this inequality can be expressed in terms of strain:

$$V_{min} \leq S_r \epsilon_{eff} \quad (9)$$

Equation (9) summarizes the electronic constraints for transducer design, and along with Equation (8) they also illustrate three methods for improving output signal detection. First,  $V_{min}$  can be lowered by improving the signal processing equipment. This method is independent of transducer design and beyond the scope of this paper. Second, the  $S_r$  can be increased either by increasing the number of active gages  $n$  or the

excitation voltage  $V_i$ . Reconfiguring the bridge is limited to a four-fold increase in  $GF$ . In addition, Equation (5) shows that two of the bridge arms have a positive sign and the other two have a negative sign. Therefore, unless there are areas of tension and compression on the transducer only two active strain gages can be used, because electronic cancellation of the strain signal will occur. In most cases, die wall stress measurement is limited to one or two active gages. Also, the bridge excitation voltage can be increased. However, because excessive power dissipation in the gages will cause temperature changes that introduce errors in measurement (9), increases in the bridge excitation voltage are limited. The third way of increasing the output voltage is to increase the strain level at the gage sites. With the segmented die, the strain is increased by decreasing the die wall thickness in the cut-away portion; however, the die wall cannot be made too thin because yielding and fracture may occur.

#### Strain gage limitations

In terms of transducer design, the primary constraints imposed by a strain gage are the gage elongation and gage fatigue limits. All strain gages have elongation limits, that if exceeded, will permanently damage the strain gage. Typical elongation limits for a strain gage range from 0.5% to 5%, depending upon factors such as grid alloy, matrix construction, bonding adhesive and gage size. In addition, gages can also fail in fatigue because cyclic loading of a gage causes the grid alloy to work harden, resulting in a permanent resistance change. The fatigue life depends on the strain level. For example, the fatigue life of a Constantan strain gage increases from  $10^2$  cycles to greater than  $10^8$  cycles when the cyclic strain level drops from 2,700  $\mu\epsilon$  to 1,200  $\mu\epsilon$

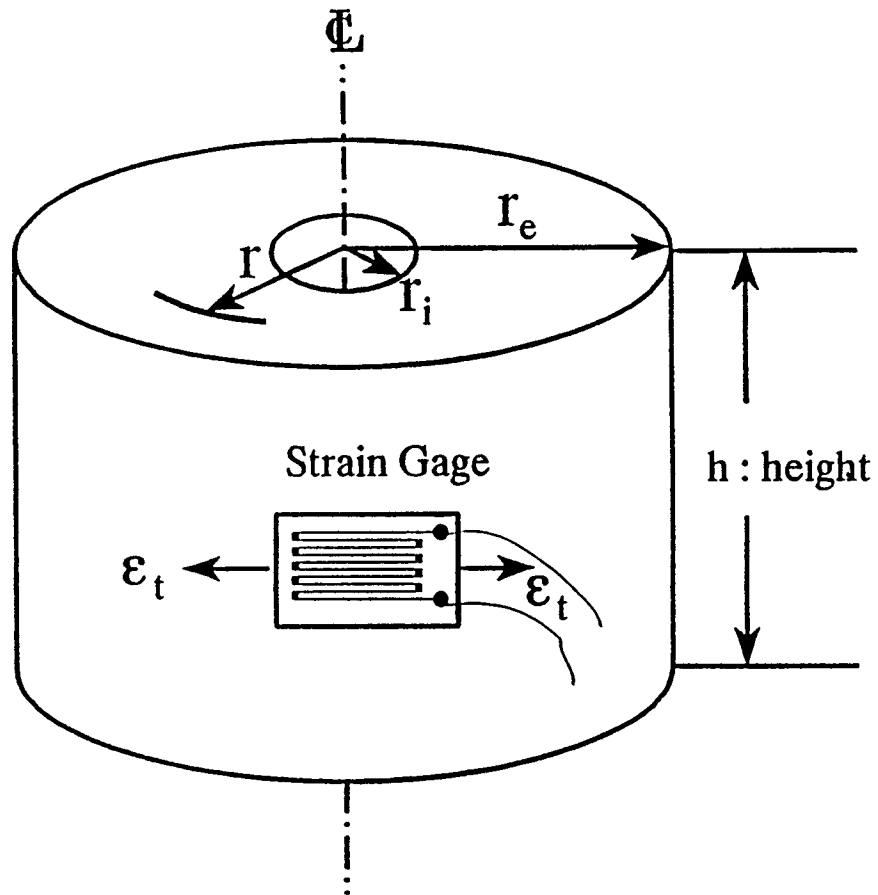
(7). Because this fatigue strain limit ( $1,200 \mu\epsilon$ ) is more stringent it will be used for the strain gage elongation limit in this paper. Therefore, to prevent strain gage damage, the strain levels at the gage site must not exceed the fatigue strain limit. Because the commonly used D3 tool steel is very brittle, the transducer will typically yield or fracture before the strain gage fails; thus, strain gage limits do not usually impose significant constraints on transducers constructed from brittle materials. However, if a more ductile material is used, then this constraint becomes much more important.

### DESIGN EXAMPLES

Dimensional optimization is the main subject of the following two design examples. For the first example, the maximum and minimum die wall thicknesses ( $t$ ) of a cylindrical die are determined using the analytical method. Then FEA is used to determine the optimal dimensions for the cut-away geometry of a segmented die; followed by an analysis of the effects of tablet height and position and strain gage placement on output signal.

#### Cylindrical Die Design (Analytical Method)

To illustrate the analytical method, the admissible range of die wall thicknesses will be calculated for the cylindrical die described by Watt (1) and shown in Figure B.3. Although die wall stress depends on tablet height and location during compaction, these stress/strain calculations will be done assuming a uniform radial pressure ( $p_i$ )



**B.3** Cylindrical die with a single active gage mounted horizontally on the die surface  $r = r_e$ .

applied to the entire inner surface of the die. This assumption simulates the severest loading conditions. In addition, it will be assumed that only radial die wall forces are present and the ends of the die are free of any applied loads, these assumptions eliminate all axial stresses within and on the die wall ( $\sigma_z = 0$ ). Even though punch movements during compaction generate die-wall friction, as shown in the literature for most well lubricated formulations the axial forces generated by die-wall friction are minimal (10,11,12). Thus, the assumption of  $\sigma_z = 0$  is valid for most compaction conditions.

The above conditions reduce the analysis to a two-dimensional plane strain problem, which makes the analytical solution more tractable. The problem of uniform pressure in a cylinder is called Lamé's problem. The solutions for the radial and tangential stresses are given by (3,4,13):

$$\sigma_r = -p_i \frac{[(\frac{r_e}{r})^2 - 1]}{\lambda^2 - 1} \quad (10a)$$

and

$$\sigma_\theta = p_i \frac{[(\frac{r_e}{r})^2 + 1]}{\lambda^2 - 1} \quad (10b)$$

where  $\lambda = r_e/r_i = 1+t/r_i$ , and the other symbols are defined in Table B.1. In addition, the tangential strain is represented by

$$\varepsilon_\theta = \frac{2r_i^2 p_i}{E(r_e^2 - r_i^2)} \quad (11)$$

where  $E$  is the elastic modulus.

Table B.1 Definition and parameters used for the cylindrical die calculations.

Parameter	Symbol	Value
Die wall thickness	$t$	-
Bore radius of die	$r_i$	5 mm
Radius of external surface	$r_e$	5 mm + $t$
Radial location	$r$	$r_i \leq r \leq r_e$
Maximum compaction pressure	$P_{\max}$	120 MPa

### Failure Analysis

Once the stress/strain fields have been determined, the minimal die wall thickness which does not yield can be calculated using the Von Mises failure criteria, Equation (2). Recalling that the principal stresses are the three normal stresses that occur when the coordinate axes are aligned so that all shear stresses equal zero. Because there are no shear stresses for the loading conditions described above, the principal stresses are equal to the normal stresses;  $\sigma_1 = \sigma_r$ ,  $\sigma_2 = \sigma_\theta$ , and  $\sigma_3 = \sigma_z$ . By substituting the principal stress Equations (10a) and (10b) into Equation (2), the Von Mises stress  $\sigma_{vm}$  becomes

$$\sigma_{vm} = [\sigma_r^2 + \sigma_\theta^2 - \sigma_r \sigma_\theta]^{1/2} = P_i \frac{\sqrt{3\beta^4 + 1}}{\lambda^2 - 1} \quad (12)$$

where  $\beta = r_i/r$ . Figure B.4 plots the normalized radial, tangential, and Von Mises stresses versus distance ( $r$ ) for the cylindrical die. Figure B.4 shows that the maximum and minimum Von Mises stresses occur at the internal and external surfaces of the die, respectively, and Equation (12) confirms that the maximum and minimum equivalent Von Mises stresses always occur at the inner and outer die wall surfaces irrespective of the die wall dimensions. However, as the die wall thickness increases, the Von Mises stress decreases.

To determine the minimum die wall thickness, the failure criteria Equation (1) is applied at the inner die wall surface, which is the critical point most likely to fail. The

equivalent applied stress  $\sigma_{app}$  can be obtained by substituting Equation (12) into Equation (3) and noting that  $\lambda = \beta$  when  $r = r_i$ :

$$\sigma_{yd} = SF \cdot p_i \frac{\sqrt{3\lambda^4 + 1}}{\lambda^2 - 1} \quad (13)$$

To calculate  $\lambda$ , the four roots of Equation (13) can be determined by twice applying the quadratic equation. The material properties for the D3 tool steel and the other parameters used for the calculation are shown in Table B.2. Because  $\lambda = r_o/r_i \geq 1$ , the only solution of interest for Equation (13) is  $\lambda \geq 1.778$ . Therefore, for a cylindrical die with an inner diameter of 5 mm the minimum die thickness ( $t$ ) required to prevent material yielding is

$$t \geq 3.89 \text{ mm}$$

### Signal Output

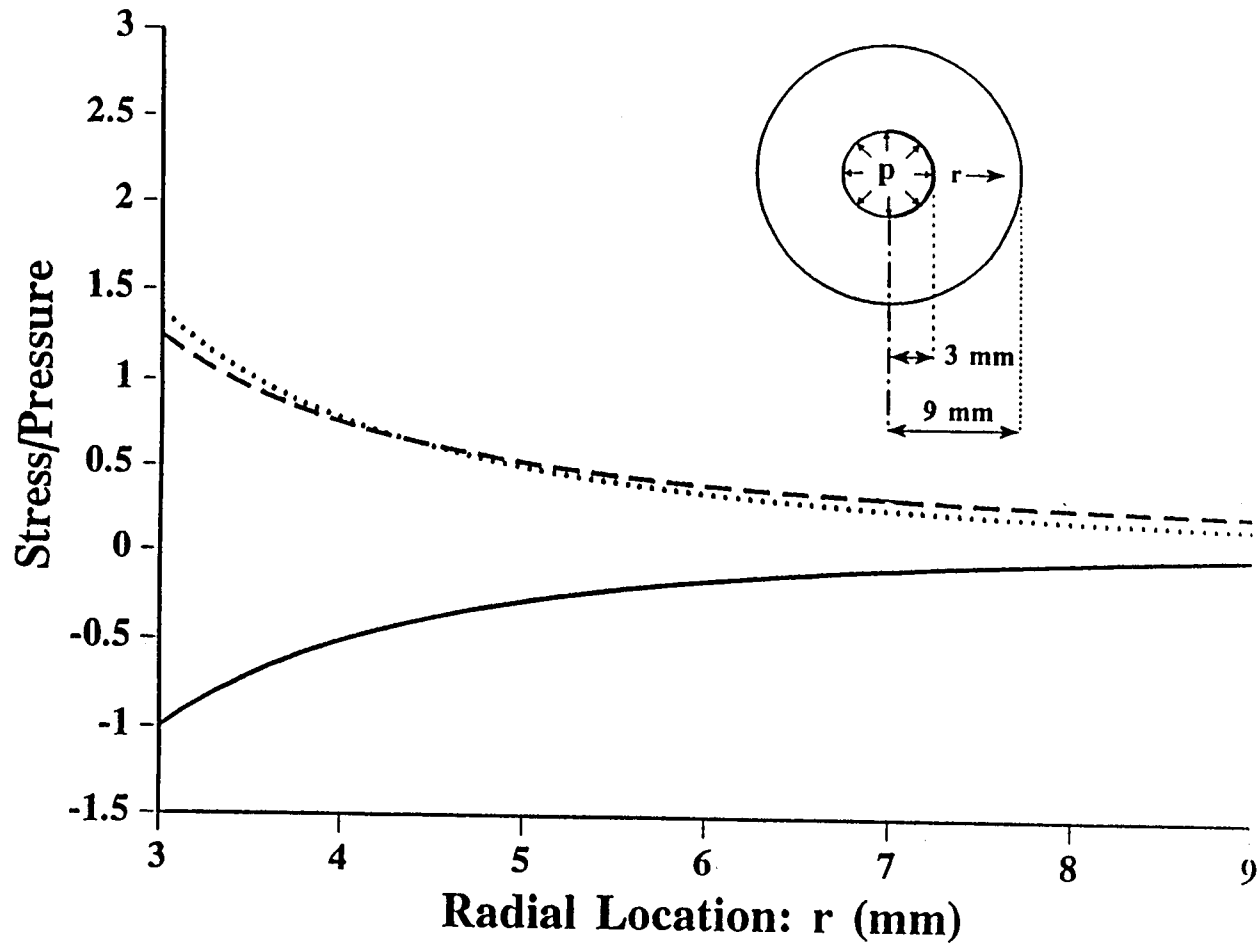
For a given lower stress detection limit, Equation (9) can be used to calculate the maximum die wall thickness from which a measurable output signal may be obtained. These calculations are done for a cylindrical die instrumented with a single strain gage mounted horizontally on the outer surface of the die,  $r = r_o$  (see Figure B.3), and with the gage configured into a non-temperature compensating, single arm Wheatstone bridge. To use Equation (9), the bridge sensitivity ( $S_r$ ) must be calculated for both the bridge configuration and the type of gage used. Also,  $\epsilon_{eff}$  must be determined at the gage site. Because there is only one active gage ( $n = 1$ ) mounted horizontally, the



Table B.2 D3 tool steel material properties used for stress/strain calculations.

Parameter	Symbol	Value
<b>D3 Tool Steel</b>		
Young's modulus	E	$2 \times 10^5$ MPa
Poisson's ratio	$\nu$	0.3
Yield strength	$\sigma_{yd}$	340 MPa
Safety Factor	SF	1.1
<b>Strain Gage*</b>		
Gage Factor	$GF$	2.01
Maximum Power Dissipation	$P_g$	0.15 W
Gage Resistance	$R_g$	120 $\Omega$

\* Model EA-06-03 IDE-120, Measurements Group, Inc., Raleigh, NC,



B.4 Distributions of the normalized radial stress  $s_r/P_{max}$  (—), tangential stress  $s_t/P_{max}$  (---) and Von Mises stress  $s_{vm}/P_{max}$  (···) along a radial line for cylindrical die ( $r_i = 3$  mm,  $r_o = 9$  mm).

effective strain equals the tangential strain,  $\varepsilon_{\text{eff}} = \varepsilon_{\theta}$ , which can be calculated by Equation (11).

To obtain the maximum bridge sensitivity, Equation (8) must be expressed in terms of the maximum power dissipation, which does not induce temperature changes within the gage. To do this, the excitation voltage in Equation (8) must be expressed in terms of a gage's power dissipation capability ( $P_g$ ) and resistance ( $R_g$ ). For a single arm bridge with all arms having the same resistance,  $V_i$  can be written as:

$$V_i = (1 + \rho)\sqrt{P_g R_g} \quad (14)$$

Substituting Equation (14) into Equation (8) and (9) yields for a single arm bridge:

$$S_R = \frac{V_o}{\varepsilon_{\text{eff}}} = \frac{\rho}{1 + \rho} GF \sqrt{P_g R_g} \quad (15)$$

To determine the maximum die wall thickness, first the desired minimum detectable strain at the gage site is calculated using Equation (15) and the lower detection limit  $V_{\text{min}}$ . The outer radius  $r_e$  can be calculated by substituting the minimum detectable strain into Equation (11) yielding:

$$\frac{2 r_i^2 p_i}{E(r_e^2 - r_i^2)} \geq \varepsilon_{\text{eff}} = \frac{V_{\text{min}}}{S_r} \quad (16)$$

If the required minimum output bridge voltage  $V_o$  from the Wheatstone bridge is 0.5 mV, and a Measurements Group, Inc. model EA-06-031DE-120  $\Omega$  strain gage (see Table B.2 for parameters) is used, then the tangential surface strain  $\varepsilon_{\theta}$  that would produce at least 0.5 mV can be calculated using Equation (16). After rearrangement the minimum die wall dimensions can be calculated:

$$r_i \leq r_o = r_i + t \leq \sqrt{2.5583 \times 10^{-4} + r_i^2} \quad (17)$$

Thus, for  $r_i = 5$  mm, the required wall thickness which can produce at least 0.5 mV bridge output at 120 MPa of compact pressure is in the range of:

$$0 \leq t \leq 11.76 \text{ mm}$$

### Strain Gage Limitations

By substituting  $\varepsilon_{\text{fatigue}}$  for  $\varepsilon_{\text{eff}}$ , Equation (16) can be used to calculate the minimum die wall thickness needed to prevent strain gage damage:

$$\varepsilon_{\theta} \leq \varepsilon_{\text{fatigue limit}} = 1200 \mu\varepsilon \quad (\text{for } 10^8 \text{ cycles}) \quad (18)$$

As discussed above, the strain gage fatigue limit of 1200  $\mu\varepsilon$  is used for the maximum strain gage elongation. With this constraint, the minimum wall thickness required to prevent damage to the installed strain gages at a  $P_{\text{max}}$  of 120 MPa is 2.09 mm. Because the gage limit is larger than the failure limit, constraints imposed by the strain gages are not important in this situation.

### Summary

In conclusion, the optimal die-wall thickness (feasible wall thickness in Figure B.5) which produces maximum bridge signal output without damaging the transducer or the installed strain gages is

$$3.98 \text{ mm} \leq t \leq 11.76 \text{ mm}$$

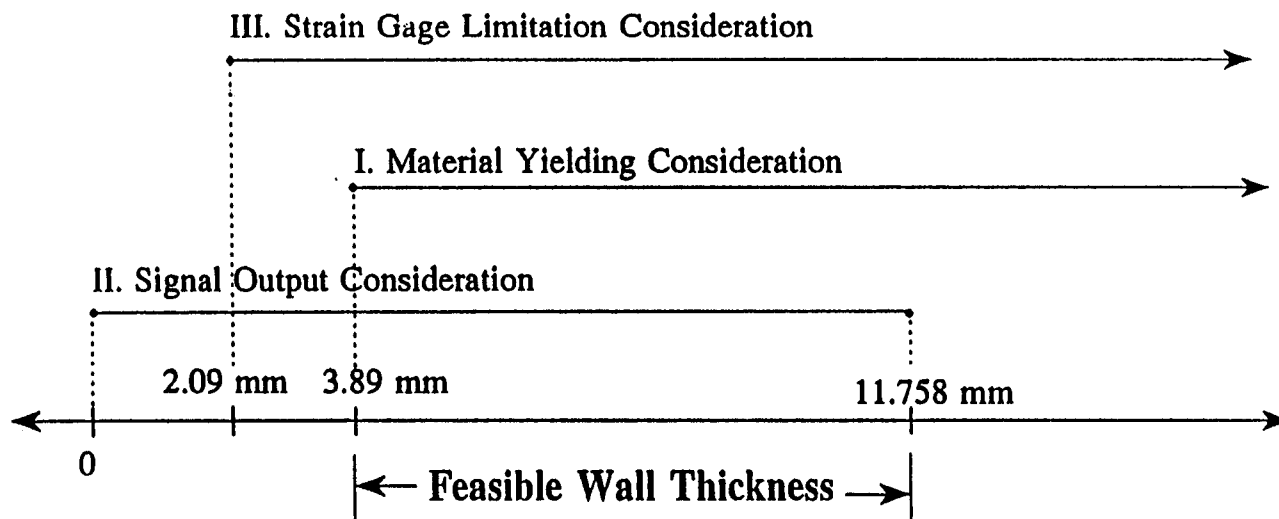
### Segmented Die Design (FEA Numerical Method)

For more complicated geometries like the segmented die numerical techniques such as FEA (Finite Element Analysis) must be used. Basically, FEA is a numerical method which divides a mechanical component into many small body elements, called, "finite elements," for the purpose of easy stress/strain analysis. These elements are interconnected at specified points called nodes or nodal points (see Figure B.6). For more information on FEA the reader can refer to excellent texts, such as Cook et al. (14) and Rao (15). In this research, the commercially available FEA software program COSMOS/M (16) was used to perform the stress/strain analysis.

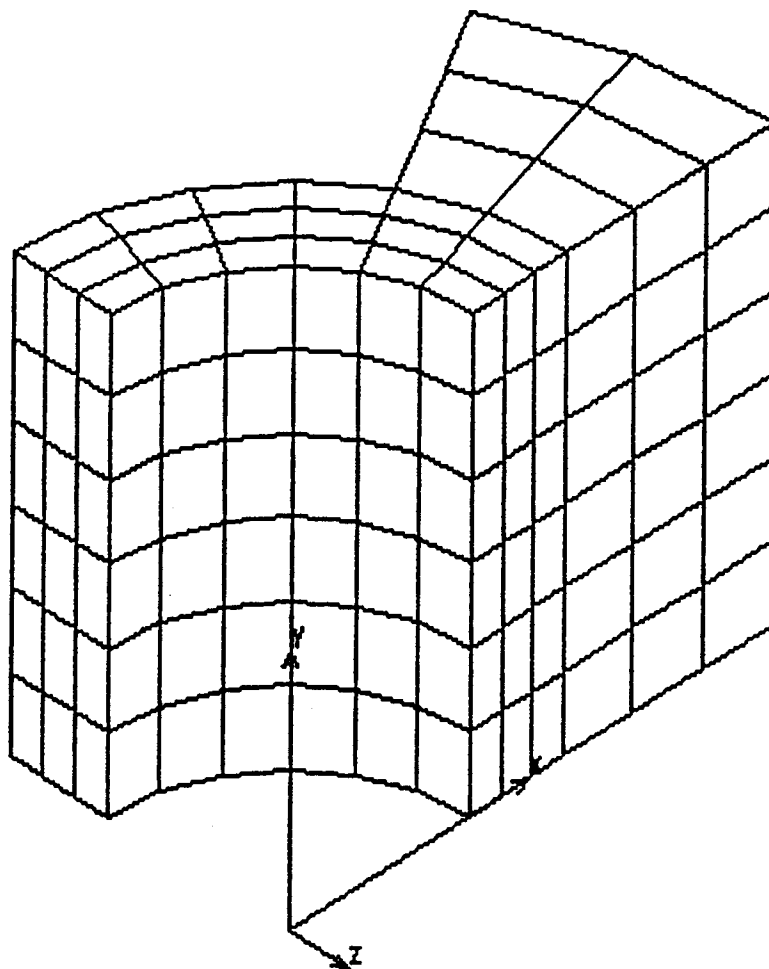
To illustrate the FEA numerical method, the effect of the cut-away geometry and strain gage arrangement on die-wall material failure, signal output level and signal linearity for the segmented die are evaluated. The primary factor affecting material failure and signal output level is the cut-away geometry, which is comprised of two factors: the cutting angle ( $\phi$ ) and the effective die-wall thickness ( $t$ ) (see Figure B.7). The primary factors affecting signal linearity are tablet height and position within the die and strain gage arrangement.

### Cutting Angle and Die Wall Thickness

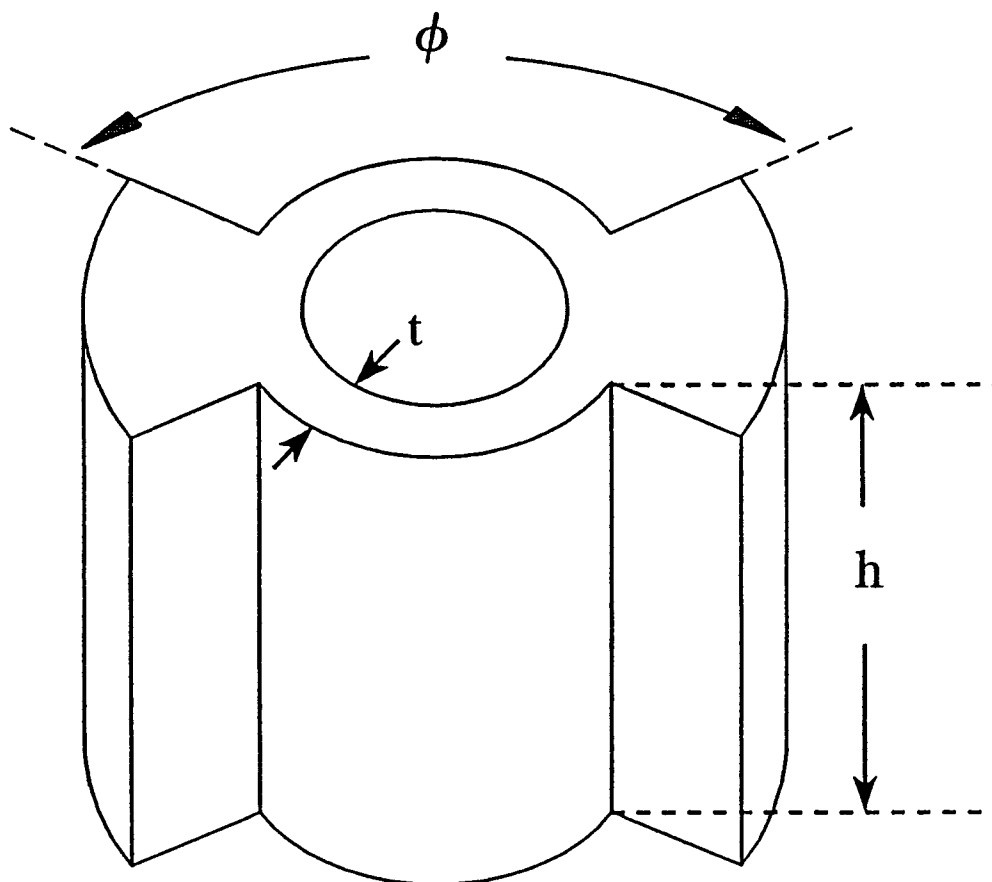
For the FEA of cutting angle and die-wall thickness, the first step is to create a finite element computer model by dividing the segmented die into discrete finite elements. For the symmetrically segmented die with  $t = 3$  mm and  $\phi = 120^\circ$ , the finite element model is shown in Figure B.6. Because of symmetry, only one-eighth of the



**B.5** Optimal die wall thickness (feasible wall thickness) for a cylindrical-shape die based on given design constraints and closed-form analytic analysis.



**B.6** Finite element model of one-eighth of the symmetrical segmented die generated by COSMOS/M using 144 3D, 8-node, solid elements.



**B.7** The symmetric segmented die;  $\phi$ : cut-away angle,  $t$ : effective wall thickness, and  $h$ : die height.



segmented die was modeled; this smaller model reduces computer time needed for computation. The model consisted of 144 3-D, 8-nodal solid elements [16], and 259 nodal points. Again, an internal die-wall pressure ( $P_i$ ) of 120 MPa uniformly applied to the entire inner surface of the die was used to simulate the severest compaction loading conditions. The material properties of a D3 tool steel were used for the calculations (the same as in the previous example, see Table B.2; the bore diameter and outer die-wall thickness are given in Table B.3. The finite element model was set up with cutting angles of 30°, 60°, 90° and 120°, and with effective die-wall thicknesses of 1, 2, 3, 4, and 5 mm in the cut-away section. The calculations were done using the FEA program, COSMOS/M (16), running on a 486, 33 MHz personal computer.

The FEA program calculates the Von Mises stress for every nodal point of the segmented die model shown in Figure B.7. The results show that the greatest Von Mises stress occurs on the inner die wall surface while the lowest Von Mises stress occurs in the thickened portion of the outer die wall, and these maximum and minimum Von Mises stresses always occur at these points for all cutting angles and die wall thicknesses examined. One concern in the analysis of failure for the segmented die is the concentration of stress in the corners at edges of the cut-away section. However, calculations show that the Von Mises stress at these nodes is well below the Von Mises stress on the inner die wall. Therefore, when analyzing material failure for this segmented die model, stress concentration in these regions can be ignored, because the inner die wall will fail first.

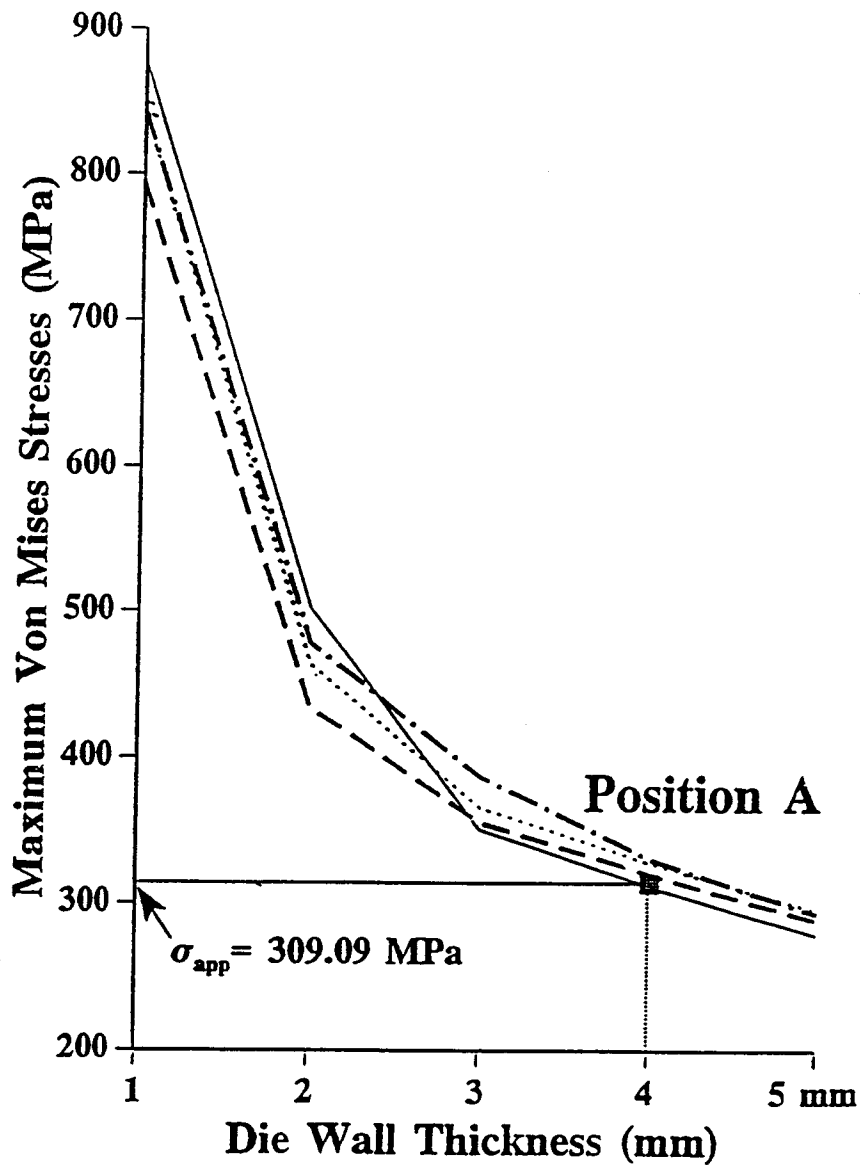
Table B.3 Definition and parameters used for the segmented die calculations.

Parameter	Symbol	Value
Die Wall thickness	$t$	1 - 5 mm
Cutting angle	$\phi$	30° - 120°
Bore radius of die	$r_i$	5.65 mm
Radius of external surface	$r_o$	15 mm
Height of Die	$h$	25 mm
Radial location	$r$	$r_i \leq r \leq r_o$
Maximum compaction pressure	$P_{\max}$	120 MPa

A summary of the FEA results is shown in Figure B.8, where the maximum Von Mises stress (at the inner die wall) is plotted versus the die-wall thickness ( $t = 1 - 5$  mm) for each cutting angles ( $\phi$ ) between  $30^\circ$  and  $120^\circ$ . For cutting angles in the range of  $30^\circ - 120^\circ$  the maximum Von Mises stress does not change very much; however, increasing the die-wall thickness from 1 to 5 mm decreases the maximum Von Mises stress by approximately 300%.

Calculations like those shown in Figure B.8 are essential for the design of a segmented die because they provide the designer with a systematic guide for selecting die-wall thicknesses and cutting angles which do not yield when peak loads are applied. For example, if the desired segmented die has a cutting angle  $\phi = 30^\circ$ , a safety factor  $SF = 1.1$ , and a material yield strength  $\sigma_{yd} = 340$  MPa, the minimum die-wall thickness that will not yield during compaction (for a maximum die-wall pressure of 120 MPa) can be determined from Figure B.8. By calculating the maximum effective Von Mises stress from the applied stress (i.e.  $\sigma_{app} = 340/1.1 = 309$  MPa, Equation (3)) the minimum die-wall thickness of 4 mm can be read off of Figure B.8 (see position A). This result suggests that die-wall yielding may explain why Huckle and Summers [17] found a hysteresis response in their segmented die with a 3 mm die-wall thickness.

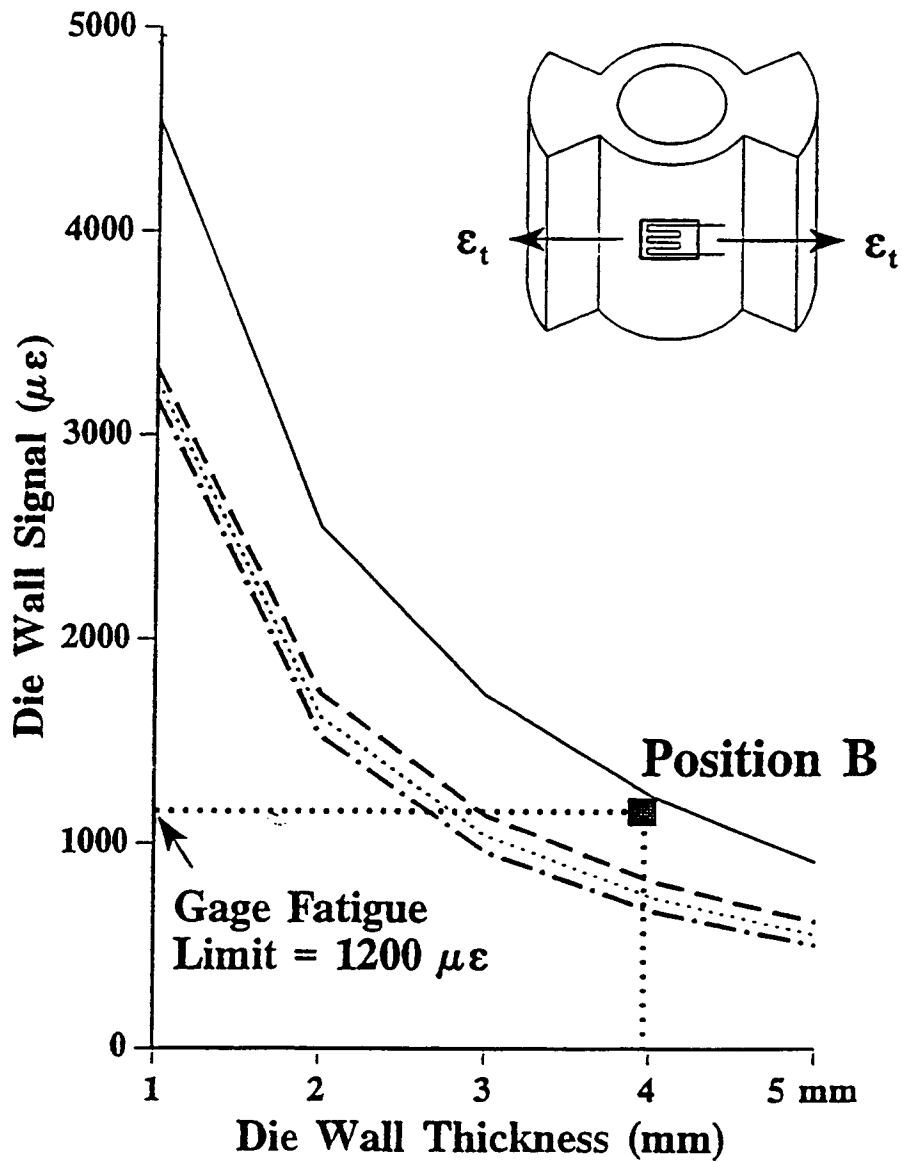
In terms of transducer design, the signal output is typically a linear function of the strain (see Equation (6)) at the gage site; therefore, this analysis of output signal is based upon the surface strain in the cut-away portion of the die wall. Using the same finite element model, cutting angles and effective die-wall thicknesses as above, the



B.8 Maximum Von Mises stresses at a 120 MPa die-wall pressure for four cut-away angles ( $f = 30^\circ$ :—,  $60^\circ$ :—,  $90^\circ$ :xxx,  $120^\circ$ :-x-x) and effective die-wall thicknesses ( $t = 1$  mm - 5 mm).

tangential surface strain  $\epsilon_0$  (i.e. the strain for a single strain gage mounted horizontally in the middle of the cut-away section) was also calculated with the FEA program, COSMOS/M. Figure B.9 illustrates that when the die-wall thickness is reduced from 5 to 1 mm the average strain increases by a factor of three or more. Generally, the smaller the cutting angle, the larger the strain, and when the cutting angle is less than  $60^\circ$  the strain is very sensitive to changes in the cutting angle. For example, if  $t = 3$  mm, the strain increases approximately 1.5 times (from  $1200 \mu\epsilon$  to  $1800 \mu\epsilon$ ) when the cutting angle is reduced from  $60^\circ$  to  $30^\circ$ . Ideally, a transducer (not exposed to cyclic loading i.e. the designer is not concerned about fatigue life) would have a full scale strain of 1,000 to  $1,700 \mu\epsilon$  (18); however, lower strains are still acceptable. Based upon Figure B.9, a segmented die with a die wall thickness of 4 to 5 mm and cutting angles between  $60^\circ$  and  $120^\circ$  will produce an adequate signal.

Also when selecting the optimal dimensions of a segmented die to match strain gage fatigue limits, the designer should consider gage size, gage location and gage configuration. In this particular case, if an EA-06-031DE-120 strain gage (Measurements Group, Inc., fatigue limit:  $10^8$  cycles @  $1200 \mu\epsilon$ ) is used on a die with an effective die-wall thickness of 4 mm, using Figure B.9, the cutting angle should be approximately greater than  $37^\circ$  (location B in Figure B.9) in order to keep the local strains below the gage fatigue limit.



B.9 Die Wall Signals at a 120 MPa die-wall pressure for four cut-away angles ( $f=30^\circ$ :—,  $60^\circ$ :---,  $90^\circ$ :····,  $120^\circ$ :-·-·) and effective die-wall thicknesses ( $t=1$  mm - 5 mm).

### Tablet Height and Position and Strain Gage Arrangement

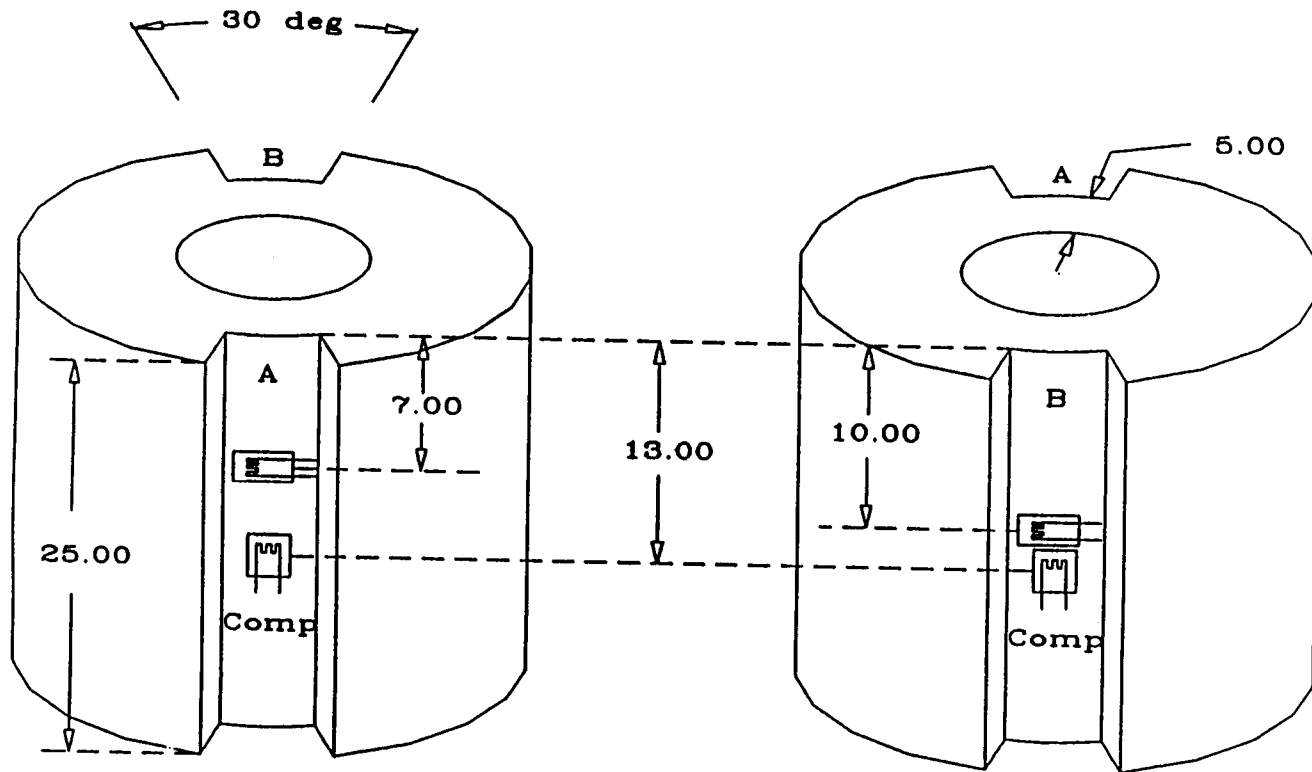
The abundance of segmented die designs reported in the literature (1), makes it impossible to analyze all of the available designs. Thus, this analysis of tablet height and position and strain gage arrangement will be limited to the segmented die and strain-gage arrangements developed by Hölzer and Sjögren (19), (see Figures B.10A and B.10B). By using FEA to reproduce the experimental output signals of Hölzer and Sjögren (19), the effects of tablet height and position and strain gage arrangement on signal linearity can be judged. In addition, this analysis will help to verify the FEA results.

Again, the first step in FEA is to create a finite element computer model by dividing the segmented die of Hölzer and Sjögren (19) into discrete finite elements (see Figure B.11). To simulate the loading conditions during compaction, the inner die-wall pressure is applied only to the areas where the tablet actually comes in contact with the die wall (see pressure arrows in Figure B.11). Consistent with Hölzer and Sjögren's (19) experimental setup, the tablet height (i.e. area in contact with the die wall) was modeled by fixing the upper punch penetration at 4 mm, while the lower punch penetration was varied from 6 to 14 mm in 1 mm increments. The parameters used for the FEA of Hölzer and Sjögren's die (19) are shown in Table B.4. Because of symmetry, only one-quarter of the segmented die was modeled. The finite element model consisted of 825 3-D, 8-nodal solid elements (16), and 1196 nodal points. The material properties of a D3 tool steel were used for the calculations (see Table B.2).

Based upon the FEA of Hölzer and Sjögren's die (19), the Von Mises stress contour and the simulated deformed shape are shown in Figures B.12 and B.13, respectively. The reader should note that Figure B.13 is an exaggerated view drawn to better visualize the die-wall deformation, which is actually less than 5  $\mu\text{m}$ . Based upon the strain in the segmented die (see Figure B.13), the resulting signal for the different strain gage arrangements can be calculated for the different tablet heights. The output signal for the temperature-compensating adjacent-arm bridge configurations 10 A and B can be calculated with Equation (6). As before, the analysis of signal output is based upon the effective strain Equation (7) rather than upon the actual output voltage. Thus, the effective strains for bridge configurations A and B are given by  $\epsilon_{\text{eff}} = \epsilon_a - \epsilon_c$  and  $\epsilon_{\text{eff}} = \epsilon_b - \epsilon_c$ , respectively. Where  $\epsilon_a$  and  $\epsilon_b$  are the axial strains for the active gages in bridge configurations A and B, respectively,  $\epsilon_c$  is the axial strain in the temperature compensating gages.

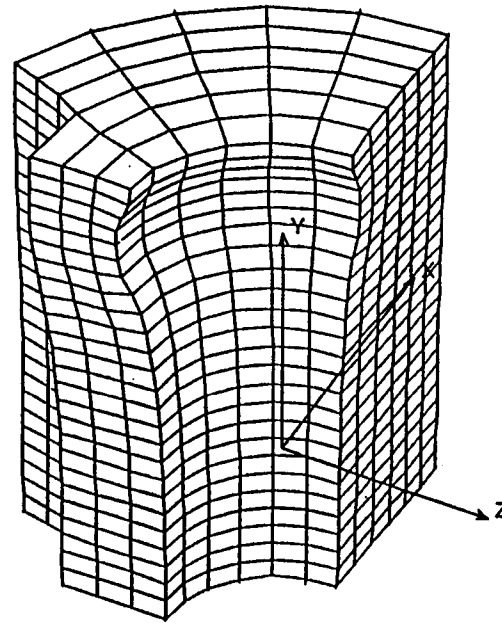
The final results (plotted in Figure B.14), show that changing the strain gage location will change signal output, and that for a fixed pressure changes in tablet height will also change signal output. This inherent geometric nonlinearity of the segmented die can be better understood by looking at the Von Mises stress contour (for elastic bodies there is a one-to-one correspondence between stress and strain, note Figure B.12). In this figure, the stress contours radiate out in a circular fashion from the area of contact between the die wall and tablet. As a result, the surface strain on the outer die wall varies with location; therefore, signal output will also vary with strain gage





B.10 Dimensions of the segmented die ( $f = 30^\circ$ ,  $t = 5 \text{ mm}$ ,  $r_i = 11.2 \text{ mm}$ ) selected for finite element analysis with Hölzer and Sjögren's [19] strain gage configuration.

Lin DEF Lc=1



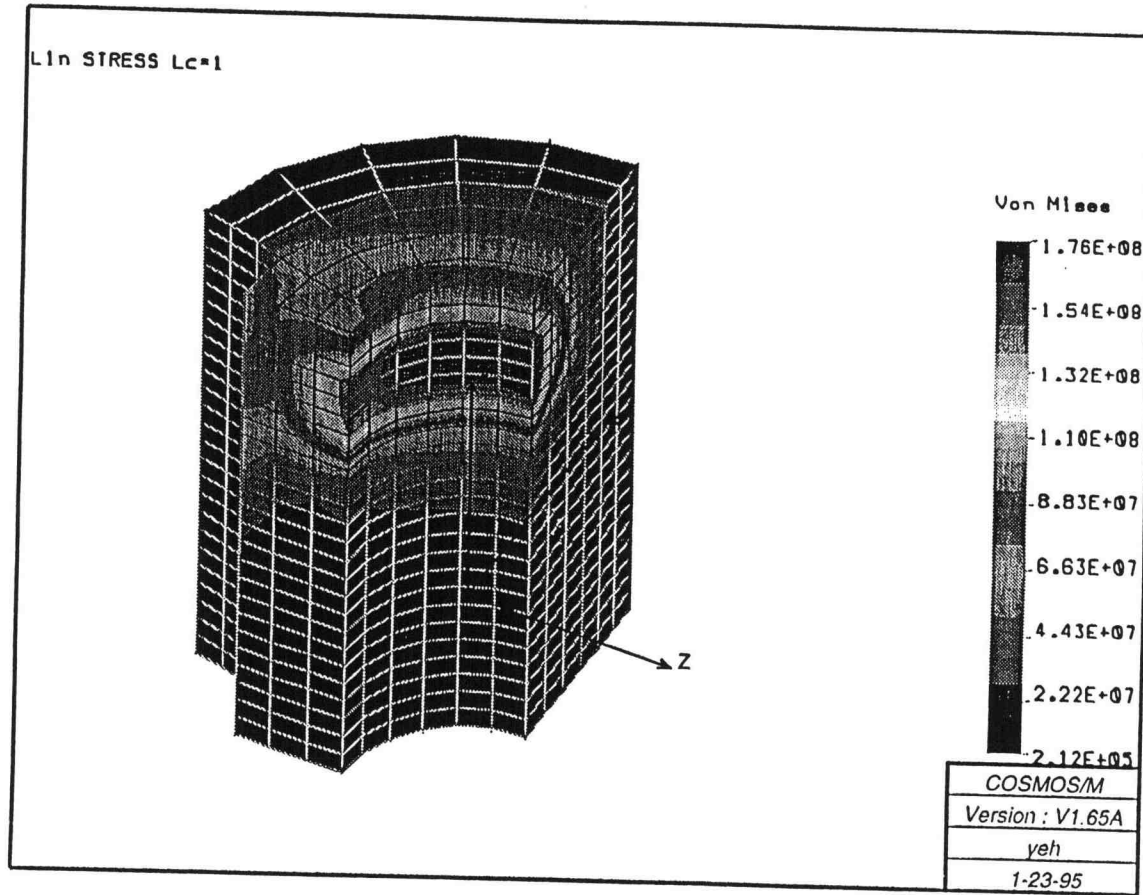
**B.11** Finite element model for tablet-compaction simulation using symmetric segmented die [19] with  $f = 30^\circ$ ,  $t = 5$  mm and bore radius equal to 11.2 mm. Compact height corresponding to 4 mm upper and 9 mm lower punch penetration and a die-wall pressure equal to 120 MPa shown by arrows.

Table B.4 Definition and parameters used for Hölzer and Sjögren's segmented die calculations.

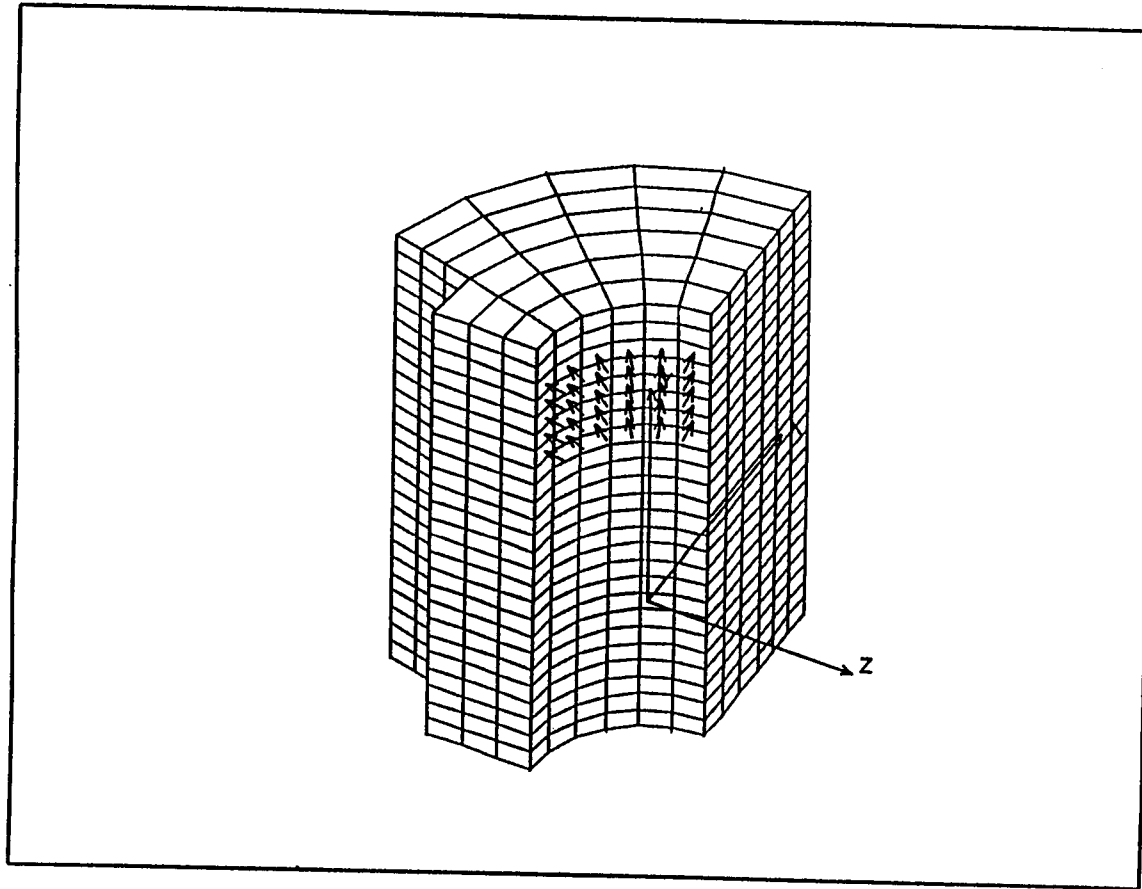
Parameter	Symbol	Value
Die Wall thickness	$t$	5
Cutting angle	$\phi$	30°
Bore radius of die	$r_i$	5.65 mm
Radius of external surface	$r_o$	15 mm
Height of Die	$h$	25 mm
Radial location	$r$	$r_i \leq r \leq r_o$
Maximum compaction pressure	$P_{\max}$	120 MPa

location. In addition, because the stress contours radiate out from the area of contact between the tablet and die wall, the stress distribution (for a fixed pressure) at the outer die wall will also change when the area of contact between the tablet and die wall changes; therefore, signal output will also change when the height of the tablet changes. These results help to explain the well known but often under appreciated fact that the output signal for a segmented die with a fixed tablet height is linear, but when the tablet height is varied (as in tablet compaction) the output becomes nonlinear. Note that for the segmented die, these effects can be mitigated to some extent by using special strain gage arrangements like those developed by Huckle and Summers [20].

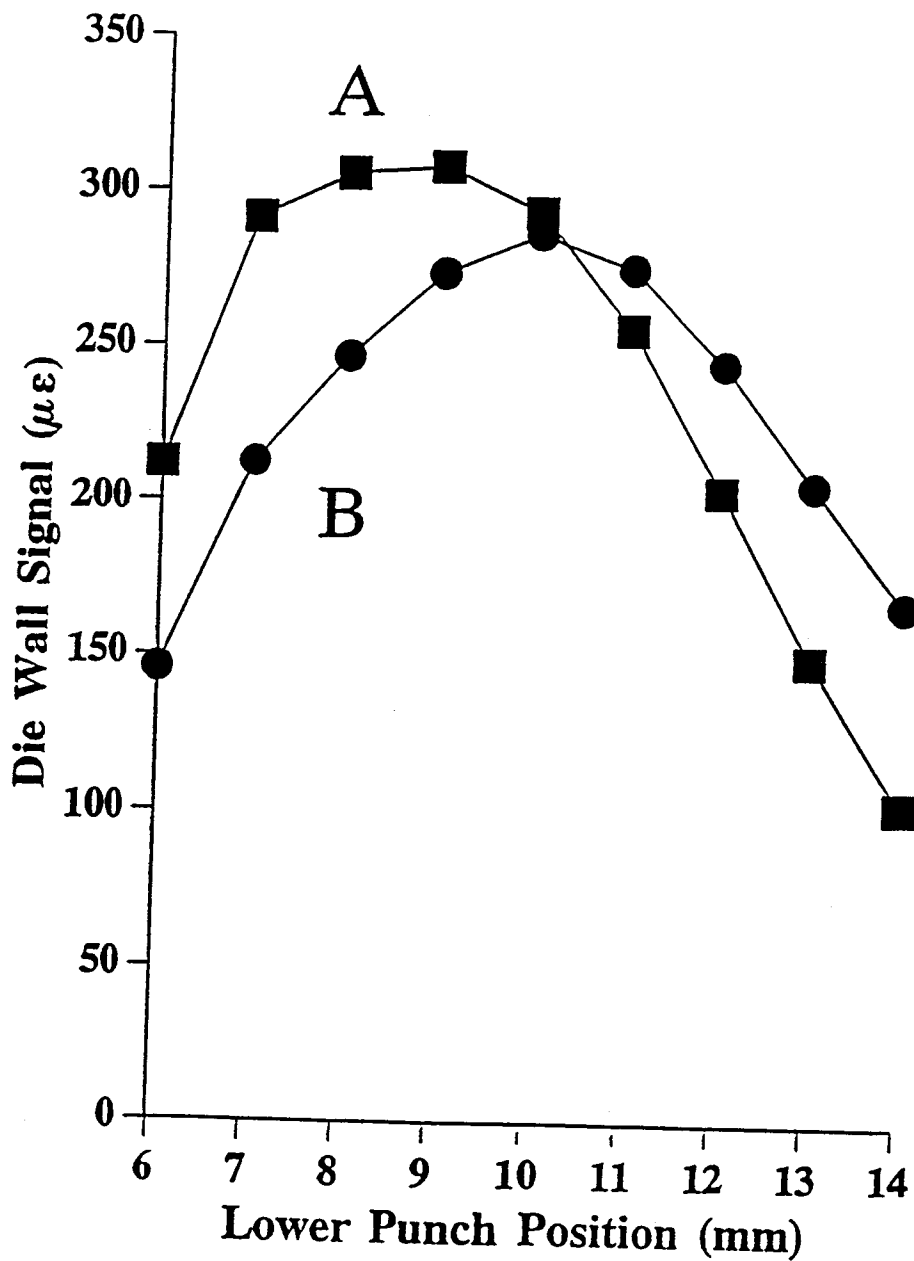
These FEA results are in excellent agreement with Hölzer and Sjögren's experimental data; the only difference between the theoretical and experimental results is that the calculated peak strains occurred at the lower punch penetration settings of 8 and 10 mm, while the experimental peak strains occurred at 7 and 8 mm for strain gage arrangements A and B, respectively. Although there are slight differences between the theoretical and experimental results, these differences can be explained by errors in estimating parameters such as material properties, compaction pressure and segmented die dimensions. Given these uncertainties, the slight differences between the theoretical and experimental results are certainly reasonable, and support the validity of the FEA calculations.



B.12 The Von Mises stress contour for symmetric segmented die at 120 MPa upper punch pressure.



**B.13** Deformed shape of the symmetric segmented die generated by COSMOS/M at 120 MPa upper punch pressure.



B.14 Die wall signals at 120 MPa upper punch pressure for various lower punch positions and at constant compact height (4 mm). bridge A: n, bridge B: l.

## CONCLUSIONS

Based upon engineering stress analysis, this study presents a general methodology for designing tablet press instrumentation. The ODP coupled with FEA and the power of modern-day computers enables the designer to simulate design performance for a wider range of loading conditions, strain gage arrangements, and design configurations than would be possible with the trial-and-error design methods. The benefits of this design-by-analysis approach include reducing design time and cost, improved performance, and increased reliability. The data presented in Figure B.8 and the design-by-analysis approach are of a general nature and can be used to optimize the cutting-angle and die wall thickness for the segmented die and any type of transducer for tablet press instrumentation. Part II of this series will apply these general methods toward the optimization of a completely different type of transducer system.



### ACKNOWLEDGMENTS

The authors wish to thank the Eli Lilly and Company and AACP Young Investigators Grant for its generous financial support and Carol A. Roberts for her typing of the manuscript.

## REFERENCES

- (1) Watt, P. R. *Tablet Machine Instrumentation in Pharmaceuticals: Principles and Practice*, Ellis Horwood Limited, (1988).
- (2) Windheuser, J. J., Misra, J., Eriksen, S. P., and Higuchi, T. Physics of tablet compression XIII; Development of die-wall pressure during compression of various materials. *J. Am. Pharm. Assn.*, 52, 767-772, (1963).
- (3) Timoshenko, S. and Goodier, J. N. *Theory of elasticity*, McGraw-Hill, New York, (1970).
- (4) Ugural, A. C. and Fenster, S. K. *Advanced Strength and Applied Elasticity*, Elsevier, (1987).
- (5) Collins, J. A. *Failure of materials in mechanical design: analysis, prediction, prevention*, John Wiley & Sons, (1993).
- (6) Ullman, D. G. *The Mechanical Design Process*, McGraw-Hill, New York, (1992).
- (7) Dally, J. W. and Riley, W. F. *Experimental Stress Analysis*, 2nd edition, McGraw-Hill, New York, (1978).
- (8) *Errors Due to Wheatstone Bridge Non-Linearity*, TN-507, Measurements Group Inc., Raleigh, USA, (1982).
- (9) Window, A. L. *Strain Gauge Technology*, Elsevier Science Publishers Ltd., (1992).
- (10) Nelson, E., Naqvi, S. M., Busse, L.W., and Higuchi, T. The Physics of Tablet Compression IV. Relationship of Ejection, and Upper and Lower Punch Forces during Comprssional Process: Application of Measurements to Comparison of Tablet Lubricants. *J. Am. Pharm. Assn.*, 43, 596-602, (1954).
- (11) Strickland, W.A. Jr., Higuchi, T., and Busse, L.W. The Physics of Tablet Compression X. Mechanism of Action and Evaluation of Tablet Lubricants. *J. Am. Pharm. Assn.*, 49, 35-40, (1960).
- (12) Salpekar, A. M., and Augsburger, L.L. Magnesium Lauryl Sulfate in Tableting: Effect on Ejection Force and Compressibility. *J. Pharm. Sci.*, 63, 289-293, (1974).

- (13) Fenner, R. T. *Engineering elasticity*, Ellis Horwood, Chichester, England, (1986).
- (14) Cook, R. D. *Concepts and applications of finite element analysis*, 2nd edition, John Wiley & sons, (1981).
- (15) Rao, S. S. *The finite element method in engineering*, Pergamon Press, 1982.
- (16) COSMOS/M. *User Guide*, SRAC, (1990).
- (17) Huckle, P. D. and Summers, M. P. The Effects of Strain Gauge Size and Configuration on Radial Stress Measurement During Tableting. *J. Pharm. Pharmacol.*, 36, Suppl. 6P, (1984).
- (18) Measurements Group, Inc.. *Strain Gage Based Transducers*, Measurements Group, Inc. Raleigh, NC, (1988).
- (19) Hölzer, A. W. and Sjögren, J. Instrumentation and calibration of a single-punch press for measuring the radial force during tableting. *Int. J. Pharmaceutics*, 3, 221-230, (1979).
- (20) Huckle, P. D. and Summers, M. P. The use of strain gauges for radial stress measurement during tableting. *J. Pharm. Pharmacol.*, 37, 722-725, (1985).